Summer 1997

Investigation of the effects of nosetip shape in terminal ballistics using a wave mechanics model

Jack Scott McMurtry

INFORMATION TO USERS

This manuscript has been reproduced from the microfilm master. UMI films the text directly from the original or copy submitted. Thus, some thesis and dissertation copies are in typewriter face, while others may be from any type of computer printer.

The quality of this reproduction is dependent upon the quality of the copy submitted. Broken or indistinct print, colored or poor quality illustrations and photographs, print bleedthrough, substandard margins, and improper alignment can adversely affect reproduction.

In the unlikely event that the author did not send UMI a complete manuscript and there are missing pages, these will be noted. Also, if unauthorized copyright material had to be removed, a note will indicate the deletion.

Oversize materials (e.g., maps, drawings, charts) are reproduced by sectioning the original, beginning at the upper left-hand corner and continuing from left to right in equal sections with small overlaps. Each original is also photographed in one exposure and is included in reduced form at the back of the book.

Photographs included in the original manuscript have been reproduced xerographically in this copy. Higher quality 6" x 9" black and white photographic prints are available for any photographs or illustrations appearing in this copy for an additional charge. Contact UMI directly to order.

UMI

A Bell & Howell Information Company
300 North Zeeb Road, Ann Arbor MI 48106-1346 USA
313/761-4700 800/521-0600

INVESTIGATION OF THE EFFECTS OF NOSETIP SHAPE IN TERMINAL BALLISTICS USING A WAVE MECHANICS MODEL

by

J. Scott McMurtry, BS, MS

A Dissertation Presented in Partial Fulfillment
of the Requirements for the Degree
Doctor of Engineering

COLLEGE OF ENGINEERING AND SCIENCES
LOUISIANA TECH UNIVERSITY

August 1997

LOUISIANA TECH UNIVERSITY

THE GRADUATE SCHOOL

May 8, 1997
Date

We hereby recommend that the thesis prepared under our supervision by Jack Scott McMurtry

entitled Investigation of the Effects of Nosetip Shape in Terminal Ballistics Using a Wave Mechanics Model

be accepted in partial fulfillment of the requirements for the Degree of Doctor of Engineering

Supervisor of Thesis Research

Head of Department
Mechanical & Industrial Engineering
Department

Recommendation concurred in:

Advisory Committee

Approved:
Director of Graduate Studies

Approved:
Dean of Graduate School

Dean of the College

GS Form 13
2/97

ABSTRACT

The purpose of this work is to delineate some of the physical mechanisms which govern the effect of nosetip shape on terminal ballistics phenomenology. A principal goal in the study of terminal ballistics has been the prediction of depth of penetration and crater diameter for penetrators and targets of various geometries, sizes, and materials. The model developed here is based on a "quasi-steady wave" mechanics approach to the problem with a 1-D model for the penetrator and a 2-D model for the target. The model is based on the application of the conservation of momentum equation to a control volume around the penetrator-target interface, and the application of both the momentum and continuity equations to control volumes around the disturbance waves in the penetrator and target.

The nosetip shape is found to influence both the structural and hydrodynamic stresses in the target. The structural stress in the target is postulated to be inversely proportional to Poisson's ratio raised to the $(1 + \sin \theta)$ power where θ is the average nosetip semi-angle based on frontal area. The hydrodynamic stress is

determined by the integral control volume analysis to be proportional to $(1 - \cos \theta)$. The effects of both of these terms are to reduce target resistance for smaller nosetip angles.

This work applies to metals, concrete, and ceramic materials for impact velocities ranging from zero to 7000 m/s. The analytical model was programmed and compared with experimental data. The predictions are nominally within the experimental uncertainty of the data.

TABLE OF CONTENTS

LIST OF FIGURES

LIST OF TABLES

ACKNOWLEDGMENTS

I wish to thank my committee chairman, Dr. E. Eugene Callens, Jr., for his help with my research efforts. I also wish to thank the other members of my committee, Drs. Randall F. Barron, Leslie K. Guice, Charles M. Sheppard, and R. Anthony Inman for their help. I appreciate the instructions and help given to me in the machine shop by Mr. Murray Rasbury and Mr. Jimmy Cook. The support of a portion this research by the U. S. Army Engineer Waterways Experiment Station (WES) Structures Laboratory, under the direction of Mr. Donald Cargile, is sincerely appreciated. The WES project was Contract No. DACA39-96-M-1557 (Louisiana Tech No. 32-4136-56112) entitled "Study of Governing Mechanisms for Projectile Nose Erosion During Penetration into Concrete and Geologic Materials."

Last, I wish to express my utmost thanks to my parents, Jack and Shirley McMurtry, for all their support and encouragement. I could never have begun or finished this project without their support.

CHAPTER 1

INTRODUCTION

This study is a continuation of previous research on the influence of penetrator and target properties on impact phenomenology and residual penetrator and crater characteristics (Ref. 1). The previous work was directed principally toward blunt projectiles impacting metal targets. It was observed in that study that a sizeable gain in penetration depth could be obtained by having a conical or ogival nosetip on the penetrator. Previous research efforts into the effects of nosetips have usually been applied to one set of impact conditions, one target material and one penetrator material. The current research seeks to develop a general analytical approach valid for a wide range of impact conditions and a broad class of penetrator and target materials as well as nosetip shapes.

Terminal ballistics has been of interest for as long as guns or bows and arrows have been in use and prediction of penetration depth without the need of expensive tests has been a goal for many years. The following is a survey of

some the literature concerning various aspects of ballistic impact.

One-Dimensional Models

Many of the one-dimensional analytical models (Refs. 2-6) are based on the Tate model(Ref. 2) which uses a modified hydrodynamic theory incorporating Bernoulli's equation. These models have a strength term, which is difficult to quantify, and are mainly applied to long rod penetrators. The models are usually tested against one set of target and penetrator materials. Penetrator length to diameter effects as well as nose-shape effects have been studied but typically yield predictions only for the specific data set being examined. For application to another set of materials, new constants must be obtained from experimental data.

Forrestal et al. (Refs. 7, 8, 10) studied spherical and cylindrical cavity-expansion approximations in simulating target response. In these models, the amount of force required to penetrate the target was found for spherical, ogival or conical nosetips. This force was used to determine the deceleration of the penetrator. A frictional term was also applied and evaluated from experimental data. Several parameters were based on experimental data so that new materials or test conditions required additional experiments to determine the new

constants. Modifications of this model include adding strain-hardening and compressible targets.

Lankford et al (Ref. 11) studied the erosion process for long rod penetrators. Some of the eroded penetrator was shown to coat the inside of the crater walls. Post experiment analyses provided a description of the eroded material, and the mushroom-shaped residual penetrators were sectioned, polished, and photographed under magnification so that the grain structure could be observed.

Anderson et al (Ref. 12) studied the velocity dependence of penetration as a function of the penetrator length to diameter ratio, L/D. The penetration depth divided by the original penetrator length, P/L, was studied for impact velocities from 1000 to 4500 m/s. It was determined that at the higher impact velocities the P/L increased for low L/D projectiles.

Concrete Target Response

Forrestal et al. (Ref. 13) performed experiments using concrete targets and ogive-nose steel projectiles. The targets ranged from low-strength grout to 62 MPa (9 ksi) concrete. This study noted that the penetrators began to erode at much lower velocities in the relatively low strength concrete targets than in metal targets.

Hanchak et al. (Ref. 14) conducted perforation experiments with ogive-nose steel penetrators into concrete

targets. The post-test entrance and exit craters were photographed. The photographs indicate three sections--a large conical entrance crater, a nearly constant-diameter cylindrical inner crater, and a large conical exit crater.

Dancygier and Yankelevsky (Ref. 15) presented a discussion of the response of reinforced concrete to fragment impacts at velocities ranging from 200 m/s to over 1000 m/s. Data were presented that deal with penetration depth and perforation of finite targets. Both high-strength and regular-strength concrete with various types of reinforcement including steel fibers were considered for different spacing and sizes of rebar. Residual velocity was not reported but crater area versus the amount of reinforcement was reported.

Forrestal et al. (Ref. 16) investigated depth of penetration for ogive-nose projectiles into concrete targets with several compressive strengths. The impact velocities range from 300 m/s to 1000 m/s. The deceleration of the projectile was studied, and displacement versus time plots for early impact times were presented.

Erosion of the Nosetip

Salik and Buckley (Ref. 17) discussed the rate at which glass beads and crushed glass beads erode steel. The weight loss of various strength steels when subjected to crushed glass for five minutes and 10 minutes were compared. The

steel was heat treated to change its hardness and thus its erosion properties.

Allen et al (Ref. 18) discussed the deceleration of .50 caliber projectiles when they impact dry quartz sand. The deceleration of the projectile was studied as well the behavior of sand under loading and unloading. Nosetip erosion was not discussed but behavior of the target was investigated. Even though the target was sand instead of concrete, the particle nature of the sand could be used to infer the behavior of concrete particles when pulverized by the impact shock wave.

Friction and Wear Behavior

Miyoshi and Buckley (Refs. 19-25) investigated different aspects of friction and wear between single-crystal silicon carbide in contact with various metals. Even though silicon carbide particles are different from concrete particles, the friction and wear patterns should be similar in appearance. The mechanisms discussed and illustrated should be applicable for concrete impact.

Loomis and Jones (Ref. 26) examined a wear-brake device rather than a single crystal. This paper may be less applicable since the wear times were much longer than the average impact time. However, these results might give an

upper limit on the amount of erosion that could occur during penetration.

Tylczak (Ref. 27) used a rotating drum to study the effects of wear. The times studied are longer than the typical impact time. However, these results might also give an indication of the upper limit on the amount of erosion that could occur during penetration.

Earth and Other Geologic Material Penetration

Longcope (Ref. 28) examined some targets such as antelope tuff. This work extended the penetration data base to a greater variety of target materials against which prediction models can be tested.

Lundgren (Ref. 29) dealt with the boosted penetrator problem. The penetrators were to be impacted into earth. The study discussed the effects of eroded, bent, or broken penetrators.

Forrestal et al. (Ref. 30) investigated the forces that are produced on conical nosetips when impacted by foundry core targets. The experimental peak accelerations and forces were reported for impact velocities from 200 m/s to 1200 m/s. These forces can be used to determined the impact velocities that cause the penetrator to flow.

Forrestal et al. (Ref. 31) performed reverse ballistics experiments by launching foundry cores samples which had a

density slightly less than concrete. The impact velocities ranged from 600 m/s to 2200 m/s. The penetrators, which had three or six caliber radius (CRH) head ogive nosetips, were photographed so that comparisons could be made. The photographs were too unclear to measure residual penetrator lengths, and therefore penetration depths were not reported. However, the peak accelerations and the peak forces were reported. The penetrators were tungsten alloy, and the velocity and acceleration were measured with laser interferometry and accelerometers, respectively.

Brunette and Goldsmith (Ref. 32) studied anchoring in rock by propellant driven penetrators. The impact velocities ranged from 100 m/s up to 400 m/s. Several different types of geologic targets were examined. Some of the penetrators were removed and photographed. Some penetration depth data were reported, but no residual penetrator results were given.

Other Studies

Turgutlu et al. (Ref. 33) investigated the manner in which penetrators deform. The penetrators and targets were metals, and many different-angled conical nosetips were examined as well as penetrators with cavities in the nosetips. The metal targets were etched to show stress patterns caused by the impact. The paper mostly dealt with spot welding, and deformation was secondary.

Chen (Ref. 34) presented a computer simulation of a steel projectile impacting a concrete slab. The paper discussed various assumptions relating to the properties of the penetrator and target. The only result in the paper is a graph of residual velocity versus striking velocity.

Bernoulli Equation Use in Penetration Studies

The model used in this paper, while resembling the Tate model (Ref. 2), is significantly different. The Tate model uses a form of the Bernoulli equation, whereas the current work uses the conservation of momentum equation. This difference introduces a slight but critical distinction between these equations in that the relationship between the structural and hydrodynamic stresses is affected. The Bernoulli equation is not appropriate for this application since the values of the Bernoulli constant are unequal across the penetrator-target interface except at the stagnation point, which is a singular point. However, the conservation of momentum equation does hold across the interface.

Objectives

The objectives of this work are to extend the previous work relating to blunt projectiles (Ref. 1) and to expand the work to include the influence of various nosetip configurations. This work also examines different target

types such as metals, concrete, and ceramics. All velocity regimes from very low velocity to hypervelocity are included. The targets are assumed to be semi-infinite and stationary relative to the penetrator unless otherwise stated.

Wave Mechanics

The initial portion of this study is directed toward understanding the physics of penetrator deceleration and the initial and final transients. Examining experimental photographs for the purpose of characterizing penetrator deceleration leads to the observation that the time between impact and the end of penetrator motion is approximately the amount of time required for the disturbance wave to repeatedly travel back and forth in the penetrator, slowing the penetrator by twice the velocity change across the wave (the particle velocity) during each complete wave cycle. The strength of the wave corresponds to a pressure equal to nearly three times the static compressive strength of the penetrator. A coefficient of static compressive strength is derived for any given material by comparing the lateral stress caused by a normal force on a material element to the static compressive strength of the material. Disturbance waves must therefore be considered in the impact process since the usual impact time is less than 200 microseconds, which is insufficient time to ignore wave motion. The time

for a single wave traversal is a significant fraction of the total event time.

In addition, it is postulated that the heat transfer by conduction is negligible due to the very short encounter time of the impact process. Therefore, the penetrator and target properties are assumed to be at constant temperature, and the momentum equation is uncoupled from the energy equation.

Since the impact process is controlled by the disturbance waves, it is modeled as a quasi-steady event. That is, the conditions at the penetrator-target interface are assumed to be constant as the compression wave travels from the interface to the end of the penetrator and returns to the interface as an expansion wave. Only then do the interface conditions adjust to the reduced penetrator velocity.

Penetrator and Target Particle and Flow Velocities

Consistent with these assumptions, the one-dimensional conservation of mass and momentum equations are used to analyze the impact parameters. The conservation of mass equations across the two disturbance waves and three conservation of momentum equations, and two across the shock waves and one for the penetrator-target interface, are used in the formulation of the solution model.

When the disturbance wave travels from the penetrator-target interface into the penetrator, the disturbance wave compresses the penetrator material as it travels. Since the penetrator material has a finite ultimate compressive strength, there is a corresponding limit to the strength of the penetrator disturbance wave. If the stress at the penetrator-target interface is above the ultimate free-surface penetrator compressive strength, a compression wave with a strength equal to the ultimate free-surface compressive strength is formed to transfer the stress. The remainder of the interface pressure is relieved by the flow of penetrator material from the interface. Therefore, the higher the interface pressure, the higher the penetrator flow velocity.

The target responds in a similar way because it also has a finite ultimate compressive strength and relieves excess pressure by flowing around the penetrator. However, one principal difference is that the target material is confined by the material around it. Hence, it requires more pressure to force the target material to flow around the penetrator-target interface. The nosetip of the penetrator will affect this confined target structural stress term as well as the target hydrodynamic stress term in the momentum equation resulting in a different flow of target material for each nosetip. For example, the flow around a blunt non-

deforming penetrator is different from the flow around a non-deforming 10-degree conical nosetip penetrator.

The material compression or expansion velocities across the disturbance waves are components in the interface kinematic velocity relation and are referred to as particle velocities. The velocities of the penetrator and target materials that flow away from the interface are also components in the interface kinematic velocity equation and are called flow velocities.

Influence of Nosetip Shape

The addition of different nosetip shapes to the study introduces additional complexity to the equations. The velocity at which the nosetip begins to flow is an important parameter since the flow will alter the nosetip shape. The equations must take into account this deformation and the corresponding changes in average penetrator nosetip angle and penetrator-target interface pressure. The required changes in the governing equations are discussed below.

A penetrator nosetip, such as 3 caliber radius head (CRH) ogive, can have a significant effect upon penetration depth. In an experiment performed at Louisiana Tech University, blunt and ogive nosetip armor-piercing steel rounds were fired into aluminum targets. The penetration depth for the ogive nosetip was four times that of the blunt

penetrator at an impact velocity of 1200 m/s. This example illustrates the dramatic effect that nosetip shape can have on penetration depth.

Initial and Final Transients

When the penetrator strikes the target, high-strength shock waves are created and travel into the target and the penetrator. Since these shock waves are formed before the material begins to flow to relieve the high pressure, the waves are typically strong enough at moderate impact velocities to cause plastic flow or to break many of the bonds in the materials near the interface. These strong impact shock waves rapidly decrease in strength as the materials begin to flow. The time for the initial transient is taken to be the time for the passage of the lateral release wave in the penetrator. It is postulated that the penetrator and target will remain in contact after the dissipation of the Hugoniot shock and that the pressure will decrease rapidly to the developed impact pressure.

During impact under these conditions, the penetrator is both decelerating and eroding. If the impact velocity is low enough, the penetrator will stop before it is completely eroded. However, if the impact velocity is sufficiently high, the entire penetrator will flow through the penetrator-target interface. When the penetrator is

completely eroded, there remains a high-pressure region at the penetrator-target interface. This high pressure region generates a terminal transient which expands into the target until the local pressure is equal to the target free-surface ultimate compressive strength, which is defined as the material compressive strength divided by Poisson's ratio (Ref. 1). Higher impact velocities result in higher residual pressures and increased depth of penetration for the final transient. Weaker target materials also result in larger terminal transient penetration.

CHAPTER 2

RESPONSE OF THE PENETRATOR

Density of Compressed Material

At impact, a generated compression wave which travels along the penetrator compressing the penetrator material. Applying the conservation of mass equation across the penetrator compression wave as illustrated in Fig. 1 results in the following equation

$$\rho_p A_p V_{sp} = \rho_p' A_p (V_{sp} - U_{pp}) \tag{1}$$

$$\rho_p' = \rho_p \left(\frac{V_{sp}}{V_{sp} - U_{pp}} \right) \tag{2}$$

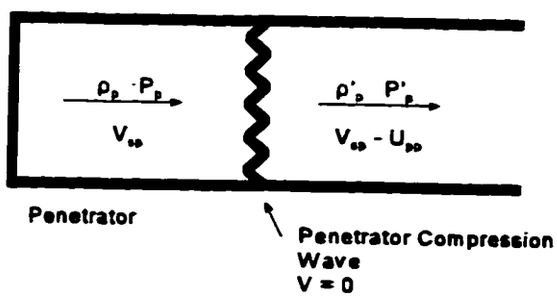

Fig 1. Penetrator Properties Relative to the Compression Wave

where

A_p = area of penetrator.

ρ_p = density of the material before wave passage.

ρ_p' = density of the material after wave passage.

V_{sp} = speed of wave = $C_{op} + S_{ip} \times U_{pp}$.

U_{pp} = velocity of the penetrator material after wave passage relative to the penetrator material before wave passage (particle velocity or compression or expansion velocity).

C_{op} = zero pressure speed of sound.

S_{ip} = Hugoniot constant.

Thus the conservation of mass equation provides the density increase caused by the wave passage.

Stress in Compressed Material

The pressure at the interface between the penetrator and the target generates the compression wave that propagates into the penetrator, compressing the penetrator material as it passes. Applying the conservation of momentum and conservation of mass equations across the penetrator compression wave, the stress, P_p', in the material caused by the passage of the wave (Fig. 1) is derived.

$$P_p' = \rho_p U_{pp} V_{sp} \qquad (3)$$

The penetrator stress before wave passage, P_p, is taken to be zero since the free end of the penetrator is

approximately a zero pressure boundary and therefore cannot support stresses.

The wave attempts to compress the penetrator until the stress P_p' is equal to the stress at the penetrator-target interface. However, the wave can only raise the stress in the penetrator until it reaches the limiting maximum stress as is discussed in the next section.

Penetrator Maximum Allowable Stress

The strength of the disturbance waves in the penetrator is postulated to be dependent upon the static ultimate compressive strength of the material and upon Poisson's ratio. For the case where the compression wave generates a stress, P_p', less than the maximum allowable, S_p', the penetrator material does not flow ($U_{pf} = 0$) and the stress is found by applying the conservation of momentum and mass equations across the compression wave.

$$P_p' = \rho_p U_{pp} V_{sp} \quad for \quad U_{pf} = 0 \tag{4}$$

For the case where the compression wave generates a stress, P_p', equal to the maximum allowable, S_p', the penetrator material flows at the penetrator-target interface ($U_{pf} > 0$) and $P_p' = S_p'$ so that the equation is

$$P_p' = S_p' = \rho_p U_{ppm} V_{sp} \quad for \quad U_{pf} > 0 \tag{5}$$

$$U_{ppm} = \frac{C_{sp}\sigma_{sp}}{\rho_p V_{sp}} \tag{6}$$

$$C_{sp} = \nu_p^{-1} \quad (7)$$

where

U_{ppm} = maximum penetrator particle velocity.

C_{sp} = penetrator free surface maximum stress constant.

ν_p = Poisson's ratio for the penetrator material.

σ_{sp} = penetrator ultimate compressive strength.

U_{pf} = penetrator flow velocity.

When the pressure at the penetrator-target interface exceeds this limit, the pressure is relieved by the flow of the penetrator material near the interface. Above this maximum allowable penetrator pressure, the penetrator flow velocity increases with interface pressure.

A heuristic argument for the postulation that the penetrator free-surface maximum stress constant is inversely proportional to Poisson's ratio (Eqn. 7) is that the principal compressive stress in the penetrator is longitudinal (σ_L) but the stress component that must exceed the ultimate compressive strength in order for the material to flow is transverse (σ_T) as illustrated in Fig. 2. It is therefore the relationship between longitudinal and transverse stresses that dictates the penetrator response to a compression wave. This relationship is deduced from the definition of Poisson's ratio and Hooke's law.

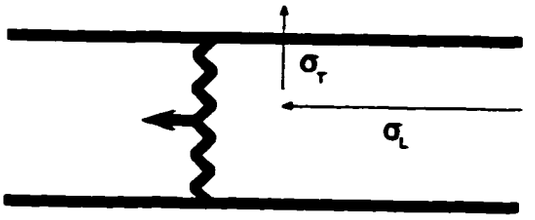

Fig. 2. Relationship of Transverse Stress to Longitudinal Stress

$$\frac{\epsilon_T}{\epsilon_L} = \nu \tag{8}$$

$$\sigma = E\epsilon \tag{9}$$

where

ϵ_T = strain in the transverse direction.

ϵ_L = strain in the longitudinal direction.

E = modulus of elasticity.

Combining the two equations gives the approximation

$$\frac{\sigma_T}{\sigma_L} \sim \nu \tag{10}$$

The relationship is considered approximate since Poisson's ratio is for tensile strain, not compressive strain. However, it is assumed that for most materials the relationship between lateral strain and longitudinal strain for compression is similar to that for tension.

Deceleration of the Penetrator

When the compression wave arrives at the end of the penetrator, it reflects from the zero pressure boundary as an expansion wave. This expansion wave travels back along the penetrator relieving the stress as it propagates. When the wave arrives back at the penetrator-target interface, it encounters the high-pressure boundary region and reflects as a compression wave. The process then repeats itself.

The time that it takes for the compression wave to travel to the end of the penetrator, plus the time for the expansion wave to return to the interface, is very important because it establishes the deceleration of the penetrator. During this time, the penetrator will decelerate by an amount equal to twice the value of the particle velocity, U_{pp}. This deceleration occurs because the compression wave slows the penetrator by one U_{pp} as it travels down the penetrator and the expansion wave slows the penetrator another U_{pp} on the return to the interface. The conditions at the interface are assumed not to change until the wave returns and lowers the velocity of the penetrator. The penetrator and target flow velocities are then assumed to adjust to the new conditions.

Using L_p^i as the length of the penetrator when the shock wave is at the penetrator-target interface, the time for the shock wave to reach the free end of the penetrator is

$$\Delta t_1 = \frac{L_p^i}{V_{sp}} \tag{11}$$

The deceleration of the penetrator when the wave has reached the free end of the penetrator is

$$Deceleration = \frac{U_{pp}}{\Delta t_1} \tag{12}$$

Using L_p^{i+1} as the length of the penetrator when the expansion wave reaches the penetrator-target interface, the time required for the expansion wave to travel from the free end of the penetrator to the interface is

$$\Delta t_2 = \frac{L_p^{i+1}}{V_{sp}} \tag{13}$$

The amount of decrease in the penetrator length per wave cycle is

$$L_p^i - L_p^{i+1} = U_{pf}(\Delta t_1 + \Delta t_2) + U_{pp}(\Delta t_1 - \Delta t_2) \tag{14}$$

The full deceleration that the penetrator experiences over the period of time it takes for the compression wave to traverse the penetrator and return to the interface as an expansion wave is

$$Full\ Deceleration = \frac{2U_{pp}}{\Delta t_1 + \Delta t_2} \tag{15}$$

As can be seen from Eqn. (15), the principal factor in the deceleration of the penetrator for a given material is the time for a full wave cycle. A longer penetrator will penetrate deeper into a target since its deceleration is

lower. The total time required for this compression-expansion wave traversal cycle is

$$\Delta t_t = \Delta t_1 + \Delta t_2 = \frac{L_p^{\,i} + L_p^{\,i+1}}{V_{sp}} \tag{16}$$

As the compression wave travels from the interface to the free end of the penetrator, it compresses the penetrator. If the penetrator is flowing, $U_{pf}>0$, the penetrator is decreasing in length due to two processes, the penetrator compression and penetrator flow. The time for the compression wave to travel along the penetrator is Δt_1 so the decrease in length of the penetrator for the half wave pass is

$$(U_{pf} + U_{pp})\,\Delta t_1 \tag{17}$$

As the expansion wave travels back into the compressed penetrator material, it relieves the stress. This process increases the length of the penetrator. If the penetrator is flowing, $U_{pf}>0$, the penetrator is decreasing in length due to the flow velocity. The time for the expansion wave to travel from the free end of the penetrator to the interface is Δt_2 and the amount of penetrator lost during this time is

$$(U_{pf} - U_{pp})\,\Delta t_2 \tag{18}$$

The sum of the two equations gives the final penetrator length

$$L_{pf} = L_{pI} - \sum_{i=1}^{n} [(U_{pf}^i + U_{pp}^i)\,\Delta t_1^i + (U_{pf}^i - U_{pp}^i)\,\Delta t_2^i] \tag{19}$$

where

L_{pf} = length of the penetrator after penetrator is completely eroded or after the penetrator has stopped.

L_{pI} = initial length of the penetrator before impact.

n = number of wave cycles until either the penetrator length is zero or the penetrator has stopped.

Velocity Component Kinematic Relationship

Fig. 3 illustrates the component velocities for a fixed observer with V_t equal to the target velocity. The penetrator flow velocity, U_{pf}, can be defined as the difference between the penetrator velocity at the interface and the velocity of the penetrator-target interface

$$U_{pf} = V_p - U_{pp} - U_{tf} - U_{pt} - V_t \tag{20}$$

where

V_p = velocity of the penetrator.

U_{tf} = target flow velocity.

Solving for the velocity of the penetrator and assuming that the target is stationary, $V_t = 0$, the velocity component kinematic relationship is obtained

$$V_p = U_{pf} + U_{tf} + U_{pp} + U_{pt} \tag{21}$$

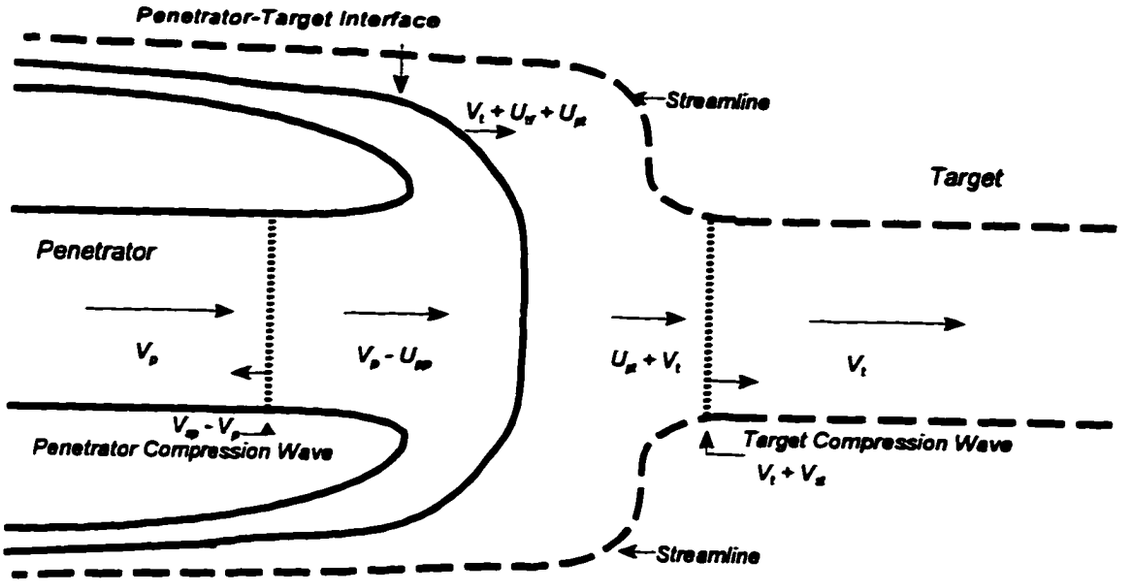

Fig. 3. Velocity Components Relative to a Fixed Observer

Calculation of Average Nosetip Angle

The addition of a nosetip shape, other than blunt, adds the additional complexity that the average nosetip angle must be determined. The full effect of an angled nosetip is addressed in another chapter. Here, the procedure for calculation of the average nosetip angle is presented. The average nosetip angle is based on frontal area and defined as

$$\theta = \frac{1}{A_p}\int_0^{A_p} \theta_p \, dA \qquad (22)$$

where

θ = average nosetip angle.

θ_p = local nosetip angle.

A_p = frontal area of the penetrator = πr_p^2.

r_p = radius of the penetrator.

dA = differential frontal area.

With dA set equal to $2\pi r\, dr$ the equation becomes

$$\theta = \frac{2}{r_p^2}\int_0^{r_p} \theta_p r\, dr \qquad (23)$$

For a cone, $\theta_p = \theta_c$ = constant and $\theta = \theta_c$

The average nosetip angle is calculated for a simple case as shown in Fig. 4. The equation for average nosetip angle becomes

$$\theta = \frac{1}{A_p}\sum_1^n \theta_i A_i \qquad (24)$$

where

θ_i = nosetip angle of the i^{th} section of the penetrator.

A_i = frontal area of the i^{th} section of the penetrator.

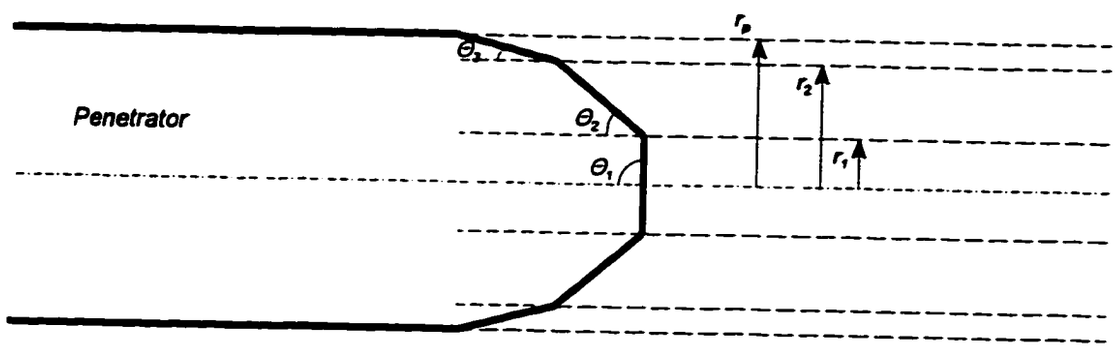

Fig. 4. Nomenclature for Average Nosetip Angle Calculation

For the case shown in Fig. 4, the equation for average nosetip angle is

$$\theta = \frac{1}{r_p^2}\left[\theta_1 r_1^2 + \theta_2 (r_2^2 - r_1^2) + \theta_3 (r_p^2 - r_2^2)\right] \tag{25}$$

The average nosetip angle is based upon the frontal or projected area because the component of the interface force that provides the axial compression (and therefore the deceleration) of the penetrator is transmitted through the frontal area.

The average nosetip angle remains constant for a non-flowing penetrator. For a flowing penetrator, the average nosetip angle increases and must be recalculated as a function of time.

CHAPTER 3

RESPONSE OF THE TARGET

Density of Compressed Material

Applying the conservation of mass equation across the compression wave that propagates into the target, as illustrated in Fig. 5

$$\rho_t A_p V_{st} = \rho_t' A_p (V_{st} - U_{pt}) \tag{26}$$

$$\rho_t' = \rho_t \left(\frac{V_{st}}{V_{st} - U_{pt}}\right) \tag{27}$$

where

ρ_t = density of the material before wave passage.

ρ_t' = density of the material after wave passage.

V_{st} = speed of the disturbance wave = $C_{ot} + S_{it} \times U_{pt}$.

U_{pt} = velocity of the penetrator material after wave passage relative to the penetrator material before wave passage (particle velocity or compression velocity).

C_{ot} = zero pressure speed of sound.

S_{it} = Hugoniot constant.

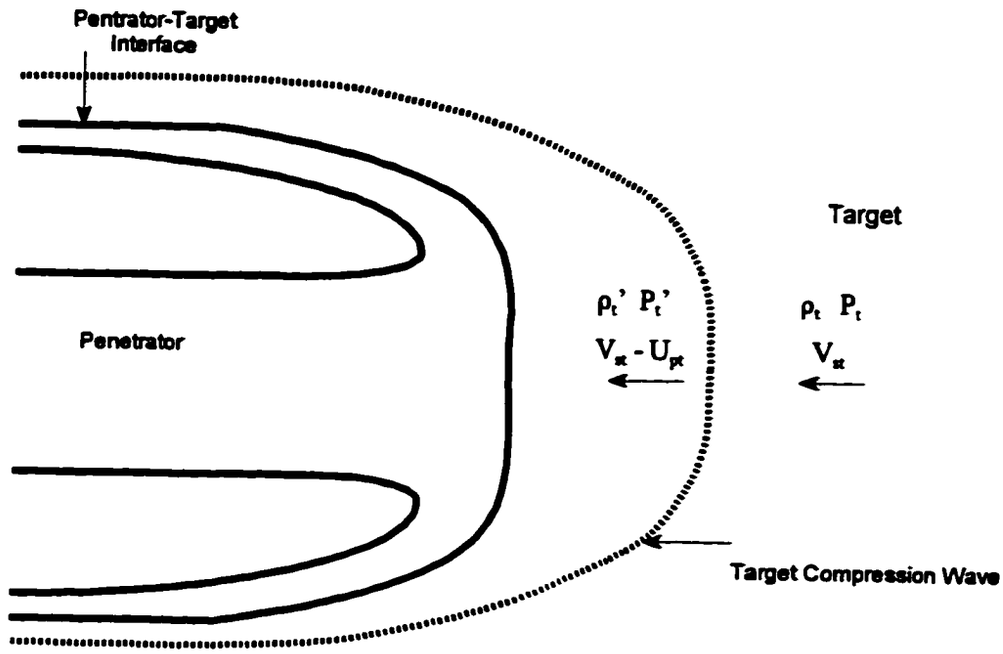

Fig. 5. Target Properties Relating to the Compression Wave

Thus the conservation of mass equation gives the density increase caused by the compression wave. It is noted that P_t is equal to zero because the target is assumed to be unstressed until the compression wave has passed. As the penetrator-target interface moves into the target, compression waves are generated in front of the interface , creating a stress gradient. The ρ_t' is therefore the density of the target right before the interface arrives. Since the compression waves weaken as they move away from the interface, the associate particle velocity decreases accordingly. Thus the target material is not moving at the full U_{pt} except immediately in front of the interface. At

conditions of relatively low target flow velocity compared with the compression wave velocity, the U_{pt} is very small away from the interface since the weakening compression wave far outdistances the interface. This effect occurs because the expansion waves from the free surface and unstressed material have time to partially relieve the stress caused by the compression waves.

Stress in Compressed Material

Applying the conservation of momentum and conservation of mass equations across the target compression wave, the stress, P_t', in the material caused by the passage of the wave (Fig. 5) is derived.

$$P_t' = \rho_t U_{pt} V_{st} \tag{28}$$

P_t is equal to zero because P_t is in the unstressed part of the target.

The pressure at the interface between the penetrator and the target generates the compression wave that propagates into the target, compressing the target material as it passes. The compression waves in front of the penetrator-target interface can only raise the stress in the target until it reaches the limiting maximum. When the pressure at the penetrator-target interface exceeds this limit, the interface begins to flow to relieve the stress. Unlike the penetrator, the target is confined for deep

penetration so that it requires a higher pressure to initiate flow compared to a penetrator of the same material. The targets are assumed to be semi-infinite in dimension so that reflected compression waves from the outer edges are not taken into account.

Target Maximum Allowable Stress

At impact, a shock wave is generated which propagates into the target expanding in an ellipsoid-shaped front. The shape of this wave is dependent upon the transverse and axial sound speeds in the target.

At impact, the maximum allowable stress in the target is related to the strength of the target by a different function as compared to the penetrator. The target is confined, unlike the penetrator, so the maximum allowable stress is greater. For the case where the compression wave generates a stress, P_t', less than the maximum allowable, S_t', the penetrator material does not flow ($U_{tf} = 0$) and the stress is found by applying the conservation of momentum and mass equations across the compression wave.

$$P_t' = \rho_t U_{pt} V_{st} \quad for \quad U_{tf} = 0 \tag{29}$$

For the case where the compression wave generates a stress, P_t', equal to the maximum allowable, S_t', the penetrator material flows at the penetrator-target interface ($U_{tf} > 0$) $P_t' = S_t'$ so that the equation is

$$P_t' = S_t' = \rho_t U_{ptm} V_{st} \quad for \quad U_{tf} > 0 \tag{30}$$

$$U_{ptm} = \frac{C_{st}\sigma_{st}}{\rho_t V_{st}} \tag{31}$$

$$C_{st} = \frac{1}{\nu_t^{[1+\sin\theta]}} \tag{32}$$

where

U_{ptm} = maximum target particle velocity.

C_{st} = target confined maximum stress constant.

υ_t = Poisson's ratio for the target material.

σ_{st} = target compressive strength.

θ = average nosetip angle.

The [1 + sin θ] exponent on Poisson's ratio in the expression for target confined maximum stress constant reduces to two when the average nosetip angle is 90 degrees (blunt). In the penetrator, the material has to transmit the stress only through one 90-degree turn in order to flow (Fig. 2), but as can be seen in Fig. 6, the target

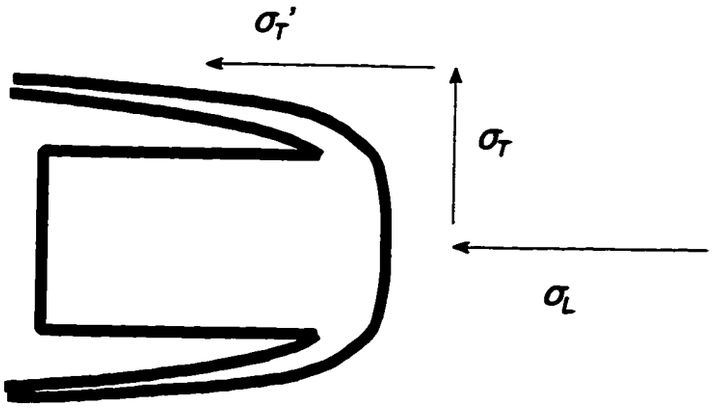

Fig. 6. Confined Stress Transmission in Target for Blunt Nosetips

stress must be transferred through two 90 degree turns to flow past the target for a blunt nosetip. This suggests using Poisson's ratio for each 90-degree transfer as was done for the single 90-degree transfer in the case of the penetrator.

$$\frac{\epsilon_T}{\epsilon_L} = \nu \tag{33}$$

$$\frac{\epsilon_T'}{\epsilon_T} = \nu \tag{34}$$

Combining these two equations with Hooke's law, we note that

$$\frac{\sigma_T'}{\sigma_L} \sim \nu^2 \tag{35}$$

so that the exponent [1 + sin θ] is equal to two.

For angled nosetips, the [1 + sin θ] term is postulated to approximate the situation shown in Fig. 7. That is, when the average nosetip angle is less than 90 degrees, the stress is not transmitted through two full 90-degree turns. The form of the term was chosen because it fits the data well and is a reasonable approximation from observing Fig. 7. The maximum confined surface structural stress immediately in front of the penetrator-target interface varies from σ_{st}/ν_t, for $\theta = 0$ (free-surface maximum value) to σ_{st}/ν_t^2 for $\theta = 90$ (blunt nosetip).

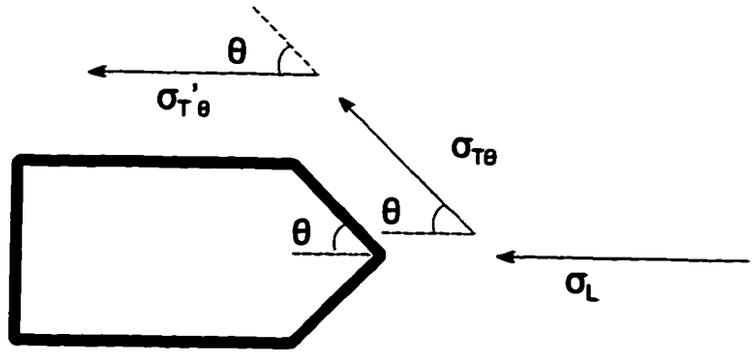

Fig. 7. Confined Stress Transmission in Target for Conical Nosetips

CHAPTER 4

PENETRATOR-TARGET INTERFACE

When the penetrator strikes the target, two generated shock waves propagate into the target and penetrator. An interface exists between the target and penetrator materials, across which there is no mass flow. From Fig. 3, it is observed that the interface moves with a velocity of $U_{tf} + U_{pt}$ relative to a stationary observer for a stationary target. As penetration continues, the penetrator pushes the interface into the target to become the crater walls.

Conservation of Momentum

The impact event velocities relative to the penetrator target interface are shown in Fig. 8a for a blunt flowing nosetip and in Fig. 8b for a non-flowing penetrator with a conical nosetip of half-angle θ.

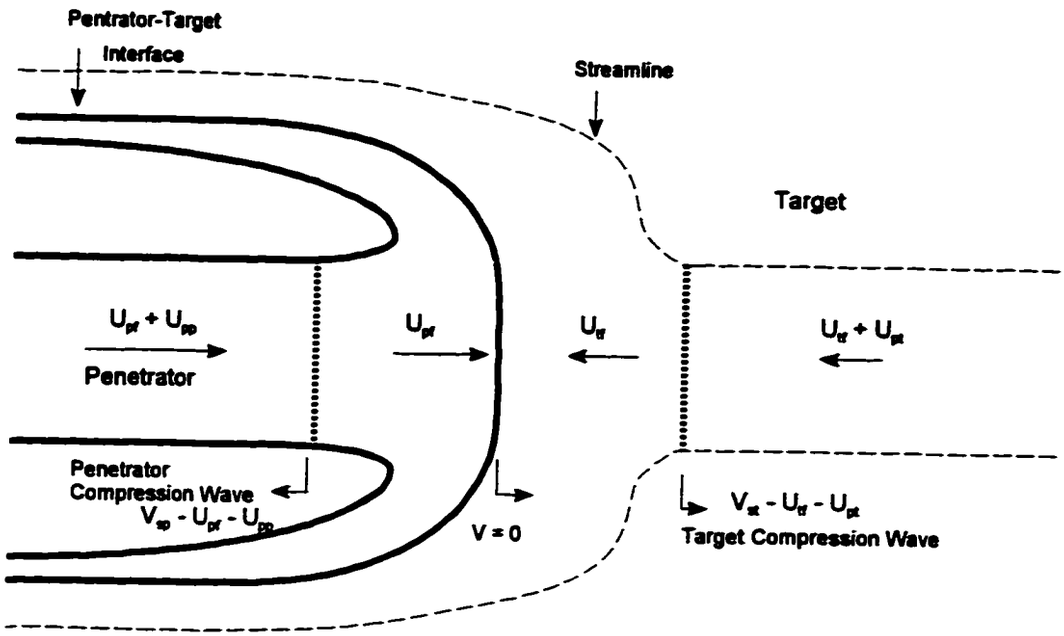

a. Blunt Flowing Nosetip

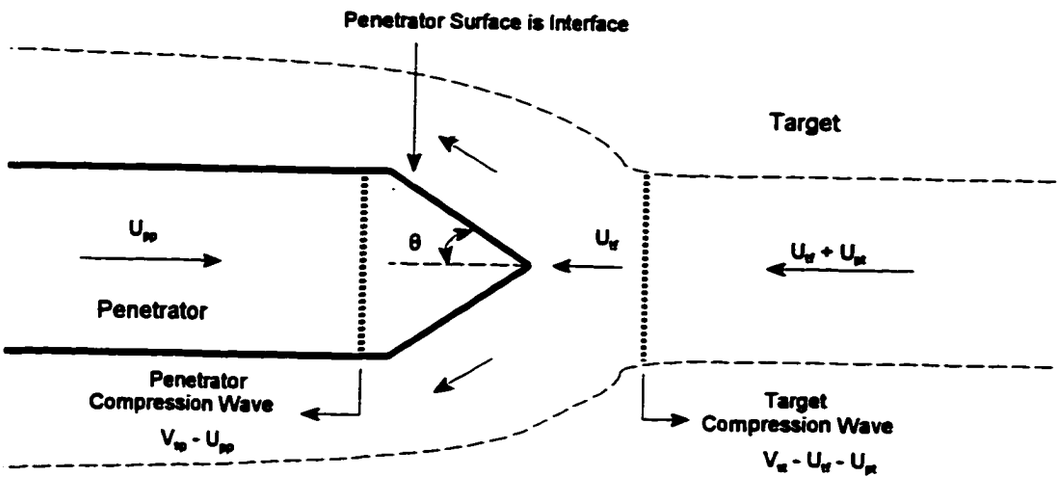

b. Conical Non-Flowing Nosetip

Fig. 8. Impact Event Velocities Relative to Penetrator-Target Interface

Fig. 9a illustrates the selection of control volume for the conservation of momentum integral analysis of the penetrator and target streams for a blunt flowing nosetip. It is hypothesized that both the penetrator and target material exit the control volume at an angle of 90 degrees from the centerline. When the conservation of momentum integral relation is applied in the axial direction

$$P_p' A_p + \dot{m}_p U_{pf} = \dot{m}_t U_{tf} + P_t' A_p \tag{36}$$

Substituting the relations for penetrator and target mass flow rates

$$\dot{m}_p = \rho_p' A_p U_{pf} \tag{37}$$

$$\dot{m}_t = \rho_t' A_p U_{tf} \tag{38}$$

and dividing by the area of the penetrator, the interface momentum equation becomes

$$P_p' + \rho_p' U_{pf}^2 = \rho_t' U_{tf}^2 + P_t' \tag{39}$$

Fig. 9b illustrates the selection of control volume for the penetrator body and target stream for a non-flowing penetrator with a conical nosetip. Since the target stream leaves the control volume at an angle θ to the centerline, it presents a force component equal to

$$\dot{m}_t U_{tf} \cos\theta \tag{40}$$

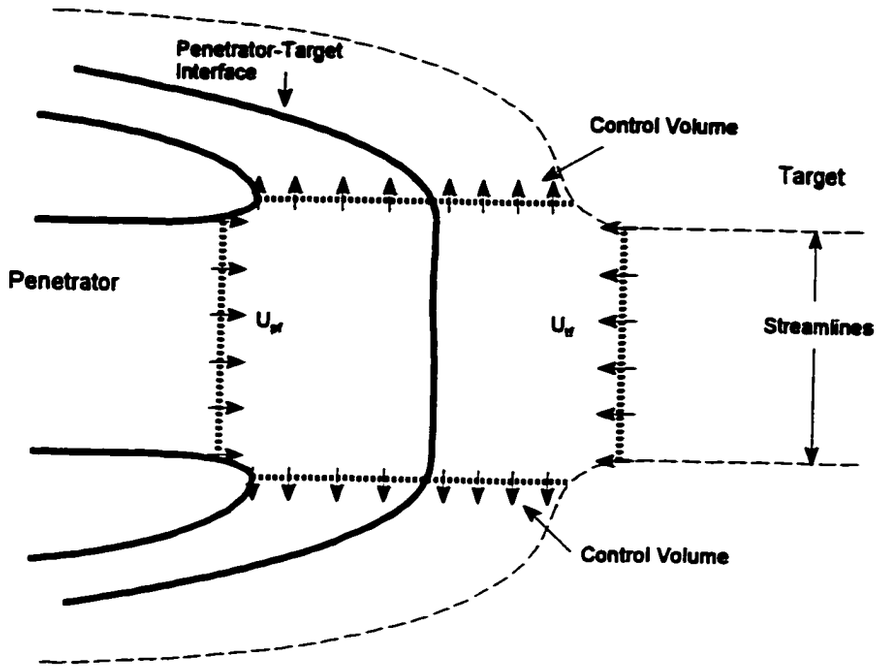

a. Blunt Flowing Nosetip

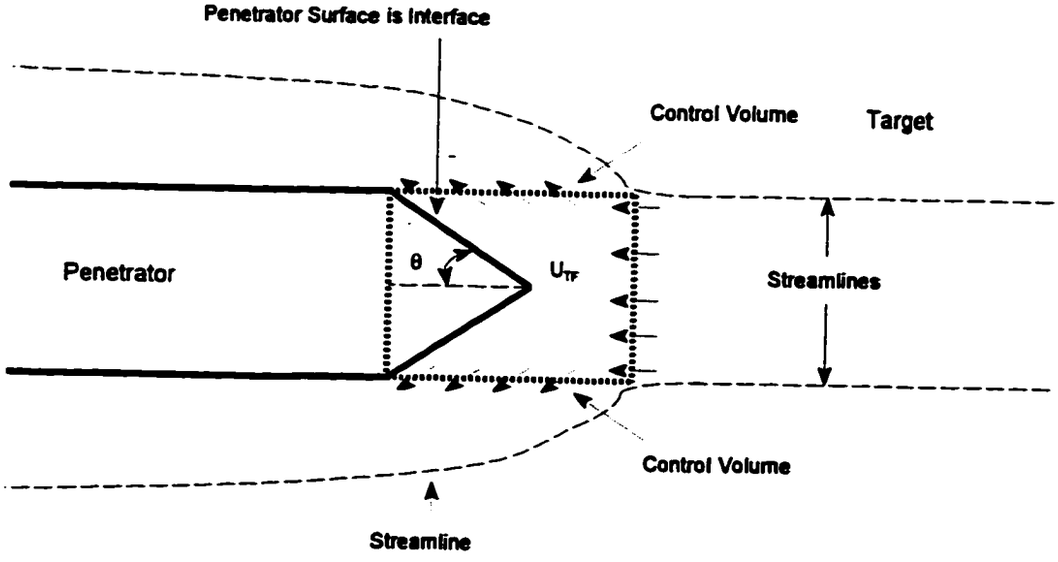

b. Conical Non-flowing Nosetip

Fig. 9. Control Volume for Conservation of Momentum Integral Analysis

in the axial direction. The conservation of momentum equation in the axial direction becomes

$$P_p' A_p + \dot{m}_p U_{pf}^2 = \dot{m}_t (U_{tf} - U_{tf} \cos\theta) + P_t' A_p \qquad (41)$$

Substituting the relations for penetrator and target mass flow rates and dividing by the area of the penetrator the interface momentum equation becomes

$$P_p' + \rho_p' U_{pf}^2 = \rho_t' U_{tf}^2 (1 - \cos\theta) + P_t' \qquad (42)$$

Therefore, when the penetrator has an angled nosetip, the target hydrodynamic term in the momentum equation is reduced by the multiplying factor [1 - cos θ]. The hydrodynamic term varies from zero for θ = 0, to the full target stream value $\rho_t U_{tf}^2$ for θ = 90 degrees (blunt nosetip). In addition, it was postulated in Eqns. (29-32) that the structural stress term, P_t', is at its maximum allowable value, S_t', for the specified average nosetip angle. Furthermore, this maximum allowable stress is inversely proportional to Poisson's ratio raised to the [1 + sin θ] power. Thus, the target resistance is reduced in both the hydrodynamic and structural stress terms.

When the penetrator has an angled nosetip and is flowing, there is a layer of penetrator material that flows out of the control volume next to the surface (Fig. 10). A difficulty that enters the problem is that the amount of penetrator surface in contact with the target stream

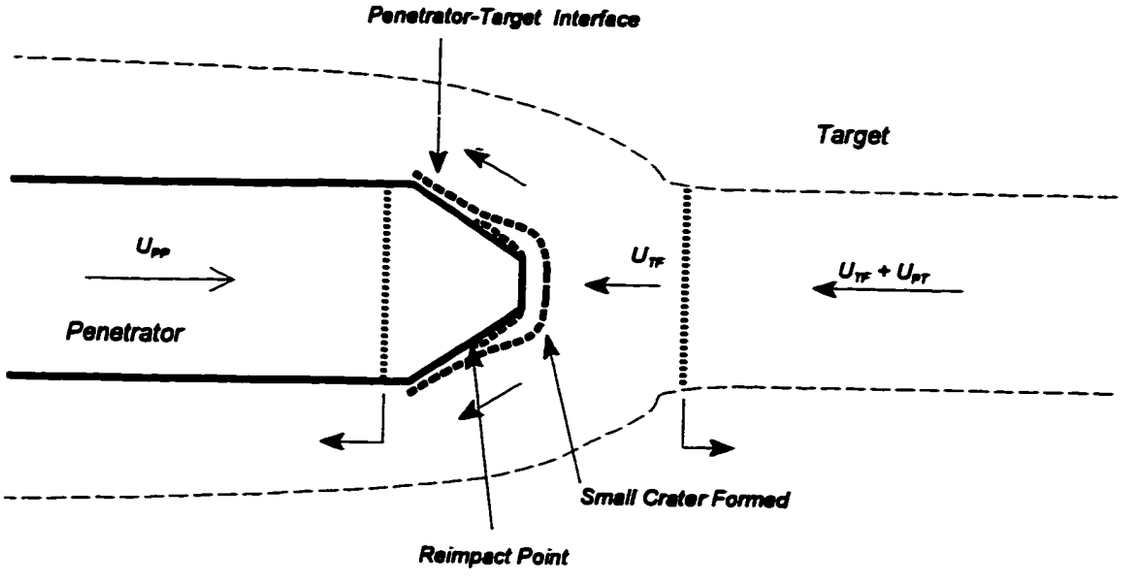

Figure 10. Flowing of an Angled Nosetip

is now not known. The momentum of the penetrator flow in the transverse direction pushes the target material outward, meaning that when the nosetip begins to flow, a small crater is formed near the forward region which will be enlarged by reimpacting the penetrator surface (Fig. 10). The flow field turning angle is not easily determined in this situation. In order to approximate this effect, an average of the average nosetip angle during the wave pass in the penetrator is used. In most situations when the nosetip begins to flow, the nosetip is eroded to blunt within one or two wave passes unless the penetrator has a length to diameter ratio of the order of less than one.

Depth of Penetration

The depth of penetration is calculated by Eqn. (43). One half of the particle velocity is used because as the compression wave expands hemispherically into the target in front of the penetrator-target interface, the particle velocity is not at its maximum. At velocities below the target flow initiation velocity, the target will compress and then rebound. It is assumed that no permanent deformation is obtained until the target has begun to flow.

$$L_{cf} = \sum_{i=1}^{n} \left[if\ U_{tf}^{i} > 0\ then\ (U_{tf}^{i} + \frac{U_{pt}^{i}}{2})\ \Delta t^{i}\ else\ 0 \right] \qquad (43)$$

where

L_{cf} = final crater depth minus the final and initial transients.

U_{tf}^{i} = target flow velocity during the i^{th} wave cycle.

U_{pt}^{i} = target particle velocity during the i^{th} wave cycle.

Δt^{i} = time for the shock wave in the penetrator to start at the penetrator-target interface, travel to the free end and return to the interface during the i^{th} wave cycle.

n = number of wave cycles.

Standing Shock Waves

The penetrator compression wave travels at a velocity equal to V_{sp} relative to the undisturbed penetrator material (Fig. 3). The compression wave velocity relative to the

penetrator-target interface is $V_{sp} - U_{pf} - U_{pp}$ (Fig. 8a). This indicates that if the impact velocity is high enough to cause the penetrator to have a flow velocity plus particle velocity equal to the speed of sound, the compression wave cannot move into the penetrator. Under these conditions the shock wave will remain at the penetrator-target interface as a standing shock wave. At impact velocities above this value, the speed of the wave increases so that it is equal to the flow velocity plus particle velocity ($V_{sp} = U_{pf} + U_{pp}$). Therefore, the penetrator will not decelerate because the free end of the penetrator cannot receive signals from the interface until the interface reaches the free end.

Likewise, the target compression wave is traveling at V_{st} relative to a fixed observed. But relative to a fixed penetrator-target interface, the wave is moving at a velocity of $V_{st} - U_{tf} - U_{pt}$ (Fig. 8a).

When the target flow velocity plus the particle velocity equals the speed of the wave, the target wave cannot propagate away from the penetrator-target interface and signal the target that the penetrator is approaching. The target wave velocity, V_{st}, is equal to the target flow velocity plus particle velocity, $U_{tf} + U_{pt}$, for this condition.

CHAPTER 5

INFLUENCE OF PENETRATOR NOSETIP SHAPE

In the nose region of the penetrator, for a sufficiently small scale, the nosetip is blunt even if the penetrator is very sharp. This small region at the centerline of the penetrator causes some different conditions to exist such as premature flowing of the nosetip. The nosetip will flow, from the center point, at a substantially lower velocity than would have been predicted by the penetrator-target interface momentum equation for angled nosetips. Further, when the penetrator begins to flow the nosetip angle will change, and therefore alter the penetrator-target interface conditions. These two modifications are discussed in the following sections.

Penetrator Flow Initiation

The penetrator-target interface momentum equation for angled nosetips, Eqn. (42), is correct for the entire penetrator area. However, in the region near the centerline of the penetrator, no matter what the penetrator nosetip angle, the penetrator nosetip will appear blunt to an incoming flow (Fig. 11). A penetrator of the same material with an angled nosetip will begin to flow at the centerline

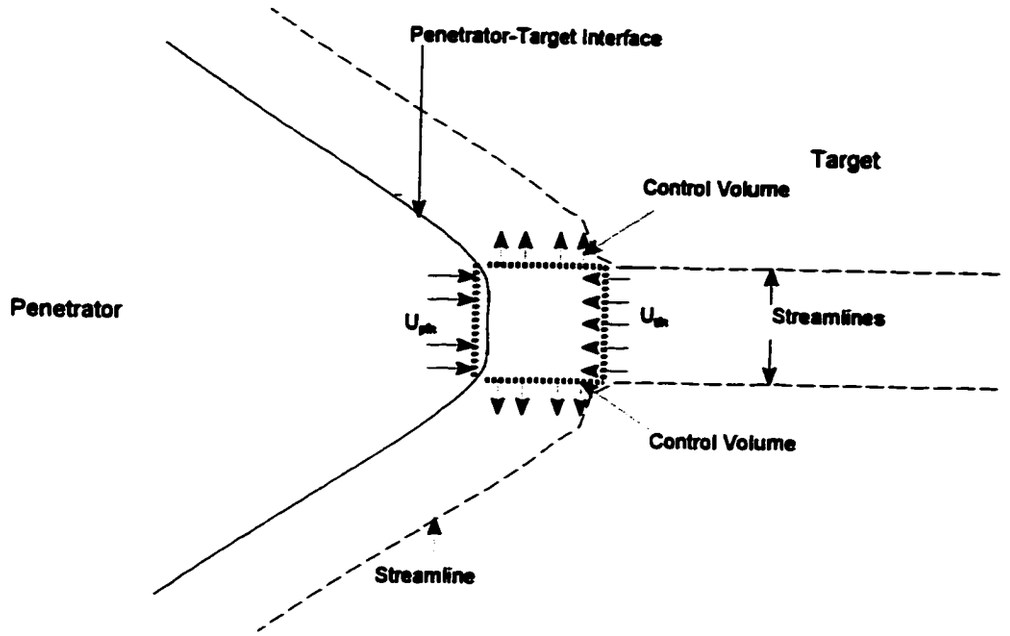

Fig. 11. Control Volume for Conservation of Momentum Integral Analysis Along the Centerline of a Conical Penetrator

for penetrator velocities above the value for which a blunt penetrator begins to flow, but below what the whole angled nosetip will flow. The blunt nosetip form of the interface momentum equation, Eqn. (39), is used

$$P_p' + \rho_p' U_{pfn}^2 = P_t' + \rho_t' U_{tfn}^2 \qquad (44)$$

The velocity component kinematic relationship becomes

$$V_p = U_{pfn} + U_{tfn} + U_{pt} + U_{pp} \qquad (45)$$

where

U_{pfn} = penetrator centerline flow velocity.

U_{tfn} = target centerline flow velocity.

The target maximum allowable stress terms, Eqns. (30-32), are used in the equation with the value of the average

nosetip turning angle θ equal to the penetrator average nosetip turning angle because the target material that enters the control volume can be stressed only to the maximum limit from Eqns. (30-32) without flowing. Fig. 11 assumes a conical nosetip that is flat at the point. As can be seen from comparing Eqn. (44) to Eqn. (42), U_{pfn} is equal to U_{pf} only when the nosetip is totally blunt.

The final penetrator length equation, Eqn. (19), is modified to be

$$L_p = L_{pI} - \sum_{i=1}^{n} [(U_{pfn}^i + U_{pp}^i)\Delta t_1^i + (U_{pfn}^i - U_{pp}^i)\Delta t_2^i] \qquad (46)$$

Consider for example, a steel penetrator with a 3 CRH ogive nosetip (θ = 17.7 degrees) impacting an aluminum target. Using the velocity component kinematic equation, Eqn. (21), with Eqn. (44), the velocity at which the nosetip will begin to flow at the nosetip centerline is

$$V_{pfi} = \sqrt{\frac{S_p' - S_t'}{\rho_t'}} + U_{ptm} + U_{ppm} \qquad (47)$$

where V_{pfi} = impact velocity for flow initiation at the nosetip centerline.

This equation is accurate only for penetrator maximum stress, S_p', greater than target maximum stress, S_t'. The total nose penetrator flow velocity, U_{pf} in Eqn. (42), is greater than zero when the impact velocity is approximately

3500 m/s, but the centerline nose penetrator flow velocity, U_{pfn}, is greater than zero when the impact velocity is approximately 1300 m/s. A fully blunt nosetip will begin to flow at 850 m/s, meaning that the whole nose from the centerline to the outer radius of the nosetip would flow if the impact velocity were greater than 3500 m/s. At an impact velocity of 1300 m/s the outer regions of the nosetip would not flow, but near the centerline of the nosetip, the nosetip would begin to flow. This is something of a degenerate condition as is discussed in the next section.

Penetrator Flow Influence on Nosetip Angle

The nosetip flow at the centerline will change the average nosetip angle which, in turn, changes the conditions at the penetrator-target interface. As the nosetip blunts, the average nosetip angle increases, the interface pressure increases and the nose penetrator flow velocity increases, causing the nosetip to blunt more rapidly. This degenerate condition stops only if the penetrator becomes fully blunt or if the compression wave returns from the free end of the penetrator and reduces the velocity of the penetrator. As an example of how the penetrator nosetip angle changes with the flowing nosetip, Table 1 presents the changing nosetip angle as a function of the length of the nose (L_n) divided by the initial nose length(L_{nI}) for a 3 CRH nosetip. A value

of zero for L_n/L_{nI} means an undeformed penetrator, and a value of one indicates the nosetip is blunt.

Table 1. Average Nosetip Angle for a 3 CRH Nosetip as a Function of Nosetip Length

L_n/L_{nI}	Nosetip Angle Degrees
0.0	17.7
0.1	20.2
0.2	26.6
0.3	35.6
0.4	46.1
0.5	57.0
0.6	67.5
0.7	76.6
0.8	83.7
0.9	88.3
1.0	90.0

It is more efficient to use a curve fit for the above data than to use tabled data and interpolate. This study uses a curve fit and an average of the average nosetip angle during the compression wave cycle.

CHAPTER 6

PENETRATOR/TARGET RESPONSE REGIMES

There are eight different penetrator/target response regimes that can occur under the appropriate impact conditions as shown in Table 2. The regime which exists for a given set of conditions is dependent upon several factors including penetrator and target strength, penetrator velocity, Poisson's ratio for the penetrator and target, and the speed of sound in the penetrator and target.

As an example, assume that a conical nosetip penetrator impacts a target with sufficient velocity so that it is in Regime 5. That is, the penetrator is flowing at its centerline, $U_{pfn} > 0$, but the rest of the nosetip is not flowing, $U_{pf} = 0$, and the target is flowing with a lower velocity than the sound velocity. The penetrator compression wave travels to the rear of the penetrator and returns as an expansion wave. During this event, the conical nosetip has been blunting and the pressure on the front of the penetrator has been increasing. At some point, the increase in pressure will cause the rest of the penetrator to begin to flow, and the impact will move into

Table 2. Penetrator/Target Response Regimes

REGIME	PENETRATOR	TARGET
1	$V_{sp} = U_{pf} + U_{pp}$ $U_{pf} > 0$ Standing Shock	$V_{st} = U_{tf} + U_{pt}$ $U_{tf} > 0$ Standing Shock
2	$V_{sp} = U_{pf} + U_{pp}$ $U_{pf} > 0$ Standing Shock	$V_{st} > U_{tf} + U_{pt}$ $U_{tf} > 0$ Target Flowing
3	$V_{sp} > U_{pf} + U_{pp}$ $U_{pf} > 0$, $U_{pfn} > 0$ Penetrator Flowing	$V_{st} = U_{tf} + U_{pt}$ $U_{tf} > 0$ Standing Shock
4	$U_{pf} > 0$, $U_{pfn} > 0$ Penetrator Flowing	$U_{tf} > 0$ Target Flowing
5	$U_{pf} = 0$, $U_{pfn} > 0$ Penetrator Centerline Flowing	$U_{tf} > 0$ Target Flowing
6	$U_{pf} = 0$, $U_{pfn} = 0$ Penetrator Not Flowing	$U_{tf} > 0$ Target Flowing
7	$U_{pf} > 0$, $U_{pfn} > 0$ Penetrator Flowing	$U_{tf} = 0$ Target Not Flowing
8	$U_{pf} = 0$, $U_{pfn} = 0$ Penetrator Not Flowing	$U_{tf} = 0$ Target Not Flowing

Regime 4. In Regime 4, the penetrator is flowing along the whole nose region from the centerline to the outer radius. When the penetrator wave returns to the interface, the penetrator velocity is decreased by 2 U_{pp} (the penetrator deceleration term). The flow velocities are assumed to adjust instantaneously to the new conditions. If after this or additional wave cycles in which the penetrator further decelerates, the target may stop flowing ($U_{tf} = 0$), but the penetrator continues to flow. This condition corresponds to

Regime 7. With additional penetrator deceleration the penetrator will turn off, that is, cease to flow ($U_{pf} = 0$), at which time it will move into Regime 8 where both the target and penetrator are not flowing. The terminal impact process will remain in this regime until the penetrator stops.

The foregoing is a hypothetical example. Many routes through the regimes are possible depending upon impact conditions and material property factors. Standing shocks occur only at very high velocity impacts because the speed of sound in many structural materials is above 4000 m/s. These same equations apply for all regimes, but they may apply differently in different regimes.

The following sections address how the equations are applied in each regime. Four of the equations--the velocity component kinematic relationship, interface momentum, and the two conservation of mass equations across the disturbance waves--apply in all regions in the following form

$$V_p = U_{pf} + U_{pp} + U_{tf} + U_{pt} \tag{21}$$

$$P_p' + \rho_p' U_{pf}^2 = \rho_t' U_{tf}^2 (1 - \cos\theta) + P_t' \tag{42}$$

$$\rho_p' = \rho_p \left(\frac{V_{sp}}{V_{sp} - U_{pp}} \right) \tag{2}$$

$$\rho_t' = \rho_t \left(\frac{V_{st}}{V_{st} - U_{pt}} \right) \tag{27}$$

Regime 1

Since both the penetrator and the target have standing shocks, the speeds of the two shock waves are

$$V_{sp} = U_{pf} + U_{pp} \tag{48}$$

$$V_{st} = U_{tf} + U_{pt} \tag{49}$$

In this regime, both the target and the penetrator are flowing so that P_p' and P_t' are at their maximum values

$$P_p' = S_p' = \rho_p U_{ppm} V_{sp} = \frac{\sigma_{sp}}{v_p} \tag{50}$$

$$P_t' = S_t' = \rho_t U_{ptm} V_{st} = \frac{\sigma_{st}}{v_t^{1+\sin\theta}} \tag{51}$$

At the velocities required in this regime, any nosetip will blunt(θ = 90 Deg., $U_{pfn} = U_{pf}$) within a small time, so that assuming a blunt nosetip is valid and it simplifies the equations. Substituting Eqns. (2), (27), (48), (49), (50), and (51) into the conservation of momentum equation, Eqn. (42), and simplifying we have

$$\frac{\sigma_{sp}}{v_p} + \rho_p (U_{pf} + U_{pp}) U_{pf} = \frac{\sigma_{st}}{v_t^2} + \rho_t (U_{tf} + U_{pt}) U_{tf} \tag{52}$$

There are 10 unknowns in this problem: U_{pf}, U_{pp}, V_{sp}, ρ_p', P_p', U_{tf}, U_{pt}, V_{st}, ρ_t', P_t'. There are also 10 equations as follows:

One velocity component kinematic relationship,

Eqn. (21).

Two strength of shock wave-stress in the material

equations, Eqns. (50) and (51).

Two maximum stress in the material equations, Eqns. (50) and (51)(Eqns. (50) and (51) are actually four equations).

One conservation of momentum equation across the penetrator-target interface, Eqn. (42).

Two conservation of mass equations across the compression and expansion waves, Eqns. (2) and (27).

Two compression wave speed of sound equations, Eqns. (48) and (49).

Since there are 10 equations and 10 unknowns, a unique solution exists. Some interesting simplifications can be made by observing the time for shock wave traversal. Since there is a standing wave in the penetrator, the time for wave traversal is equal to the time for the wave to travel to the end of the penetrator

$$\Delta t_1 = \frac{L_p^i}{V_{sp}} = \frac{L_{pI}}{U_{pf} + U_{pp}} = \Delta t_t \qquad (53)$$

Using this time, the crater depth without initial or final transients is equal to

$$L_c^{i+1} = L_c^i + (U_{tf} + U_{pt})\,\Delta t_t \qquad (54)$$

since there is only a single wave pass, $L_c^i = 0$. Expressions for the initial and final transients are developed in Chapter 7.

Regime 2

Since there is a standing shock wave in the penetrator and a moving compression wave in the target, the equations for wave speed are

$$V_{sp} = U_{pf} + U_{pp} \tag{48}$$

$$V_{st} = C_{ot} + S_{it} U_{pt} \tag{55}$$

Since in this region the penetrator and target are both flowing and both are at their maximum stress levels

$$P_p' = S_p' = \rho_p U_{ppm} V_{sp} = \frac{\sigma_{sp}}{\nu_p} \tag{50}$$

$$P_t' = S_t' = \rho_t U_{ptm} V_{st} = \frac{\sigma_{st}}{\nu_t^{1+\sin(\theta)}} \tag{51}$$

As in Regime 1, the nosetip will have little effect due to the nosetip becoming quickly blunted (θ= 90, $U_{pfn} = U_{pf}$). Substituting Eqns. (2), (27), (48), (56), (50), and (51) into Eqn. (42), we have

$$\frac{\sigma_{sp}}{\nu_p} + \rho_p (U_{pf} + U_{pp}) U_{pf} = \frac{\sigma_{st}}{\nu_t^2} + \rho_t' U_{tf}^2 \tag{56}$$

There are 10 unknowns and equations as in Regime 1, with the exception that the speed of sound in the target is calculated from Eqn. (55) instead of Eqn. (49) since the target compression wave is not a standing wave.

Since there is a standing compression wave in the penetrator, the same simplifying assumptions that applied in

Regime 1 to the crater depth and time calculations, Eqns. (53) and (54), also apply here.

Regime 3

Since there is a standing shock in the target and a flowing penetrator, the equations for wave velocity are

$$V_{sp} = C_{op} + S_{ip} U_{pp} \tag{57}$$

$$V_{st} = U_{tf} + U_{pt} \tag{49}$$

Because both the target and the penetrator are flowing, P_p' and P_t' are at their maximum values as given by Eqns. (50) and (51). As in Regions 1 and 2, the penetrator will blunt($\theta = 90$, $U_{pfn} = U_{pf}$) extremely quickly at the velocities required in this region. Substituting Eqns. (2), (27), (57), (49), (50), (51) into Eqn. (42) yields

$$\frac{\sigma_{sp}}{v_p} + \rho_p' U_{pf}^2 = \frac{\sigma_{st}}{v_t^2} + \rho_t (U_{tf} + U_{pt}) U_{tf} \tag{58}$$

Again, there are the same 10 unknowns and equations as in Regime 1 with the exception that the speed of sound in the penetrator is calculated from Eqn. (57) instead of Eqn. (48). Since the penetrator does not have a standing shock wave, the simplifying assumptions used in Regimes 1 and 2 do not apply for the crater depth and time. Instead, Eqns. (15), (16), (43), (46) are used to solve for the crater depth, time to end of impact, and final length of penetrator.

Regime 4

This is the most common regime because with typical ballistic materials (steels, tungsten, etc.), the penetrator and target begin to flow when the impact velocity is approximately 600 m/s for a blunt penetrator. The material sound velocities are typically above 4500 m/s, yielding a large impact velocity range covered by this regime.

Angled nosetips pose a different problem in this regime. As the penetrator blunts, the average nosetip angle, θ, will increase. This increase will affect the penetrator-target interface conditions while the compression wave travels down the penetrator and returns as an expansion wave. One way of accounting for this condition is to take small steps in time and track the compression/expansion wave in the penetrator and change the average nosetip angle as the penetrator blunts. At each time step, the interface conditions with the new average nosetip angle are calculated until the penetrator is fully blunt. At that point, the quasi-steady process can take over where the conditions at the penetrator-target interface do not change during a wave cycle. Another solution method is to use an average of the average nosetip angle during the wave cycle. This method allows an easier solution to the region and is almost as accurate.

Because both the target and penetrator are flowing, the disturbance wave velocities are given by Eqns. (55) and (57), and P_p' and P_t' are at their maximum values given by Eqns. (50) and (51). The average nosetip angle, θ, is

$$\theta = \frac{1}{A_p}\int_0^{A_p} \theta_p \, dA \tag{22}$$

Substituting Eqns. (50) and (51) into Eqn. (42) yields

$$\frac{\sigma_{sp}}{\nu_p} + \rho_p' U_{pf}^2 = \frac{\sigma_{st}}{\nu_t^{1+\sin\theta}} + \rho_t' U_{tf}^2 (1 - \cos\theta) \tag{59}$$

Substituting Eqns. (50) and (51) into Eqn. (44) yields

$$\frac{\sigma_{sp}}{\nu_p} + \rho_p' U_{pfn}^2 = \frac{\sigma_{st}}{\nu_t^{1+\sin(\theta)}} + \rho_t' U_{tfn}^2 \tag{60}$$

By comparing Eqn. (60) with Eqn. (59), it can be seen that the penetrator centerline velocity, U_{pfn}, will only equal the penetrator flow velocity when then the penetrator is totally blunt.

There are now 13 unknowns, the 10 original plus θ, U_{pfn}, U_{tfn}. There are now 13 equations, the 10 original except Eqns. (57) and (55) instead of Eqns. (48) and (49) plus

One average nosetip angle equation, Eqn. (22).

One centerline interface equation, Eqn. (45).

One centerline velocity component kinematic equation

$$V_p = U_{pfn} + U_{pp} + U_{tfn} + U_{pt} \tag{61}$$

Eqns. (15), (16), (43), (46) are used to solve for the crater depth, time to end of impact, and final length of penetrator.

Regime 5

In this regime the centerline of the penetrator is flowing, $U_{pfn} > 0$, while the rest of the penetrator is not flowing, $U_{pf} = 0$. The pressure at the penetrator-target interface is sufficiently low that the penetrator does not flow anywhere except at the centerline, but the pressure is high enough to cause the target to flow around the penetrator. This effect will occur only if the penetrator has an angled nosetip. Because the penetrator is not flowing for most of its frontal area and the target is flowing, the equations become

$$P_p' = \rho_p U_{pp} V_{sp} < \frac{\sigma_{sp}}{\nu_p} \tag{62}$$

$$S_p' = \rho_p U_{ppm} V_{sp} = \frac{\sigma_{sp}}{\nu_p} \tag{63}$$

$$P_t' = S_t' = \rho_t U_{ptm} V_{st} = \frac{\sigma_{st}}{\nu_t^{1+\sin\theta}} \tag{51}$$

The maximum penetrator stress must be achieved in order for the centerline of the penetrator to flow.

The average nosetip angle is calculated from Eqn. (22). As in Regime 4, quasi-steady pressure at the penetrator-target interface will not occur until the penetrator becomes blunt. Since the penetrator centerline is always flowing in this regime and the rest of the penetrator is not, quasi-steady pressure at the penetrator-target interface will not be attained. The impact will usually progress from this regime to Regime 4. This change occurs because as the penetrator blunts, the pressure at the penetrator-target interface increases to the point where the entire penetrator nose will begin to flow unless the penetrator decelerates enough to stop the penetrator from flowing at the penetrator centerline.

In this regime, as in Regime 4, a method such as small time steps or an average of the average nosetip angle must be used for the calculations. Substituting Eqns. (61) and (51) into Eqn. (42) gives

$$\rho_p U_{pp} V_{sp} = \frac{\sigma_{st}}{\nu_t^{1+\sin\theta}} + \rho_t' U_{tf}^2 (1 - \cos\theta) \qquad (64)$$

Again, Eqns. (15), (16), (43), (46) can be used to solve for the crater depth, time to end of impact, and final length of penetrator.

Regime 6

In this regime, the pressure at the penetrator-target interface is sufficiently low so that the penetrator does

not flow, $U_{pfn} = 0$ and $U_{pf} = 0$. However, the pressure is high enough to cause the target to flow around the penetrator. Because the penetrator is not flowing, the stress is below the maximum stress. The equations become

$$P_p' = \rho_p U_{pp} V_{sp} < \frac{\sigma_{sp}}{\nu_p} \tag{62}$$

$$P_t' = S_t' = \rho_t U_{ptm} V_{st} = \frac{\sigma_{st}}{\nu_t^{1+\sin\theta}} \tag{51}$$

The wave speeds are as in Regime 4. It is noted that U_{pp} is a variable since the compressive stress is now less than its maximum value, Eqn. (62). The penetrator compressive stress is equal to the pressure at the penetrator-target interface. Since U_{pp} is decreasing, the density ratio approaches unity. The average nosetip angle is calculated from Eqn. (22).

Substituting Eqns. (62) and (51) into Eqn. (42) gives the following equation

$$\rho_p U_{pp} V_{sp} = \frac{\sigma_{st}}{\nu_t^{1+\sin\theta}} + \rho_t' U_{tf}^2 (1 - \cos\theta) \tag{64}$$

This regime is commonly associated with a high-strength, high-density penetrator and a low-strength, low-density target. The penetrator must be strong enough to overcome the confined strength of the target. Again, Eqns. (15), (15), (43), and (46) can be used to solve for the

crater depth, time to end of impact, and final length of the penetrator.

Regime 7

In this regime the penetrator is flowing, $U_{pf} > 0$ and $U_{pfn} > 0$, but the target is not flowing, $U_{tf} = 0$. The stress term in the penetrator is at the maximum value, but the stress term in the target is less than its maximum value.

$$P_p' = S_p' = \rho_p U_{ppm} V_{sp} = \frac{\sigma_{sp}}{\nu_p} \tag{50}$$

$$P_t' = \rho_t U_{pt} V_{st} < \frac{\sigma_{st}}{\nu_t^{1+\sin\theta}} \tag{65}$$

The wave speeds are given by Eqns. (55) and (57). In this case U_{pt} is now a variable because the pressure at the penetrator-target interface is not large enough to produce the maximum strength compressed wave allowable. The increased density in the target is no longer at its maximum since U_{pt} is less than its maximum. The increased density approaches the unstressed target density as U_{pt} decreases. The average nosetip angle is calculated by Eqn. (22) and time stepping or an average of the average nosetip angle must be used for each wave cycle. Substituting Eqns. (50) and (65) into Eqn. (42) yields

$$\frac{\sigma_{sp}}{\nu_p} + \rho_p' U_{pf}^2 = \rho_t U_{pt} V_{st} \tag{66}$$

Also substituting Eqns. (51) and (65) into (44) yields

$$\frac{\sigma_{sp}}{\nu_p} + \rho_p' U_{pfn}^2 = \rho_t U_{pt} V_{st} \qquad (67)$$

By comparing Eqns. (66) and (67) it can be seen that the flow at the penetrator centerline is equal to penetrator flow term ($U_{pfn} = U_{pf}$). Eqns. (15), (16), (43), and (46) are used to solve for the crater depth, time to end of impact, and final length of penetrator.

Regime 8

In this regime neither the penetrator nor the target is flowing. If the penetrator is not fully consumed in the impact, it must always terminate in this regime. The pressure at the penetrator-target interface for this regime is lower than for any other regime. The stress in the penetrator and the target are both less than the maxima as follows:

$$P_p' = \rho_p U_{pp} V_{sp} < \frac{\sigma_{sp}}{\nu_p} \qquad (62)$$

$$P_t' = \rho_t U_{pt} V_{st} < \frac{\sigma_{st}}{\nu_t^{1+\sin\theta}} \qquad (65)$$

The average nosetip angle is calculated from Eqn. (22). Substituting Eqns. (62) and (65) into Eqn. (42) yields

$$\rho_p U_{pp} V_{sp} = \rho_t U_{pt} V_{st} \qquad (68)$$

Eqns. (15), (16), (43), and (46) are used to solve for the crater depth, time to end of impact, and the final length of the penetrator.

Regime Determination

One method to determine which regime characterizes a specific impact condition is to calculate the minimum penetrator velocities required to flow the target(V_{tfi}), penetrator(V_{pfi}), and centerline penetrator(V_{pfni}). The average nosetip angle must be calculated from Eqn. (22). The maximum penetrator and target stresses (S_p' and S_t') and the maximum penetrator and target velocities (U_{ptm} and U_{ppm}) are also needed.

For the condition of S_p' greater than S_t', the target will flow before the penetrator. The velocity component kinematic equation is used in the determination of the target flow initiation velocity,

$$V_p = U_{pf} + U_{tf} + U_{pp} + U_{pt} \tag{21}$$

as is the penetrator-target interface momentum equation,

$$P_p' + \rho_p' U_{pf}^2 = P_t' + \rho_t' U_{tf}^2 (1 - \cos\theta) \tag{59}$$

Solving for the penetrator velocity that will just flow the target, the target particle velocity is at its maximum while the penetrator particle velocity will be less than its maximum. The penetrator particle velocity is obtained by solving for U_{pp} in the penetrator-target interface equation.

$$\rho_p U_{pp} V_{sp} = S_t' \tag{69}$$

The minimum penetrator velocity required to flow the target becomes

$$V_{tfi} = U_{ptm} + U_{pp} \tag{70}$$

In the determination of the minimum penetrator velocity required to flow the penetrator under these conditions, it is noted that the penetrator particle velocity will be at its maximum. The target will be flowing as shown above and the target particle velocity will be at its maximum.

$$V_{pfi} = U_{ptm} + U_{ppm} + U_{tf} \tag{71}$$

The U_{tf} in this equation is determined from the penetrator-target interface equation

$$S_p' = S_t' + \rho_t' U_{tf}^2 (1 - \cos\theta) \tag{72}$$

The penetrator velocity to just flow the penetrator centerline is determined with an equation similar to Eqn. (71)

$$V_{pfni} = U_{ptm} + U_{ppm} + U_{tfn} \tag{73}$$

The determination of U_{tfn} requires the penetrator-target interface momentum equation in the nose region which is Eqn. (44)

$$S_p' = S_t' + \rho_t' U_{tfn}^2 \tag{74}$$

With the three flow initiation velocities, the particular regime can be determined as explained below.

For the case where S_t' is greater than S_p', the penetrator will flow at a lower penetrator velocity than the target. The penetrator particle velocity will be at its

maximum whereas the target particle velocity will be less than its maximum. The penetrator velocity required to just flow the penetrator is

$$V_{pfi} = U_{pt} + U_{ppm} \tag{75}$$

The target particle velocity is found from the penetrator-target interface equation

$$S_p' = \rho_t U_{pt} V_{st} \tag{76}$$

The penetrator velocity required to flow the target is

$$V_{tfi} = U_{ptm} + U_{ppm} + U_{pf} \tag{77}$$

where the penetrator flow velocity is determined from

$$S_p' + \rho_p' U_{pf}^2 = S_t' \tag{78}$$

As can be seen in Eqn. (74) and (78), the velocity required to flow the penetrator centerline for this case is the same as the velocity to flow the whole penetrator.

In comparing the penetrator velocity, V_p, with the flow initiation velocities, it can be determined which of the eight regimes characterizes the impact events. The conditions corresponding to each of the regimes are presented in Table 3.

Table 3. Determination of Penetrator/Target Response Regimes

REGIME	Condition
1	$V_p > V_{pfni}$ and V_{pfi} and V_{tfi}, $V_{sp} = U_{pp} + U_{pf}$, $V_{st} = U_{pt} + U_{tf}$ Standing Shocks in the Penetrator and Target
2	$V_p > V_{pfni}$ and V_{pfi} and V_{tfi}, $V_{st} = U_{pt} + U_{tf}$ Standing Shock in the Target
3	$V_p > V_{pfni}$ and V_{pfi} and V_{tfi}, $V_{sp} = U_{pp} + U_{pf}$ Standing Shock in the Penetrator
4	$V_p > V_{pfni}$ and V_{pfi} and V_{tfi}
5	$V_p > V_{pfni}$ and V_{tfi} $V_p < V_{pfi}$
6	$V_p > V_{tfi}$ $V_p < V_{pfi}$ and V_{pfni}
7	$V_p > V_{pfi}$ and V_{pfni} $V_p < V_{tfi}$
8	$V_p < V_{pfi}$ and V_{pfni} and V_{tfi}

CHAPTER 7

CRATER DIAMETER, INITIAL TRANSIENT, AND FINAL TRANSIENT

The crater diameter, initial transient, and final transient are considered together because they are each a function of the same parameter, the pressure at the interface. The initial transient is the time between impact and the establishment of a quasi-steady state. The final transient is the time between the complete erosion of the penetrator and the cessation of crater formation. The crater diameter is the average crater dimension perpendicular to the crater centerline along the direction of penetration.

Crater Diameter

When the penetrator stream approaches the penetrator-target interface, it is turned by the target stream as shown in Fig. 12. Relative to the penetrator-target interface, the penetrator stream must always turn at an angle greater than 90 degrees. When the flow is turned 90 degrees, the penetrator stream pushes directly at the target walls. It is this pressure that forms the crater. From in-flight photographs and recovered projectiles it is found that the

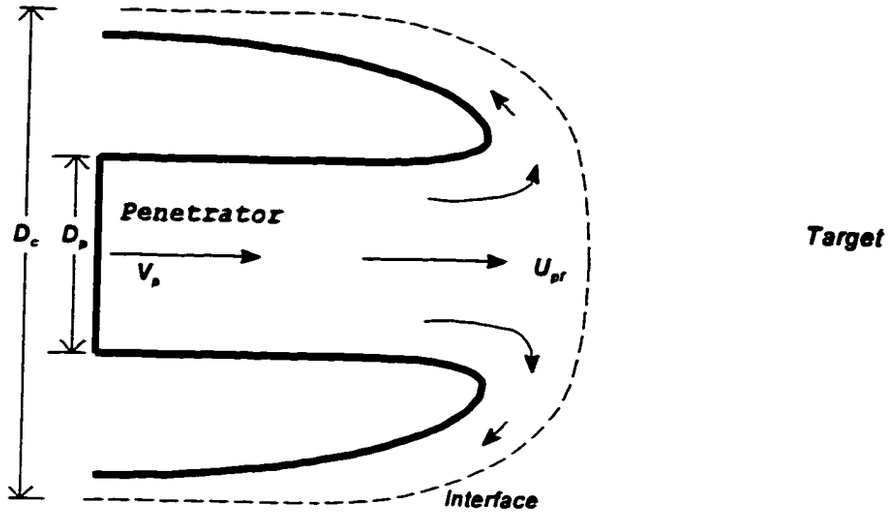

Fig. 12. Crater Diameter Formation

penetrator flows with an approximately mushroom-shaped nosetip. The pressure of the penetrator steam is assumed to push outward from the centerline against the walls of the target until the pressure has decreased to the target free-surface compressive strength. This condition is shown schematically in Fig. 13.

The force associated with the penetrator is

$$F_p = CD_p^2(\rho_p' U_{pf}^2 + \frac{\sigma_{st}}{\nu_t}) \qquad (79)$$

where

C = shape-dependent constant

$\rho_p' U_{pf}^2$ = hydrodynamic pressure from the penetrator at the penetrator-target interface

σ_{st}/ν_t = free surface stress in the target

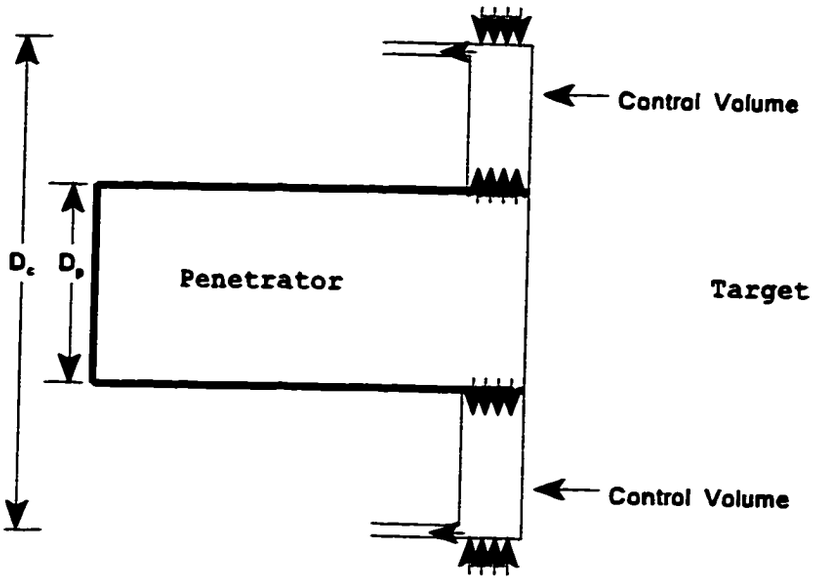

Fig. 13. Sectional View of Crater Diameter Formation

The amount of force that the target can resist without flowing is

$$F_t = \frac{\sigma_{st}}{\nu_t} C D_c^2 \tag{80}$$

where

D_c = diameter of the crater

The crater diameter corresponds to the lateral dimension where the net forces in the penetrator stream and target are equal. Applying the radial conservation of momentum equation to the control volume shown in Fig. 13

$$C D_p^2 (\rho_p' U_{pf}^2 + \frac{\sigma_{st}}{\nu_t}) = C \frac{\sigma_{st}}{\nu_t} D_c^2 \tag{81}$$

Solving for the ratio of D_c to D_p

$$\frac{D_c}{D_p} = \sqrt{1 + \frac{\rho_p' U_{pf}^2}{\frac{\sigma_{st}}{\nu_t}}} \qquad (82)$$

The ratio of D_c to D_p must always be greater than unity since the penetrator must be able to fit into the crater.

Initial Transient

At the instant of impact, before either the penetrator or the target have begun to flow, a large Hugoniot impact pressure is generated at the penetrator-target interface. As the penetrator and the target begin to flow in response to this high pressure, the pressure decreases until it reaches the maximum sustainable, free surface value in the penetrator, σ_{sp}/ν_p, and the maximum confined stress in the target, σ_{st}/ν_t^2. This is accomplished by the passage of high pressure shock waves in each material which decrease in strength to their sustained values. The confined stress is used in the target because the stress must exceed the confined stress to penetrate into the target. Fig. 14 illustrates a blunt penetrator initial transient, and Fig. 15 illustrates a conical penetrator initial transient. The pressure on the penetrator side of the interface after shock passage is equal to the Hugoniot pressure

$$P_{ph}' = \rho_p U_{pph} V_{sph} \qquad (83)$$

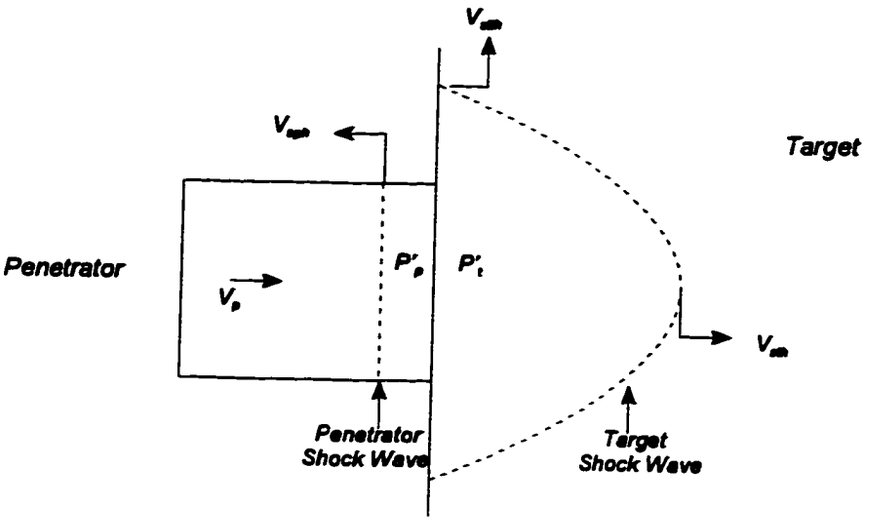

Fig. 14. Initial Transient Formation For a Blunt Nosetip

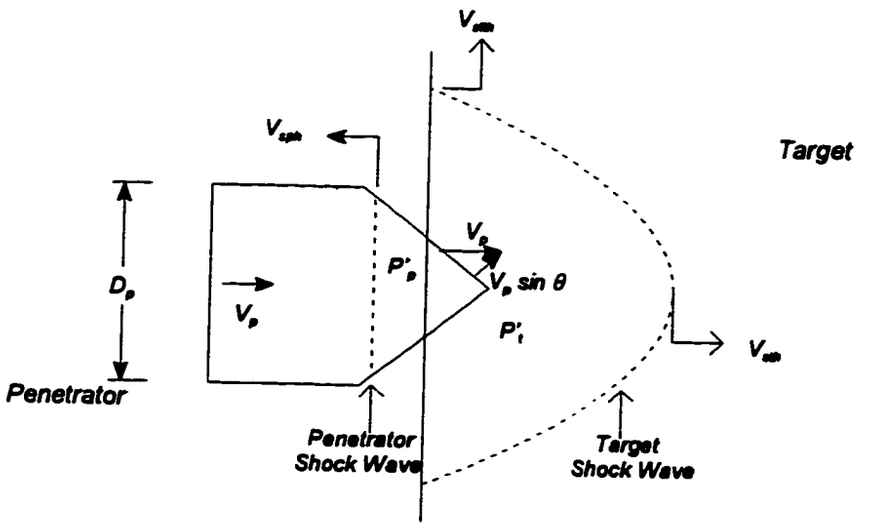

Fig. 15. Initial Transient Formation For a Conical Nosetip

where

U_{pph} = Hugoniot particle velocity in the penetrator.

V_{sph} = Hugoniot speed of sound = $C_{op} + S_{ip}\ U_{pph}$.

On the target side of the penetrator-target interface the pressure is equal to

$$P'_{th} = \rho_t U_{pth} V_{sth} \tag{84}$$

where

U_{pth} = Hugoniot particle velocity in the target.

V_{sth} = Hugoniot speed of sound = $C_{ot} + S_{it}\ U_{pth}$.

The pressures on each side of the interface are equal so that initially

$$\rho_p U_{pph} V_{sph} = \rho_t U_{pth} V_{sth} \tag{85}$$

From the velocity component kinematic relationship, a relative equation is obtained

$$V_p \sin\theta = U_{pph} + U_{pth} \tag{86}$$

The time for the initial transient is taken to be the time for the passage of the lateral release wave in the penetrator

$$\Delta t_{it} = \frac{r_p}{V_{spht}} \tag{87}$$

where

V_{spht} = penetrator transverse Hugoniot shock velocity.

= $C_{opt} + S_{ip}\ U_{pph}$.

C_{opt} = transverse zero pressure speed of sound.

The crater length due to the initial transient is given by

$$\begin{aligned} &\text{if } U_{pth} < U_{ptm} \quad \text{then} \quad L_{cI} = 0 \\ &\text{if } U_{pth} > U_{ptm} \quad \text{then} \quad L_{cI} = (U_{pth} - U_{ptm})\,\Delta t_{it} \end{aligned} \tag{88}$$

The length of the penetrator eroded during the initial transient expansion is

$$\begin{aligned} &\text{if } U_{pph} < U_{ppm} \text{ then} \quad \Delta L_{pI} = 0 \\ &\text{if } U_{pph} > U_{ppm} \text{ then} \quad \Delta L_{pI} = -(U_{pph} - U_{ppm})\,\Delta t_{it} \end{aligned} \tag{89}$$

Final Transient

Two possible conditions may exist at the termination of an impact. These are zero penetrator velocity or zero penetrator mass. As the penetrator decelerates, the pressure at the penetrator-target interface decreases as the velocity decreases until the pressure is zero corresponding to zero velocity. However, if the penetrator is consumed before the velocity is zero, there is still pressure at the interface that will expand into the target if it exceeds the target's free surface maximum strength. There are two contributions to the terminal crater formation, the high pressure region formed by the flowing penetrator and the expansion of the target particle momentum. The high pressure region is assumed to expand until it reaches the free surface maximum strength in the target, σ_{st}/ν_t.

The penetrator flow velocity is the principal factor in the final transient as the energy of the penetrator is transferred into the target flow (Fig. 16). When the penetrator is consumed, the target is usually still flowing. Applying the conservation of momentum over a control volume

$$C r_p^2 \rho_p' U_{pf}^2 = C r_f^2 \frac{\sigma_{st}}{\nu_t} \tag{90}$$

where C = shape dependent constant.

The right hand side is the expression for the force at full expansion, and r_f is the final radius.

When solved for the ratio r_f/r_p

$$\frac{r_f}{r_p} = \sqrt{\frac{\rho_p' U_{pf}^2}{\sigma_{st}/\nu_t}} \tag{91}$$

From Fig. 16, it is observed that because of the point at which the expansion was started, the radius of the penetrator must be subtracted from r_f to obtain the final transient equation

$$\frac{L_{ctpf}}{r_p} = \sqrt{\frac{\rho_p' U_{pf}^2}{\sigma_{st}/\nu_t}} - 1 \tag{92}$$

where

L_{ctpf} = crater depth formed by the penetrator flow term of the final transient.

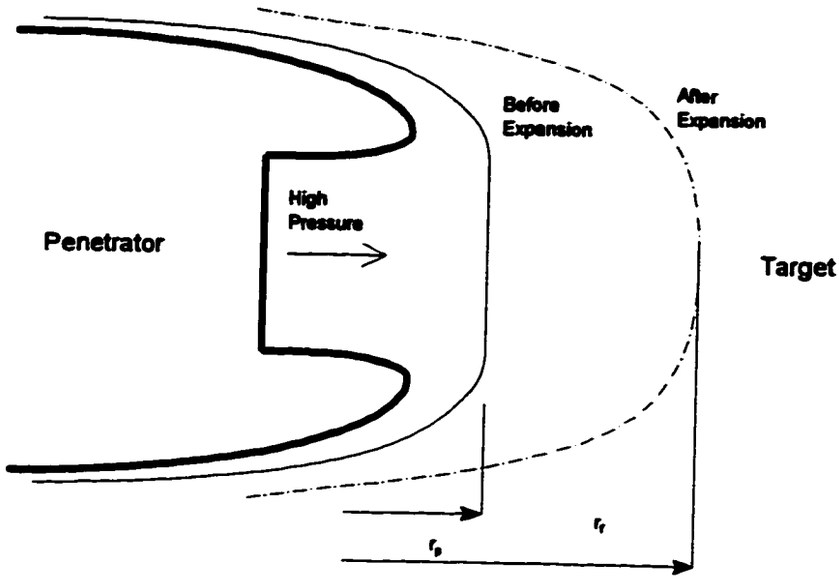

Fig. 16. Penetrator Flow Momentum Terminal Transient Formation

The other part of the terminal transient comes from the expansion of the target particle momentum. Applying the conservation of momentum (Fig. 17)

$$\rho_t' U_{pt}^2 C r_p^2 = \rho_{tfs}' U_{ptfs}^2 C r_c^2 \qquad (93)$$

where

U_{ptfs} = free surface target particle velocity.

ρ_{tfs}' = free surface target density.

From Fig. 17, the crater length formed by the target particle momentum is

$$\frac{r_c - r_p}{L_{ctpm}} = \frac{V_{stt}}{V_{st}} \qquad (94)$$

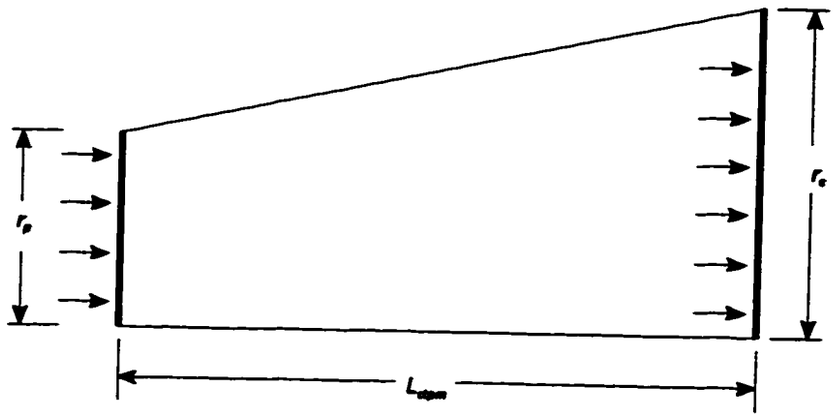

Fig. 17. Target Particle Momentum Expansion Terminal Transient Formation

Solving Eqns. (93) and (94) together for L_{ctpm}

$$L_{ctpm} = r_p \frac{V_{st}}{V_{stt}} \left(\frac{U_{pt}}{U_{ptfs}} \sqrt{\frac{\rho_t'}{\rho_{tfs}'}} - 1\right) \tag{95}$$

The total crater length due to the terminal transient is the sum of the two separate transient terms.

$$L_{final} = L_{ctpm} + L_{ctpf} \tag{96}$$

In the calculation procedure, a final transient is calculated for each wave pass. This final transient is added to the initial transient plus developed crater depth and is checked to determine if this total depth is greater than the total depth for the previous wave pass. The greater depth is used as the new maximum crater depth. However, this value is used only when the penetrator is finally consumed and is not additive at each wave pass. This procedure recognizes the fact that in the case of rapid

penetrator deceleration, the maximum terminal transient may not be generated by the final wave. That is, the transient generated at some wave pass before the final wave pass could contribute to a crater depth greater than that caused by an subsequent wave pass plus its transient. Therefore, for the i^{th} wave pass, this is illustrated as follows:

$$L_c^i = L_{initial} + L_{cf}^i + L_{final}^i$$
$$If\ L_c^i > L_{cm}\ then\ L_{cm} = L_c^i \qquad (97)$$

where

L_{cm} = maximum crater depth from previous wave passes.

L_c^i = total crater depth at the i^{th} time step resulting from the current transient if the penetrator was consumed.

L_{cf}^i = crater depth formed by the penetrator in the quasi-steady (developed) state condition.

$L_{initial}$ = crater depth formed by the initial transient.

L_{final}^i = crater depth formed by the transient if this is the final wave pass.

The crater depth, L_{cm}, is therefore updated for each wave pass and becomes the local maximum as if it were the final pass. The final value of L_{cm} is the final crater depth if the penetrator is consumed.

CHAPTER 8

CERAMIC, CONCRETE, AND GEOLOGIC TARGETS

It has been observed from experiments conducted at Louisiana Tech University that for a range of impact velocities, when a high-strength penetrator with an ogive nosetip penetrates into a low-strength target, such as tool steel into soft aluminum, the penetrator does not deform and can be recovered without even the tool marks upon its surface being removed. Non-deformation of the nosetip also occurs for blunt nosetips, depending on penetrator strength, up to impact velocities of several hundred meters/second. For ogive and conical nosetips, non-deformation may exist for impact velocities above a kilometer/second. However, such is not the case for concrete and certain geologic targets which, even with their comparatively low densities and strengths, tend to erode the penetrator nosetips at relatively low impact velocities. It has been observed that nosetip erosion begins at velocities lower than 300 m/s for a high strength steel penetrator with an ogive nosetip into concrete or grout (Ref. 13).

The ballistic properties of ceramic targets are of great interest in such diverse applications as bulletproof

vests and tank armor. Ceramics appear to provide significant advantage over metals for some impact conditions.

Concrete and Geologic Targets

Significant erosion in the nose region of high-strength projectiles is observed for impact velocities above 350 m/s for penetration into concrete and geologic materials. For example, the experimental results reported by Forrestal, Frew, Hanchak, and Brar in Ref. 13 indicate projectile-mass loss of about one percent at an impact velocity of 350 m/s, up to about six percent at a velocity of 1050 m/s for impacts into grout targets. Similar results were obtained for impacts into concrete. The mass loss increased monotonically with striking velocity, and examination of the recovered projectiles showed that almost all of the erosion was in the nose region. Moreover, the directional instability associated with the projectile trajectory in the target increased with velocity, presumably due to increasing nose erosion. At velocities above 1200 m/s, the projectiles exited the side of the target, bent severely, or broke.

It is noteworthy that the projectiles for this particular data set were 4340 steel rods with a compressive strength of approximately 1.2 GPa (180 ksi) while the grout targets had a compressive strength of only 13.8 MPa (2 ksi).

That is, the mass losses occurred on high-strength projectiles for penetration into relatively low-strength targets.

The penetration model presented in this dissertation predicts that the penetrator will not begin to flow until the impact velocity reaches approximately 1600 m/s for these materials, suggesting that the stress on the nose due to the target structural resistance and hydrodynamic pressure remains below the level required to cause the penetrator to transition to plastic flow, which is approximately three times the compressive strength of the penetrator material. In addition, examination of the surfaces of the post-test projectiles indicates local surface erosion as opposed to global plastic flow.

This nose erosion at impact velocities well below the predicted velocity for penetrator flow initiation is not observed in ductile metals. However, this erosion has been observed on high-strength projectiles at relatively low-impact velocities for penetration into relatively strong granite and relatively weak limestone targets in addition to various strength concrete targets. These results indicate that the presence or absence of local surface erosion may not be a strong function of the strength or density of the material but may be dependent upon the ductility or granularity of the target.

In support of this hypothesis, tests conducted at Louisiana Tech University have shown no discernible erosion on 1.93 GPa (280 ksi) steel projectiles impacting 0.52 GPa (75 ksi) stainless steel targets while impacts of the same type projectiles at the same impact velocity (790 m/s) into 15 MPa (2.2 ksi) concrete caused measurable nose erosion.

Analysis of Potential Projectile Erosion Mechanisms

One potential governing mechanism studied is spallation due to thermal stresses in the penetrator material. Solution of the unsteady heat conduction equation with the conservative assumption that the penetrator surface temperature is raised to the melting temperature, shows that the temperature at a depth of 0.01 mm increases less than 200 K in 200 μs, which is a typical time for the impact event. Therefore, thermal effects are negligible during the actual penetration process due to insufficient time for significant heat transfer. The conclusion is that it is unlikely that the projectile erosion is due to thermal effects.

Another potential governing mechanism investigated is global plastic flow due to the target structural resistance and hydrodynamic pressure. For all of the test conditions reported in Ref. 13, it was predicted that the stresses on the nosetips were well below those required to cause nosetip

material loss during the developed target erosion portion of the penetration process. This result contrasts with the experimental results that clearly show nosetip erosion on the recovered projectiles. The model accurately predicts the impact velocities for the onset of nosetip erosion for penetration of metal targets. The model is based solely on the conservation of momentum and mass equations and involves no empirical parameters, so that the inability to predict the observed erosion suggests that another mechanism is involved. It was concluded that the target structural and hydrodynamic stresses are unlikely to account for projectile erosion at the relatively low impact velocities of the tests in Ref. 13.

An additional potential mechanism considered is mechanical erosion due to a postulated unsteady, periodic impact process. This postulation characterizes the penetration process as a series of high-frequency impacts that alternately raise the interface pressure to impact values and decrease it to near zero as the target material is jetted away from the interface region. The application of such a postulated mechanism to target penetration showed no fundamental differences on penetrator erosion between concrete and metal targets. It is highly questionable that this mechanism actually exists and, if it does, it does not

explain the observed projectile nosetip erosion in concrete and geologic targets.

It was also considered that friction between the penetrator and target in the nosetip region might be a cause of the nosetip erosion. However, calculation of the friction force due to the resistance of the target indicates that this force is always well below the shear strength of the penetrator for the materials and test conditions of Ref. 13. The shear stress associated with the friction force is typically less than 10 percent of the sum of the structural and hydrodynamic stresses during the penetration process. It is concluded that it is unlikely that penetrator-target interface friction causes the observed projectile erosion.

The final potential mechanism studied is mechanical erosion due to the aggregate or grains in concrete or geologic target materials. This mechanism postulates that the target particles impact the penetrator nosetip at irregular intervals, causing a high pressure Hugoniot shock wave for each impact which exceeds the shear strength of the penetrator material and results in the removal of irregular chunks from the surface. This mechanism was the most probable cause of the projectile erosion. The analysis on which this conclusion is based is summarized in the next section.

Analysis of Mechanical Erosion Due to Target Granularity

From data in Ref. 13, it is observed that for a strong steel projectile (1275 MPa; 185 ksi), with an ogive nosetip penetrating into 13.8 MPa (2 ksi) grout, there is penetrator nosetip erosion at less than 400 m/s. The percent mass loss of the penetrator is presented in Fig. 18 for four different strengths of grout or concrete. If the data in Fig. 18 are extrapolated downward, the point at which penetrator nosetip erosion begins is approximately 200 m/s.

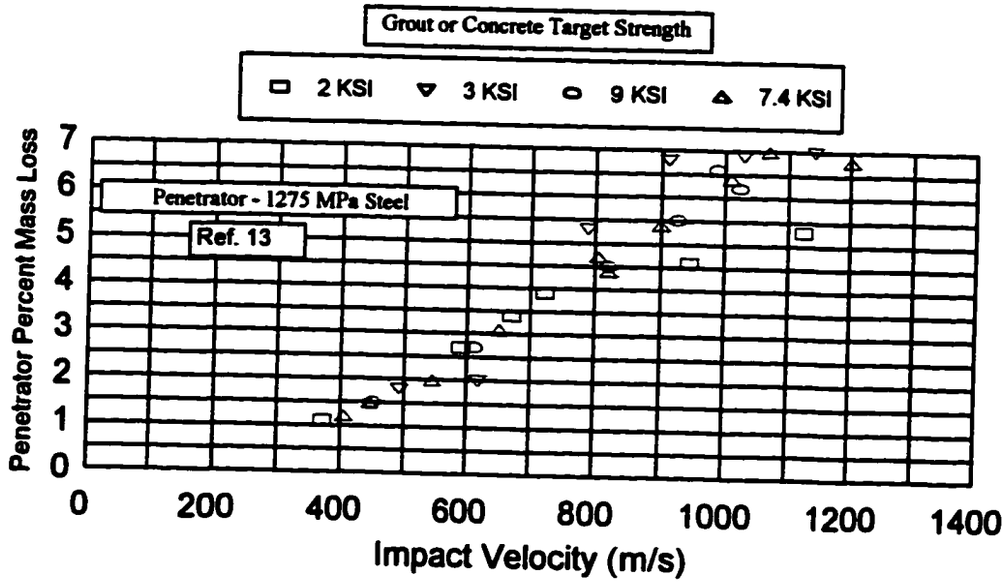

Fig. 18. Penetrator Percent Mass Loss vs. Impact Velocity For Various Strengths of Grout or Concrete Targets

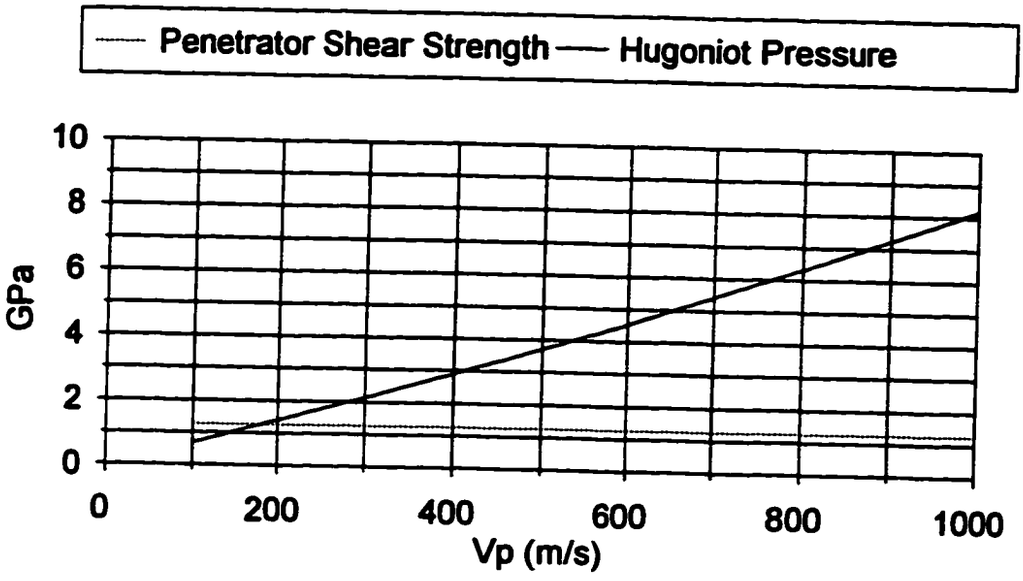

Fig. 19. Hugoniot Impact Stress vs. Impact Velocity for 1275 MPa (185 ksi) Steel into 62 MPa (9 ksi) Concrete

In Fig. 19, the Hugoniot pressure is plotted versus impact velocity for the materials in Fig. 18. The penetrator shear strength is also shown as a horizontal line on the graph. It is noted that the lines cross at 190 m/s which, notably, is approximately the same velocity at which erosion begins from the extrapolation of the experimental data in Fig. 18. Therefore, the particle Hugoniot impact pressure exceeds the penetrator shear strength at approximately the same impact velocity where the onset of penetrator erosion is observed. A metal target with the same strength and density as the concrete would not begin to erode the same penetrator until the impact velocity exceeds 1500 m/s. These observations strongly suggest that the

particle Hugoniot impact pressure may play a significant role in penetrator erosion for granular targets.

Based on these results, it is postulated that the nosetip erosion is caused by the same mechanism as the initial transient, the Hugoniot shock wave. In this proposed model, the penetrator continues to strike the non-homogenous aggregate or grains at certain intervals depending on the spacing and size of the particles. Every time the penetrator strikes another particle, a Hugoniot shock wave with its accompanying high stress is generated. The pressure then decreases with time in the penetrator in the same manner as for the initial transient.

Modeling this effect begins by calculating the particle velocity for a Hugoniot shock wave equal to the shear strength of the penetrator. The shear strength of the penetrator is used because, as the particle strikes the penetrator, material is sheared from the surface. In equation form, this term is

$$\rho_p U_{phss} V_{sp} = \sigma_{ssp} \qquad (98)$$

where

U_{phss} = particle velocity for a Hugoniot shock wave equal to the shear strength of the penetrator.

σ_{ssp} = shear strength of the penetrator.

The strength of the Hugoniot shock wave striking a particle depends upon the current velocity of the

penetrator. The particle velocity associated with this shock wave is calculated as in the case of the initial transient except that the current velocity is used. The Hugoniot particle velocity due to the aggregate impact is U_{phag}. This particle velocity must exceed the particle velocity for a Hugoniot shock wave equal to the shear strength of the penetrator, U_{phss}, in order for the penetrator to be eroded by an impact with the aggregate. This means that the stress associated with the Hugoniot shock wave produced by an impact with the aggregate must be higher than the shear strength of the penetrator in order for the penetrator to lose mass. Assuming that the particles are spaced sufficiently close together, the pressure on the front of the penetrator will be continually increasing and decreasing due to the periodic impacting of the aggregate and grains of the concrete. After impact with a particle, the pressure decreases and, in the absence of subsequent impacts, falls below the shear strength, whereupon penetrator mass loss stops. Over a wave cycle, the pressure would not remain at the Hugoniot pressure so an equation for mass loss must account for this. The amount of penetrator length lost per wave cycle is

$$(U_{phag} - U_{phss}) \frac{\sin\theta \, \Delta t^{i}}{P_f} \qquad (99)$$

where

P_f = spacing/transient effects factor for the aggregate or grains in the concrete.

Δt^i = time for each wave cycle.

The spacing/transient factor, P_f, reduces the full Hugoniot pressure to account for the spacing between impacting particles and the transient nature of the impacts. A typical value for P_f is 6 which must be determined from experimental data for each material. Once the P_f is found for that material, it can be used to predict all other data points for that material set.

The time for each wave cycle is an important parameter because longer penetrators have lower decelerations due to increased wave cycle time. This means that the time during which the penetrator nosetip is eroded is also greater. For example, doubling the penetrator length with the same diameter will cause the nosetip to erode for twice as long which, in turn, results in a larger penetrator mass loss.

Eqn. (99) is added to the penetrator length equation, Eqn. (46), as long as U_{phag} is greater than U_{phss}. The term is equal to zero if U_{phag} is less than U_{phss}. The term is also assumed to be zero when the penetrator begins to flow because the penetrator near the interface is already in the plastic state and flowing away from the interface.

The effect of this term is that the nosetip blunts, resulting in increased target resistance, and, consequently, the rate of crater depth formation decreases. This result is expected because, if the nosetip is not deformed, the predicted penetration depth is much greater than the experimental as shown in Fig. 20. When the nosetip is eroded by using Eqn. (99) with $P_f = 7$, the penetration depth reduces to approximately the correct depth as is observed in Fig. 20. The calculation using the configuration of the recovered penetrator assuming no further deformation is also shown. It is noted that the data falls between the ogive with no erosion term and the recovered penetrator configuration with no erosion term. This suggests that the nosetip blunting effect causes the reduction in penetration depth.

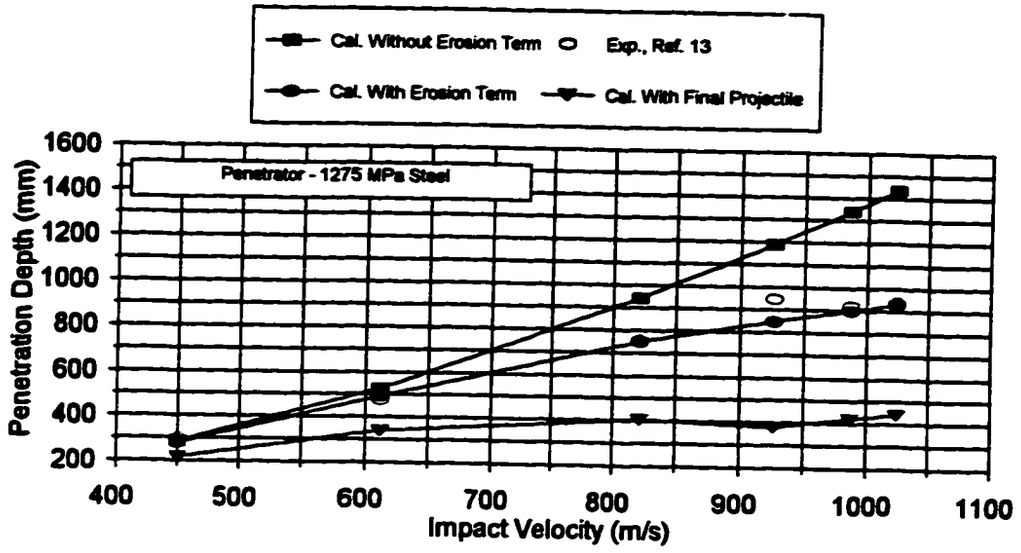

Fig. 20. Penetration Depth vs Impact Velocity for 62 MPa (9 ksi) Concrete With and Without the Aggregate Erosion Term

Fig. 21a shows penetration depth in a 62 MPa(9 ksi) concrete target after impact by a 1,275 MPa(185 ksi) steel penetrator with a 3 CRH ogive nosetip. The calculated value includes the aggregate erosion term which blunts the sharp ogive nosetip penetrator and thereby reduces the penetration depth. The model predicts the penetration depth for the entire range within the experimental uncertainty.

Fig. 21b presents residual penetrator length for these same tests. Without the aggregate erosion term, the model predicts that no nosetip erosion occurs. But with the aggregate erosion term, the residual penetrator lengths match the data for the entire velocity range.

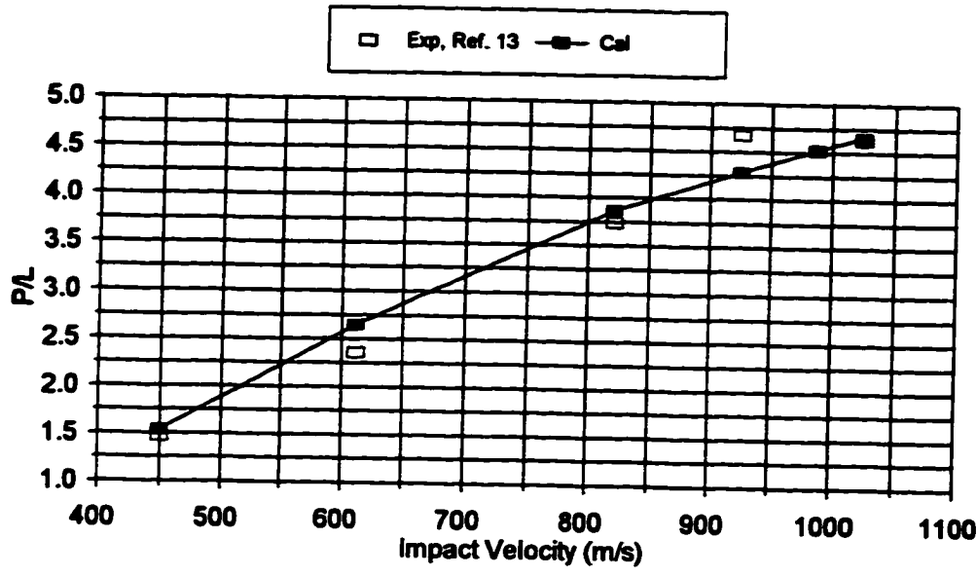

a. Crater Depth vs. Impact Velocity

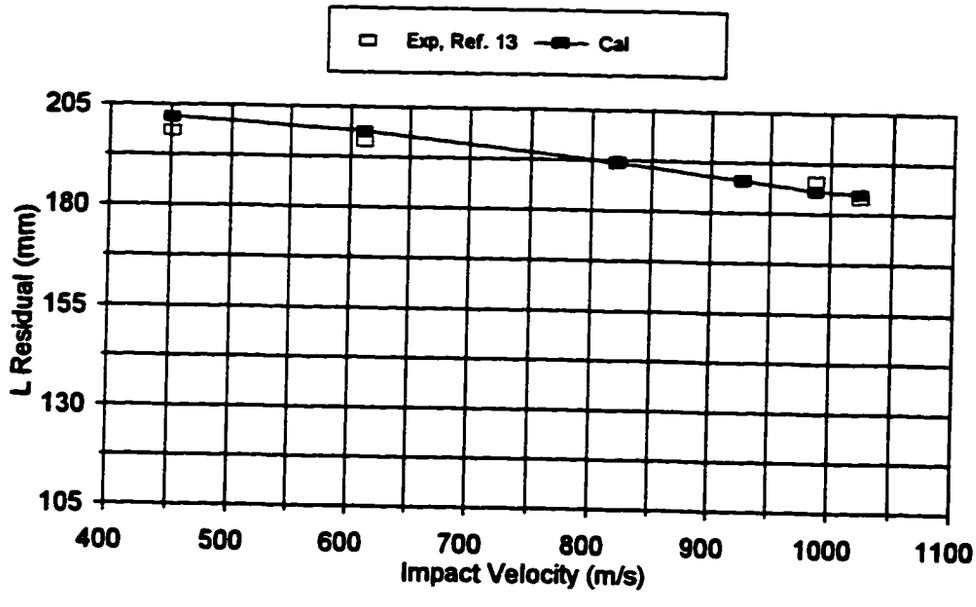

b. Residual Penetrator Length vs. Impact Velocity

Fig. 21. 3 CRH Ogive Nosetip Steel 1275 MPa (185 ksi) Penetrator into 62 MPa (9 ksi) Concrete, L/D = 10

Fig. 22a presents crater depth versus impact velocity for 1275 MPa (185 ksi), 3 CRH ogive nosetip steel penetrator into 51 MPa (7.4 ksi) concrete. The prediction model includes the aggregate erosion term and predicts well over the entire velocity range.

Fig. 22b shows the residual penetrator lengths for these same tests. The aggregate erosion model is about 1 to 3% high over the entire velocity range, which is within the experimental uncertainty of the data.

These results show that the projectile erosion and decreased penetration depths observed for impact into concrete can be accurately predicted with a model based on the elevated Hugoniot shock pressures that accompany encounter with the particles in the concrete. The emergence of this mechanism as the most probable also suggests that target granularity may be the most influential target property in the erosion process.

Ceramic Targets

Ceramic targets have been studied for their ballistic protection over low- to medium-impact velocities, but it has been noted that at hypervelocities, such as shape charge velocities, ceramics are less effective than metals. With these two effects known, a combination of target materials such as ceramics and metals in layers are an

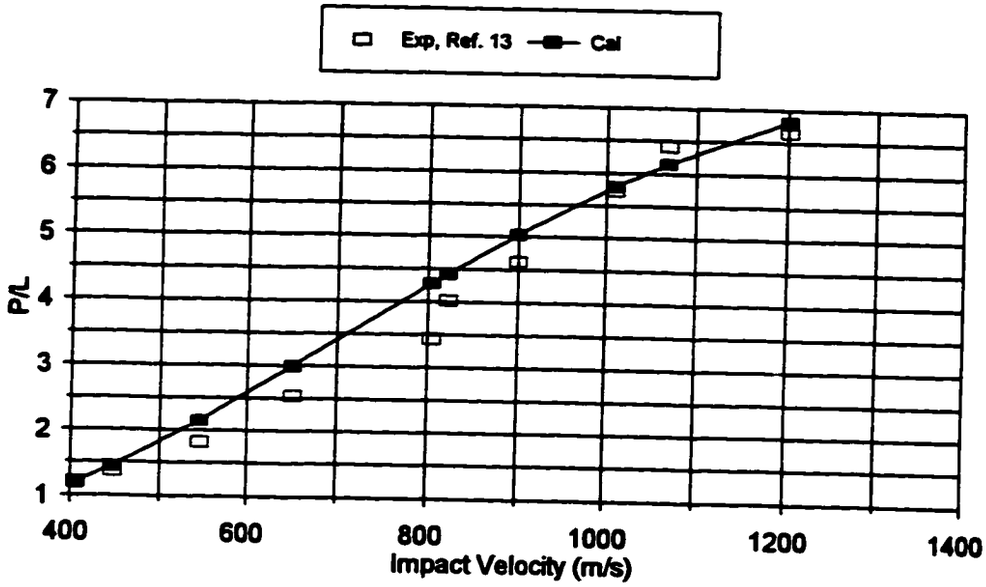

a. Crater Depth vs. Impact Velocity

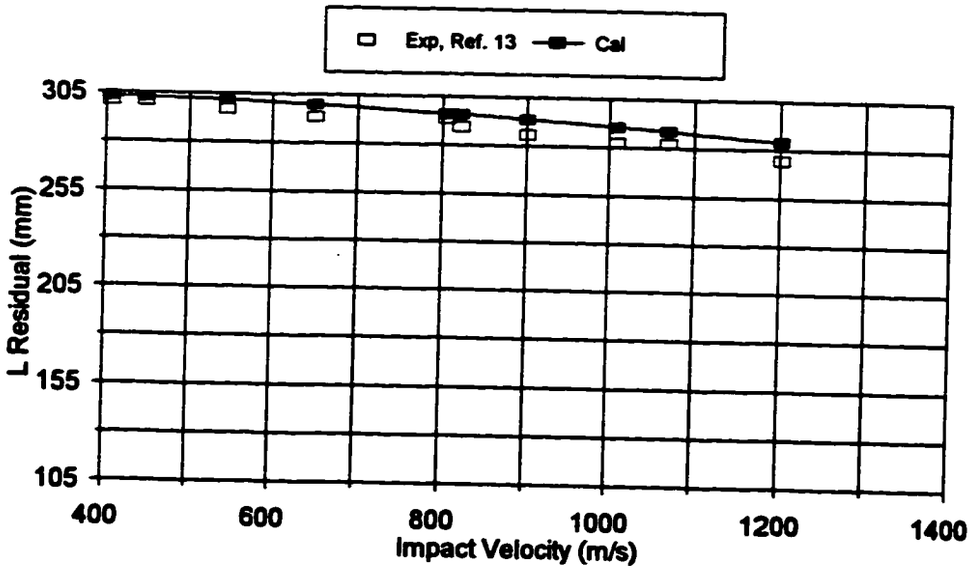

b. Residual Penetrator Length vs. Impact Velocity

Fig. 22. 3 CRH Ogive Nosetip Steel 1275 MPa (185 ksi) Penetrator into 51 MPa (7.4 ksi) Concrete, L/D = 10

effective solution. It is noted that in Eqn. (42), the rate of penetration increases at impact velocities above that at which the target begins to flow. The impact velocity for target flow initialization for boron carbide ceramic with a density of 2510 kg/m^3 and a compressive strength of 2.8 GPa impacted by a tungsten penetrator with a strength of 1.5 GPa is approximately 1000 m/s. For a steel target with a compressive strength of 1.5 GPa, the upper limit on steels, impacted by the same tungsten penetrator, the target flow initialization velocity is 1250 m/s. This means that both ceramic and steel targets will have low penetration depths until the flow initiation velocities are reached but the boron carbide has less than one-third the density of steel. This results in significant weight savings. The target flow initialization velocity is found by combining Eqns. (77)and (78).

$$V_{ptfi} = U_{ppm} + U_{ptm} + \sqrt{\frac{S_t' - S_p'}{\rho_p'}} \qquad (100)$$

It is observed that a decrease in target density and increase in target compressive strength causes the maximum target particle velocity to increase.

$$P_t' = S_t' = \rho_t U_{ptm} V_{st} = \frac{\sigma_{st}}{\nu_t^{1+\sin\theta}} \qquad (51)$$

The increase in target strength also increases the maximum confined strength from Eqn. (51). This increase in both the maximum target particle velocity and target maximum confined strength are responsible for the increase in the target flow initialization impact velocity as observed in Eqn. (100). This indicates that to a low-penetration depth at lower velocities, a low-density, high-strength target material like a ceramic is equivalent or superior to a high-density, high-strength target material like steel or tungsten.

The higher penetration depth at higher velocities, (shape-charge velocities) is explained by the density effect. At high velocities the ratio of penetration depth to the initial penetrator length, P/L, is given by the hydrodynamic flow equation (Ref. 2).

$$\frac{P}{L} = \sqrt{\frac{\rho_p}{\rho_t}} \qquad (101)$$

This equation is valid only for long penetrators and very high velocities. The P/L calculated with this equation for the 2510 kg/m^3 ceramic target and the tungsten penetrator is 2.75. The P/L for the steel target and the tungsten penetrator is 1.55. Thus, the penetration is 77% greater for a ceramic target than for a steel target. The P/L for a tungsten target and a tungsten penetrator is 1.00 while the P/L is 2.75 for the ceramic target which is a 175% difference.

It is seen from the above examples that ceramics offer better protection for targets over low- to medium-impact velocities but do not compare favorably at hypervelocities as demonstrated in Fig. 23 which presents a comparison of a 1.5 GPa tungsten penetrator into boron carbide, 1.5 GPa steel, and 1.5 GPa tungsten targets. The ceramic is equally resistant to penetration compared with the metals up to an impact velocity of approximately 1000 m/s. Above this velocity, the penetration depth curves diverge and the metals become more resistant to penetration. However, the significantly lower density of the ceramic offers a substantial weight reduction for impact velocities up to 5 km/s. This indicates that a layered target with both ceramics and high density metals would offer protection over a wide range of velocities. The ceramic would be more effective against low- to medium-velocity projectiles while the high density metal would be more effective at hypervelocity. Additional study is required in order to optimize the weight of the armor and the protection needed.

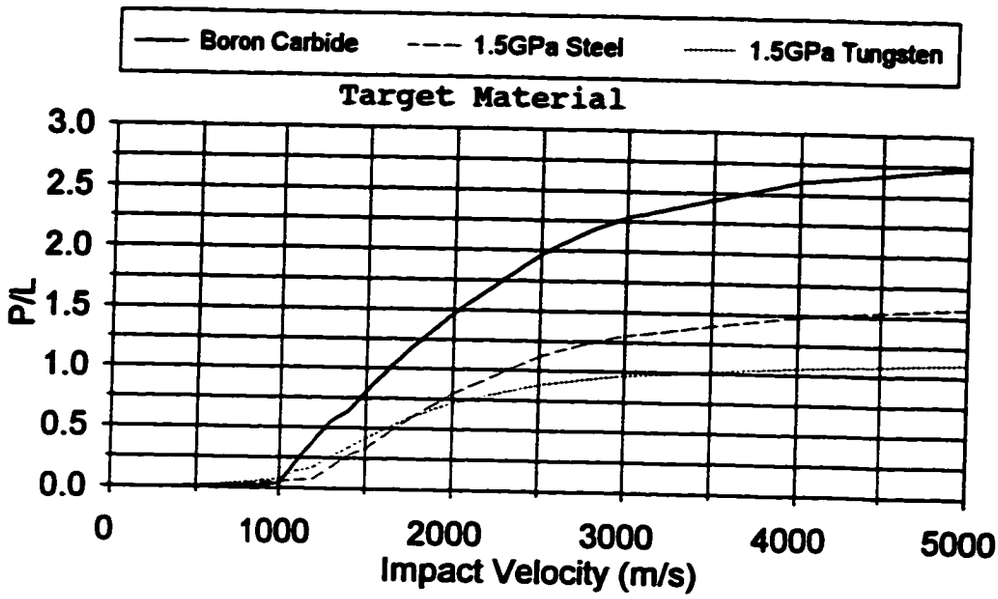

a. Normalized Penetration Depth vs. Impact Velocity

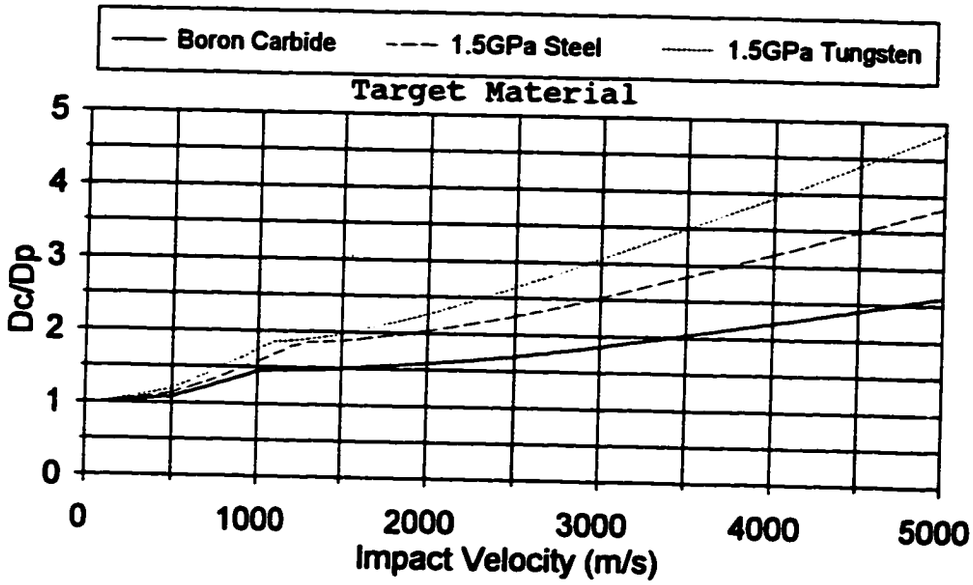

b. Normalized Crater Diameter vs. Impact Velocity

Fig. 23. Effect of a 1500 MPa Tungsten Penetrator into Boron Carbide, 1.5 GPa Steel, and 1.5 GPa Tungsten, (Blunt Nosetip, L/D = 20)

CHAPTER 9

RESULTS

The theoretical analysis presented here was programmed into a computer spreadsheet to compare the predicted crater depths, crater diameters, residual penetrator lengths, and residual penetrator velocities with experimental data. The experimental data were obtained from several references along with experiments conducted in the ballistics range at Louisiana Tech University. A parametric study of the effect of the nosetip angle on penetration depth for various penetrator and target properties is included.

Tabular data are provided for the experiments conducted at Louisiana Tech University. Graphs are provided for the data taken from the references. The graphical output presents penetration depth normalized by initial length of the penetrator, crater diameter normalized by the penetrator diameter, residual penetrator length, or residual penetrator velocity all versus impact velocity.

Table 4 lists the required input parameters for the analytical model. Typical values are given for a tungsten alloy penetrator and a 4340 steel target. Table 5 displays the typical output parameters for the analytical model.

These are the variables of primary importance. Other variables can be deduced if necessary.

Table 4. Required Input Parameters for Analytical Model

PARAMETER	UNITS	TYPICAL VALUES*	
		PENETRATOR	TARGET
DENSITY	Kg/m^3	17120	7900
ULTIMATE COMPRESSIVE STRENGTH	MPa	1200	800
POISSON'S RATIO		.285	.285
LONGITUDINAL SOUND VELOCITY	m/s	4029	3574
TANGENTIAL SOUND VELOCITY	m/s	2890	2800
HUGONIOT CONSTANT		1.237	1.92
NOSETIP AVERAGE ANGLE	deg	17.7	
INITIAL PENETRATOR LENGTH	m	.018	
PENETRATOR DIAMETER	m	.006	
INITIAL IMPACT VELOCITY	m/s	1000	

* Penetrator is tungsten alloy and target is 4340 steel.

TABLE 5. Typical Output Parameters for Analytical Model

PARAMETER	SYMBOL
TIME FROM IMPACT, μs	t
PENETRATOR VELOCITY AS FUNCTION OF TIME, m/s	V_p
RATIO OF PENETRATOR LENGTH TO INITIAL PENETRATOR LENGTH AS FUNCTION OF TIME	L_p/L_{pI}
RATIO OF CRATER DEPTH TO INITIAL PENETRATOR LENGTH WITHOUT THE FINAL TRANSIENT AS FUNCTION OF TIME	L_c/L_{pI}
RATIO OF CRATER DIAMETER TO INITIAL PENETRATOR DIAMETER AS FUNCTION OF CRATER DEPTH	D_c/D_p
RATIO FINAL CRATER DEPTH TO INITIAL PENETRATOR LENGTH AS FUNCTION OF TIME	L_{cm}/L_{pI}

Louisiana Tech University Experiments

Table 6 presents the results of three shots conducted at Louisiana Tech using armor-piercing steel cores cut from a metal-jacketed 30-06 round. The properties were obtained from a hardness test (R_c = 55). The cores were turned in a lathe to reduce the diameter to 5.715 mm to fit into the 30-06 accelerator sabot. Because the cores were too hard for a lathe tool, a grinder mounted on the lathe was used. The lathe-grinder was also used to machine conical nosetips on the cores. The gun was a 30-06 rifle mounted in a holder and firing into a 12 mm thick, steel-walled ballistic range. A digital chronograph was used to obtain the velocity of the penetrators by measuring the time for the projectile to break two light beams 12 inches apart. Three of a total of six shots are reported here. The three shots not reported either tumbled on launch or broke into pieces upon impact. The three reported shots had conical nosetips that were 32, 67, and 90 degrees.

The 90 degree conical nosetip is a blunt or flat faced penetrator. None of the penetrators showed any sign of deformation, but they were broken into two or three pieces. The penetrator material is so brittle that the release waves will cause failure. The calculated crater depths are within the experimental error for the 32 and 67 degree nosetips,

Table 6. Armor Piercing Steel into 6061-T651 Aluminum

a. Target and Projectile Characteristics

Component	Material	Density (kg/m^3)	σ (MPa)
Target	6061-T651 Aluminum	2700	310
Projectile	Tool Steel	7900	1800

b. Experimental and Calculated Crater Depth

Impact Velocity (m/s)#	Nosetip Type#	Proj. Len.* (mm)#	Exp. Crater Depth (mm)#	Cal. Crater Depth (mm)	Percent Diff.
1024	32° Cone	23.72	44.5	45.5	2.2%
1139	67° Cone	20.75	33	32.4	-1.9%
1327	90° Blunt	19.58	30	34	13.5%

* Projectile Diameters are all 5.715 mm

Uncertainties are ± .5 degrees for the nosetip angle, ± 6 m/s for impact velocity, ± 0.012 mm for projectile length and diameter, ± 0.5 mm for crater depth

but the 90-degree conical nosetip predicts a value 13.5% too high.

Table 7 gives the results for the same 6061-T651 aluminum target but with a softer steel penetrator. The penetrator was ground down from a Grade 11.5 0.5-inch steel bolt which had a compressive strength of 1200 MPa. The performance of these penetrators show extreme sensitivity to angles of yaw at impact. If the penetrator had significant yaw upon impact, the side of the nosetip that impacts first

experiences a larger side force which results in a larger yawing moment, causing the penetrator to tumble in the target. The calculated depths for the two low-yaw tests are approximately 6% and 12% too deep as compared to the experiments.

Table 7. Grade 11.5 0.5-Inch Steel Bolt into 6061-T651 Aluminum

a. Target and Projectile Characteristics

Component	Material	Density (kg/m^3)	σ (MPa)
Target	6061-T651 Aluminum	2700	310
Projectile	Grade 11.5 Steel Bolt	7900	1207

b. Experimental and Calculated Crater Depths

Impact Velocity (m/s)#	Nosetip Type#	Proj. Len.*# (mm)	Exp. Crater Depth# (mm)	Cal. Crater Depth (mm)	Percent Diff.
1072	20 Cone	11.7	25.5	28.7	12.5%
1100	20 Cone	16.21	39.0	41.5	6.4%

* Projectile Diameters are all 5.715 mm

Uncertainties are ± .5 degrees for the nosetip angle, ± 6 m/s for impact velocity, ± 0.012 mm for projectile length and diameter, ± 0.5 mm for crater depth

Table 8 shows the data obtained by firing full metal jacket rounds made of lead into the same type 6061-T651 aluminum targets. It is predicted that the soft lead begins to flow immediately upon impact. It is noted that the non-flowing 20-degree conical nosetip in Table 7 penetrates much deeper into the target than the flowing 20 degree conical nosetip in Table 8. The two penetrator materials are different so an exact comparison cannot be made, but it is noted that the penetration depth is 12 mm for the flowing penetrator and 39 mm for the non-flowing penetrator.

Metal Penetrators into Metal Targets

Figs. 24a and 24b compare the calculated and experimental results for penetration depth and crater diameter, respectively, as a function of impact velocity, V_p, for tungsten penetrators into two steel targets of different strengths. In Fig. 24a the penetration depth, P, is normalized by dividing by the original length of the penetrator, L, and, in Fig. 24b, the crater diameter is normalized by dividing by the diameter of the penetrator D_p. The penetrators had an average L/D ratio of 23 with hemispherical nosetips. The nosetips should have been quickly blunted at these impact velocities since the calculations predict that the penetrators were flowing at

Table 8. Full Metal Jacket Lead into 6061-T651 Aluminum

a. Target and Projectile Characteristics

Component	Material	Density (kg/m^3)	σ (MPa)
Target	6061-T651 Aluminum	2700	310
Projectile	FMJ Lead	11500	50

b. Experimental and Calculated Crater Depths

Impact Velocity (m/s)	Nosetip Type#	Proj. Len. (mm)#	Exp. Crater Depth (mm)#	Cal. Crater Depth (mm)	Percent Diff.
1132.2	20 Cone	16.21	12	14.6	21.7%
1132.3	20 Cone	16.21	12	14.6	21.7%

* Projectile Diameters are all 5.715 mm

Uncertainties are ± .5 degrees for the nosetip angle, ± 6 m/s for impact velocity, ± 0.012 mm for projectile length and diameter, ± 0.5 mm for crater depth

the lowest impact velocities reported. The higher strength steel target offered better protection than the lower strength target at velocities below approximately 2800 m/s. Above that impact velocity, the target strength did not make a significant difference in normalized penetration depth.

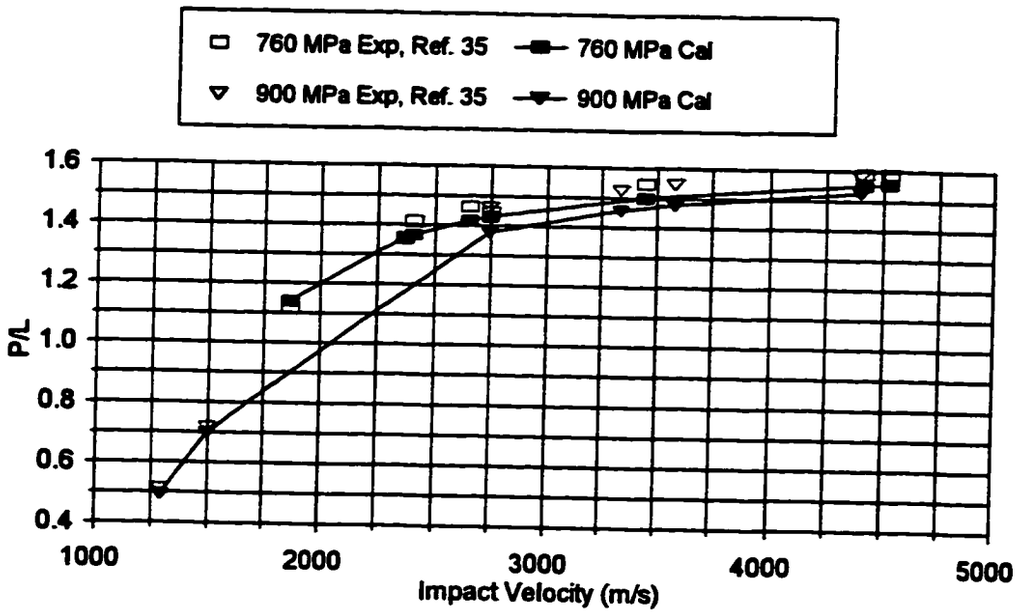

a. Crater Depth vs. Impact Velocity

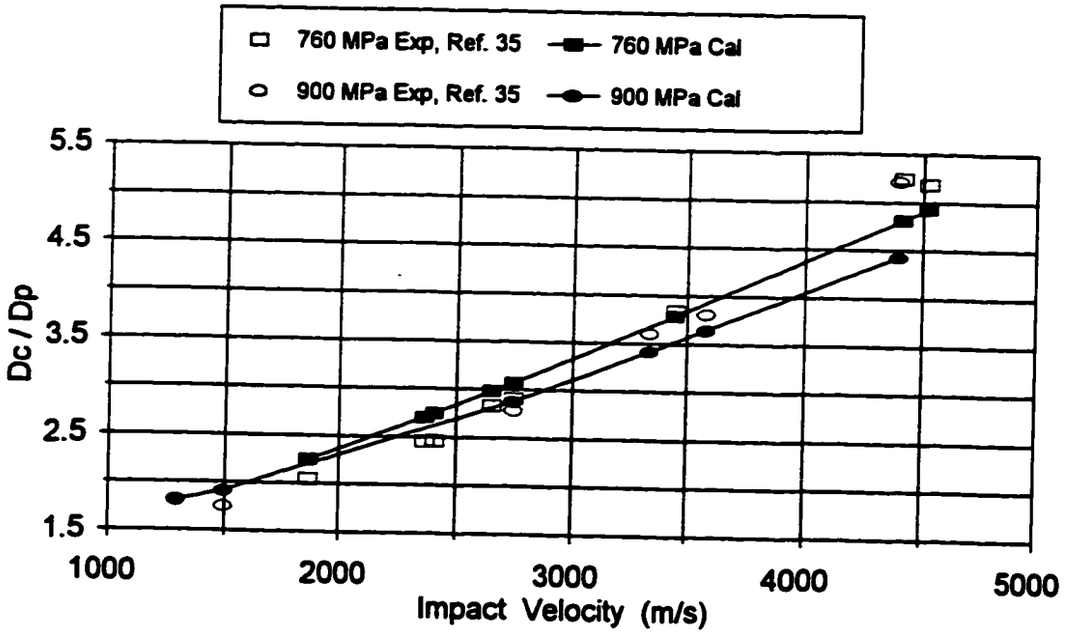

b. Crater Diameter vs. Impact Velocity

Fig. 24. W10 Tungsten Hemispherical Nosetip Penetrator into 760 MPa and 900 MPa RHA, L/D = 23

At the higher velocities, the hydrodynamic terms in the momentum interface equation are much larger than the constant structural strength terms and the penetrator/target interaction is considered to be hydrodynamic in nature. The theoretical value of P/L is the square root of the ratio of penetrator density to target density, Eqn. (101), which is approximately 1.5 in this case. The experimental and calculated values of P/L in Fig. 23a are approaching 1.6 and the calculations show that the P/L continues to increase with increasing impact velocity. It is found from the model developed in this study that the added penetration depth beyond the theoretical limit is due principally to the terminal transient with some small contribution from the initial transient. The calculated crater depths and crater diameters are nominally within 3% of the experiment results.

Figs. 25, 26, and 27 compare the penetration capabilities of uranium alloy and tungsten alloy penetrators. Fig. 25 shows a 93W tungsten alloy impacting rolled homogeneous armor (RHA) which is 4340 steel and Fig. 26 shows U-3/4 Ti uranium alloy impacting RHA. Fig. 27 combines the data to show the differences between the two data sets. The penetrator strengths were approximately the

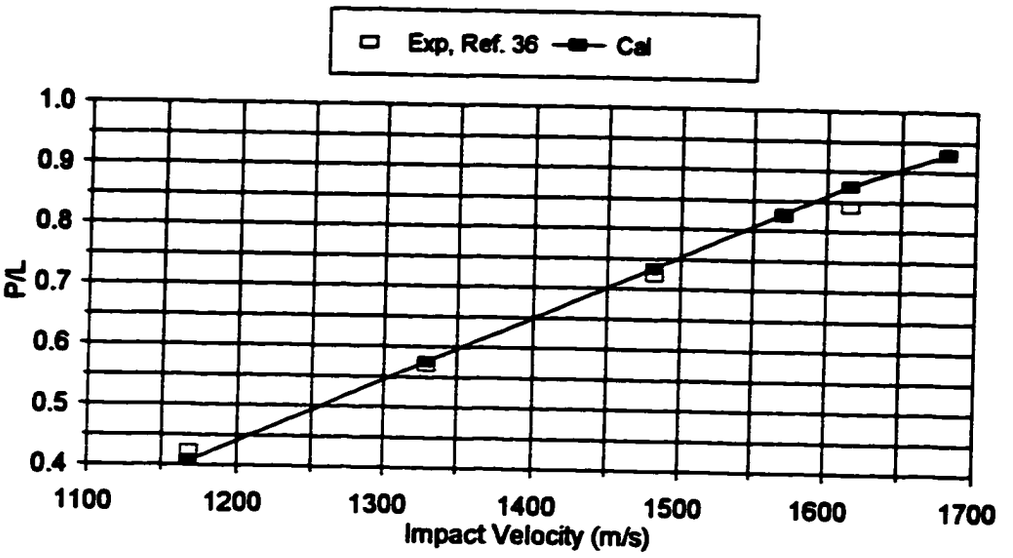

Fig. 25. Crater Depth vs. Impact Velocity for 93W Hemispherical Nosetip Penetrator into RHA, L/D = 20

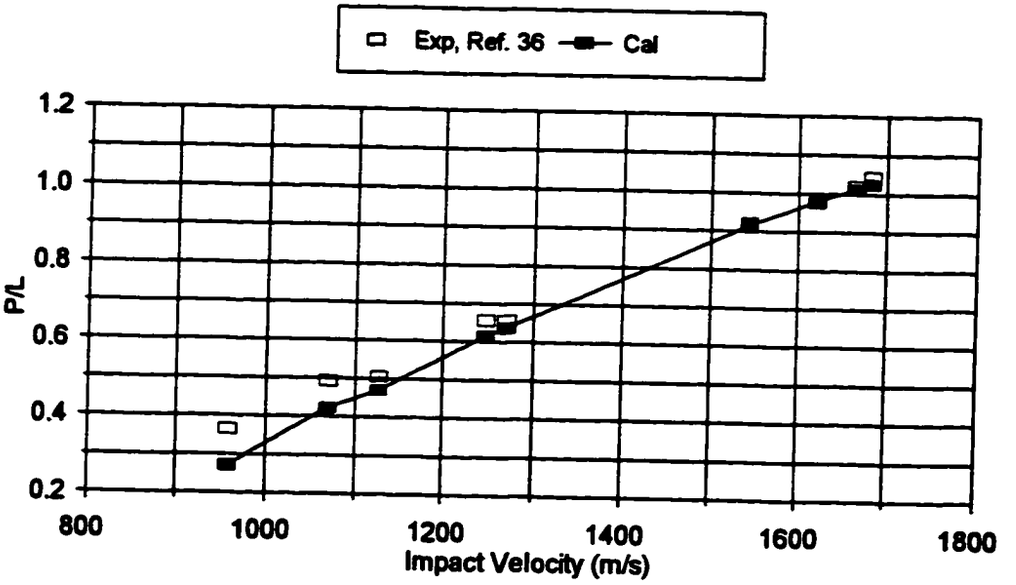

Fig. 26. Crater Depth vs. Impact Velocity for U-3/4 Ti Hemispherical Nosetip Penetrator into RHA, L/D = 20

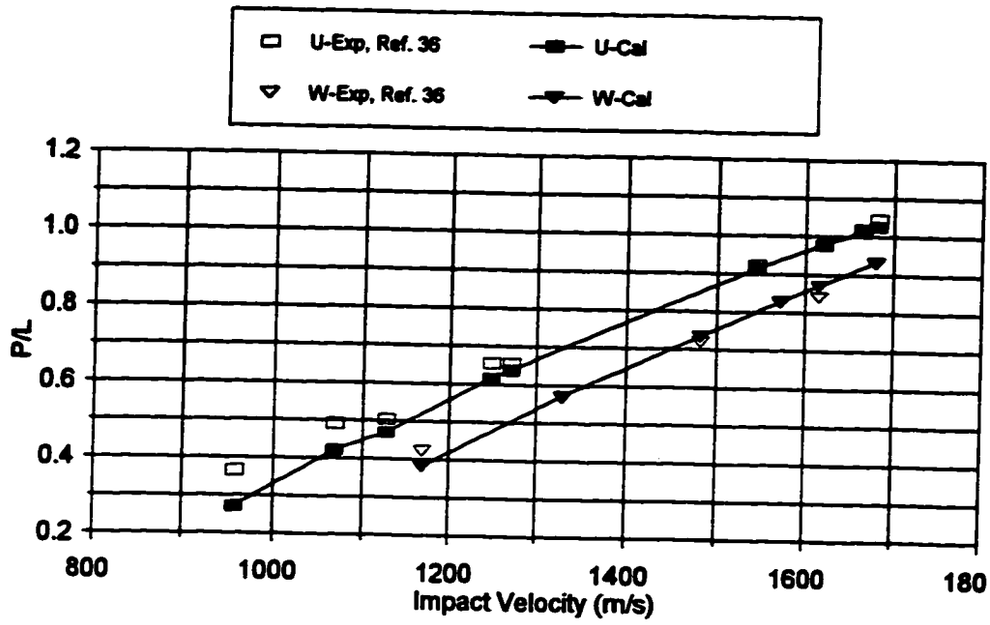

Fig. 27. Comparison of Depth vs. Impact Velocity for U-3/4 Ti and 93W Tungsten Penetrators into RHA, L/D = 20

same. The uranium alloy penetrates to a greater depth than the tungsten alloy over the entire velocity range with values of P/L approximately 35% greater at 1200 m/s decreasing to approximately 10% at 1700 m/s. This appears to indicate that there is a gain in using uranium projectiles over tungsten projectiles. From the physics based model used in this study, it is found that the difference in penetration capability is due to uranium's low Poisson's ratio compared to tungsten. The calculated depths are nominally within 2% of the experimental results except at the lower impact velocities for the uranium penetrator.

Fig. 28 demonstrates the gain obtained by using an ogive nosetip over a hemispherical nosetip for the same penetrator and target materials. The penetrators were non-deforming over the 400 to 1400 m/s velocity range. There is only a small gain in penetration depth up to 800 m/s, but above 800 m/s there is an increasing gain up to approximately 30% at 1200 m/s. The calculated depths are nominally within 5% of the experimental values.

Fig. 29 shows the L/D effect of a non-deforming penetrator for three L/D's of 5.5, 10.5, and 14.5 for T-200 steel into 6061-T651 aluminum. The results show no significant differences between the normalized penetration for L/D of 10.5 and 14.5. The L/D of 5.5 indicates slightly higher penetration depths. The theoretical model indicates that this difference is due to the initial transient. This increased normalized penetration for lower L/D is greater for blunt penetrators due to the average nosetip angle, θ, in Eqn. (86) being at its maximum. The calculated depths match the experiment within the experimental uncertainty except at the highest velocities.

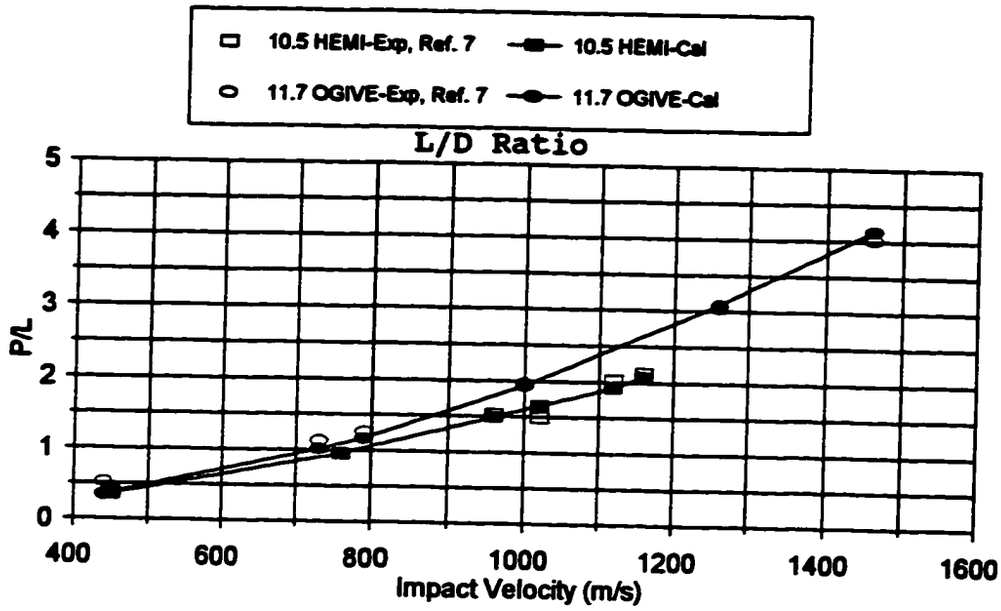

Fig. 28. Crater Depth vs. Impact Velocity for C-300 Steel Hemispherical Nosetip and Ogive Penetrators into 6061-T651 Aluminum, L/D = 10.5 and 11.68

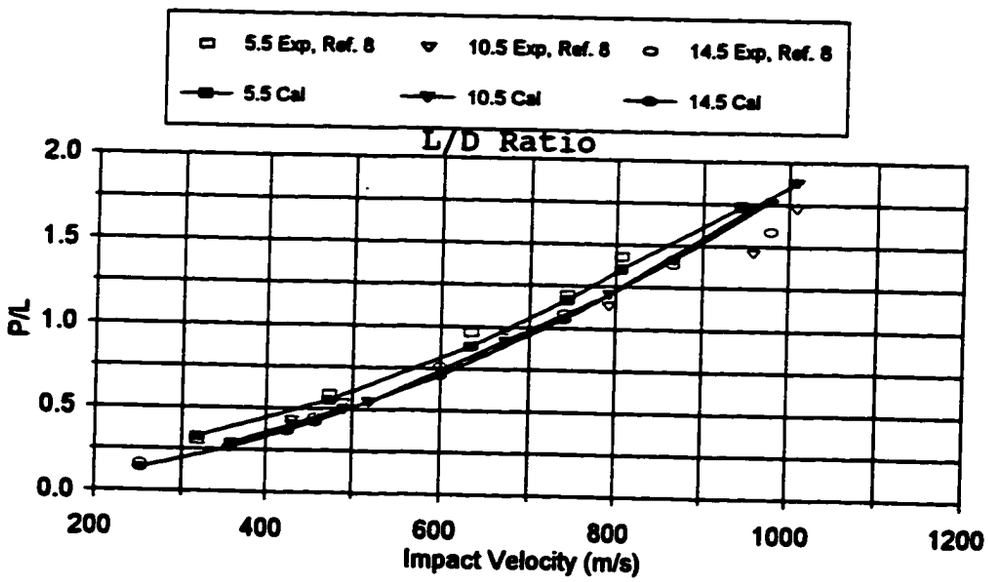

Fig. 29. Crater Depth vs. Impact Velocity for T-200 Steel Hemispherical Nosetip Penetrator into 6061-T651 Aluminum, L/D = 5.5, 10.5, and 14.5

Figs. 30a and 30b show the difference in penetration for L/D = 10 and 15 penetrators for tungsten into 4340 steel (RHA). The crater depth has some experimental scatter, and the calculated data matches the experiment within the experimental scatter. The crater diameter calculations are within the data scatter except at the upper velocity range where it is 5% high. There is only one crater diameter line for both L/D's since by Eqn. (82) the crater diameter depends only upon the penetrator diameter.

Fig. 31 illustrates the L/D effect for L/D's of 3, 6, and 12 for tungsten penetrators into steel targets. The L/D effect is very pronounced over the entire velocity range. There is considerable scatter in the experimental data, and the calculated penetration depth is nominally within the experimental uncertainty. There is significant difference between the L/D = 3 data and the L/D = 12 data. It is this difference that is a possible explanation for the segmented penetrator effect. As an example, the comparison of one segment with a length of 1.2 m and four segments with individual lengths of 0.3 m for a diameter of 0.1 m at 1500 m/s gives a penetration depth of 0.96 m for the single segment and 1.38 m for the total of the four segments. This

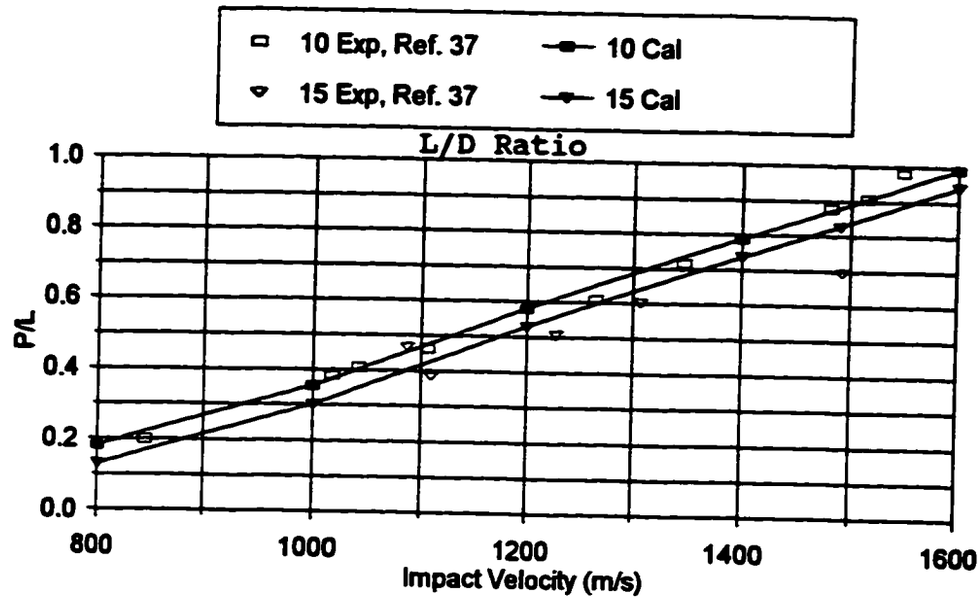

a. Crater Depth vs. Impact Velocity

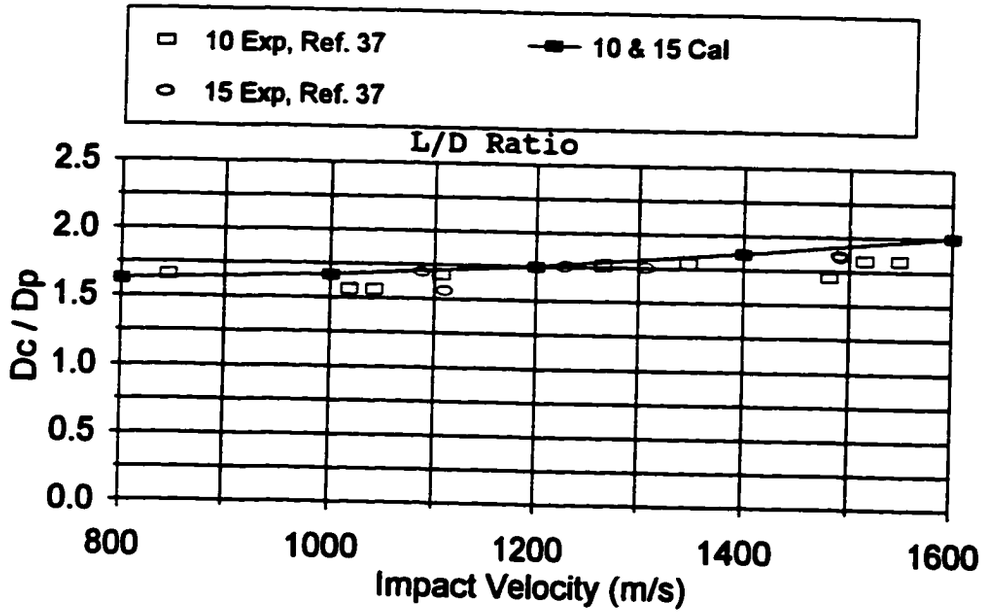

b. Crater Diameter vs. Impact Velocity

Fig. 30. X-27 Tungsten Hemispherical Nosetip Penetrator into 4340 Steel(RHA), L/D = 10 and 15

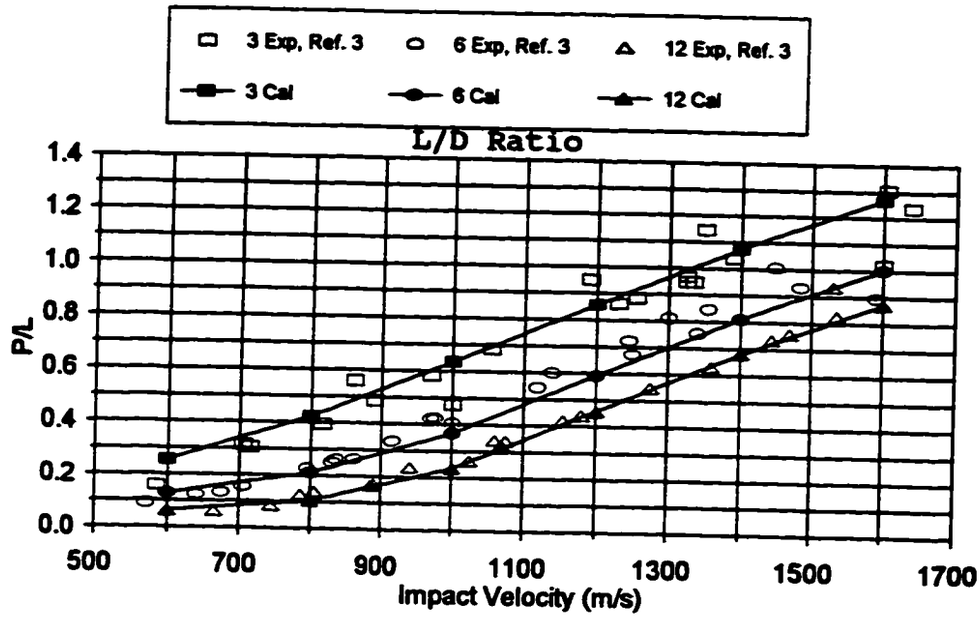

Fig. 31. Crater Depth vs. Impact Velocity for Tungsten Alloy Blunt Nosetip Penetrator into STA 61 Steel, L/D = 3, 6, and 12

shows a 44% increase and leads to the conclusion that four shorter segments would be better than one long segment if there is no interaction between the segments. The physical explanation for the increased penetration of the segmented rod as determined from the theoretical model is that each segment has a terminal transient, so that the four segments have four terminal transients compared to only one for the single segment penetrator. This also suggests that the spacing between segments will have an influence on the magnitude of the segmented penetrator advantage as increased spacing provides more time for the expansion of the terminal

transient from one segment before the impact of the next segment.

Figs. 32a and 32b show L/D = 20, uranium alloy penetrators impacting RHA. The calculated crater depths are within the experimental uncertainty over the velocity range. The calculated crater diameters also agree within the experimental uncertainty except at the higher velocities where the predictions are about 10% high.

Fig. 33 shows the same type penetrator with an L/D = 10 into St37 and St52 steels, with strengths of 450 MPa and 600 MPa, respectively. The crater depth predictions are within the experimental uncertainty except for the high velocity range where they are approximately 10% high.

In Fig. 34, 1100-0 aluminum is the material for both the penetrator and target. The penetrator has an L/D = 3. The model predicts the experimental results within the data uncertainty below 2000 m/s. Above 2000 m/s the model predicts approximately 15% high until the above 5500 m/s where it matches again.

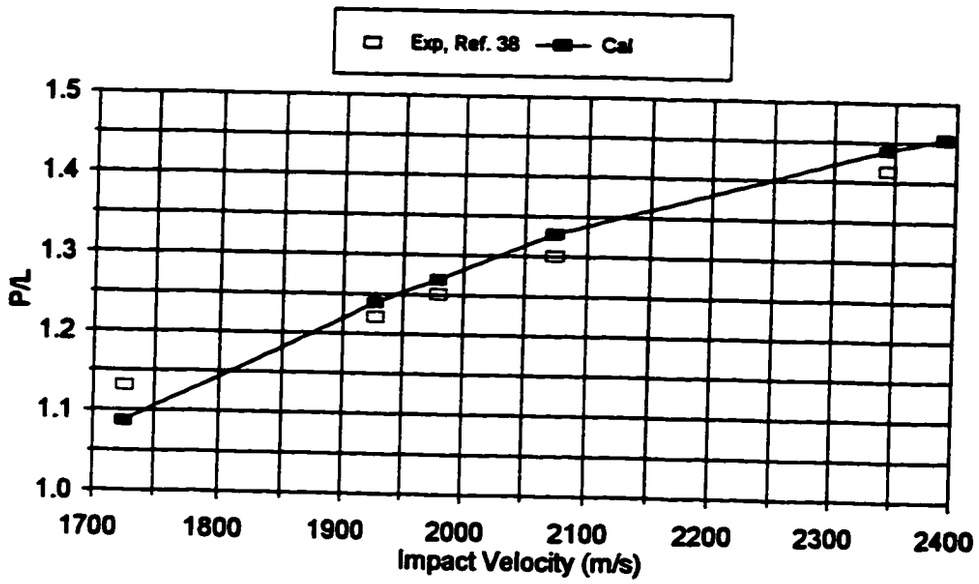

a. Crater Depth vs. Impact Velocity

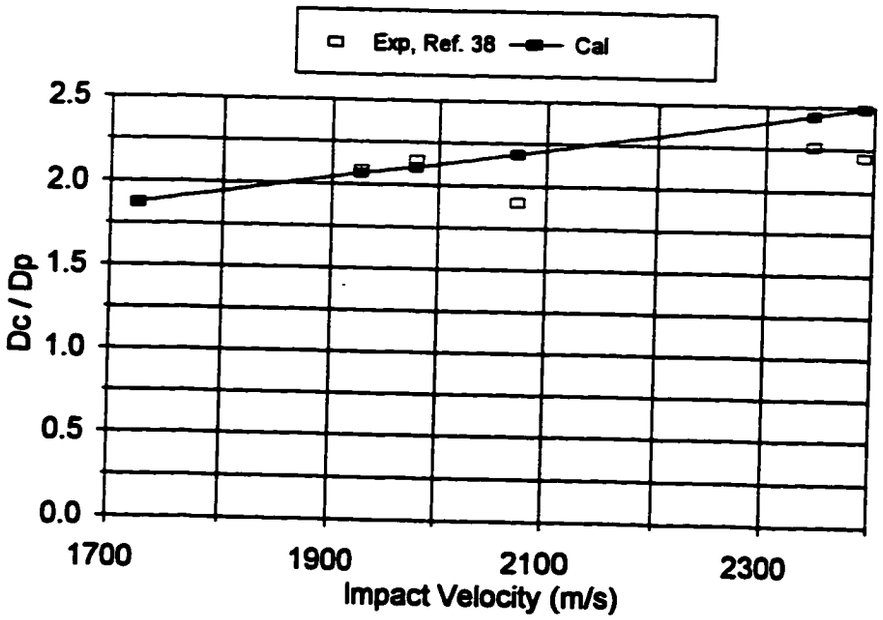

b. Crater Diameter vs. Impact Velocity

Fig. 32. U-3/4 Ti Blunt Nosetip Penetrator into RHA, L/D = 20

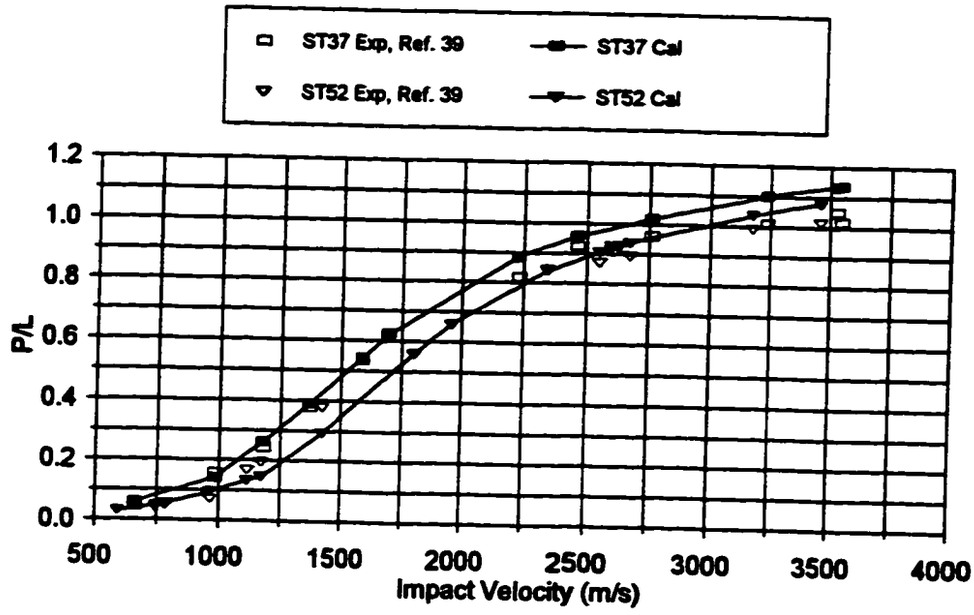

Fig. 33. Crater Depth vs Impact Velocity for C110W1 Steel Blunt Penetrator into St37 and St52 Steel, L/D = 10

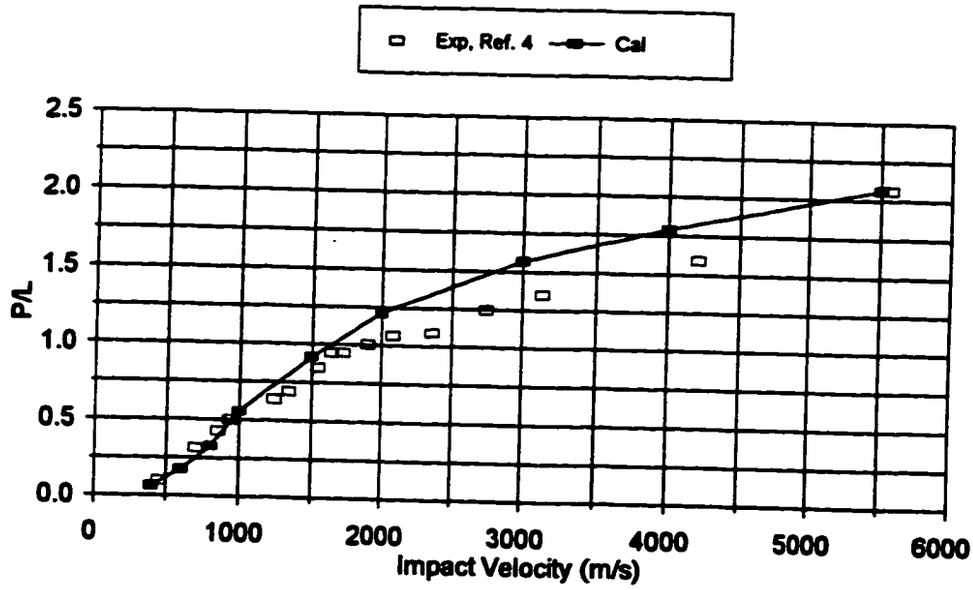

Fig. 34. Crater Depth vs Impact Velocity for 1100-0 Aluminum Blunt Penetrator into 1100-0 Aluminum, L/D = 3

Finite Thickness Targets

Fig. 35 explores the semi-infinite assumption of the current model. The residual velocity from a finite target is shown as a function of impact velocity for U-3/4 Ti into RHA. There is a lot of scatter in the experimental data, and the predictions are at the upper limit of the data band.

Fig. 36 shows the case where the penetrator does not easily perforate the target for the entire velocity range. Below 1800 m/s the code does not predict that the target will be perforated because the semi-infinite target assumed in the model has no release waves from a rear boundary to reduce target resistance. At velocities above 1800 m/s in Fig. 35, the code gives an accurate prediction of the residual velocity, presumably because the target compression wave is very near the penetrator-target interface at these higher velocities. To modify the code to allow for the finite target problem, the target compressive wave that leads the penetrator-target interface would have to reflect off the free surface at the rear of the target. When the reflected waves return to the penetrator-target interface, the stress is reduced on the penetrator. This allows the penetrator to penetrate deeper without the loss in velocity that is predicted by a semi-infinite target. This modification is a recommendation for future research.

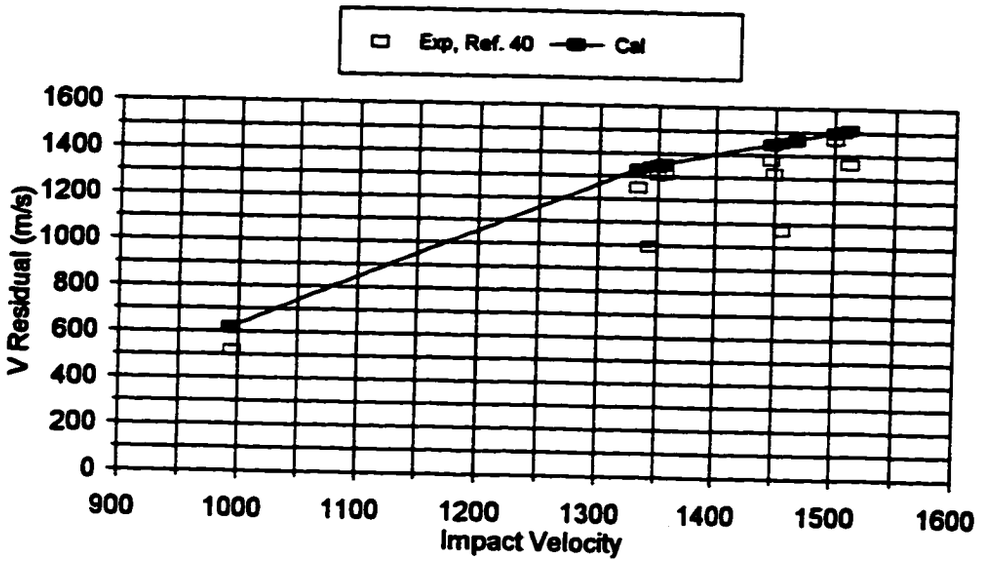

Fig. 35. Residual Velocity for a U-3/4 Ti Hemispherical Penetrator Perforating RHA, L/D = 10

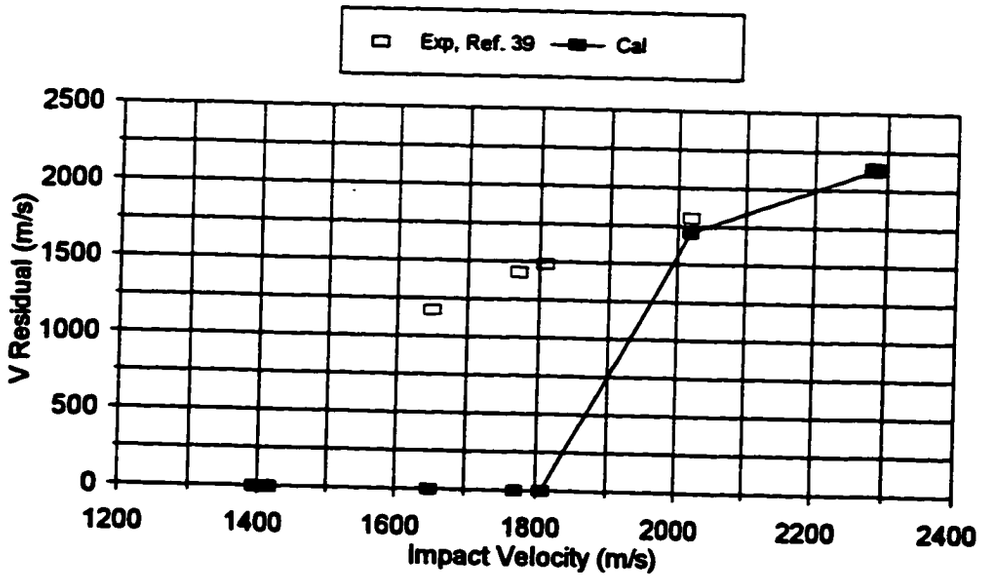

Fig. 36. Residual Velocity for a C110W1 Steel Blunt Penetrator Perforating Steel, L/D = 10

Parametric Study

The next several figures show the results of a parametric study of the influence of nosetip angle on penetration depth. The conical nosetip angles studied are 10, 20, 30, 45, 60, and 90 degrees. The 90-degree condition corresponds to a blunt penetrator. The velocity range studied is from 0 to 5000 m/s. The parametric study uses as a baseline a steel penetrator with a strength of 1900 MPa and a density of 7900 kg/m^3 and a steel target with a strength of 800 MPa and a density of 7900 kg/m^3. In the study, the penetrator and target densities are varied from 1000 to 20000 kg/m^3 and the strengths from 70 to 2000 MPa. The speed of sound, Poisson's ratio, and other variables are those for steel and are given for the target in Table 4.

Figs. 37a and 37b show the normalized penetration depth and normalized crater diameter as a function of impact velocity for the baseline case. The 10-degree nosetip penetrates almost 50% more than the 20-degree nosetip and a factor of ten more than the blunt penetrator at 1000 m/s. There is a local maximum in the 10, 20, and 30 degree curves due to the reduced pressure on the front of the nosetips at lower nosetip angles. It requires a higher impact velocity to flow the nosetip. The local maximum occurs at 1100 m/s for the 10 degree nosetip and 1000 m/s for the 20 degree nosetip. Almost no difference exists between the 45, 60,

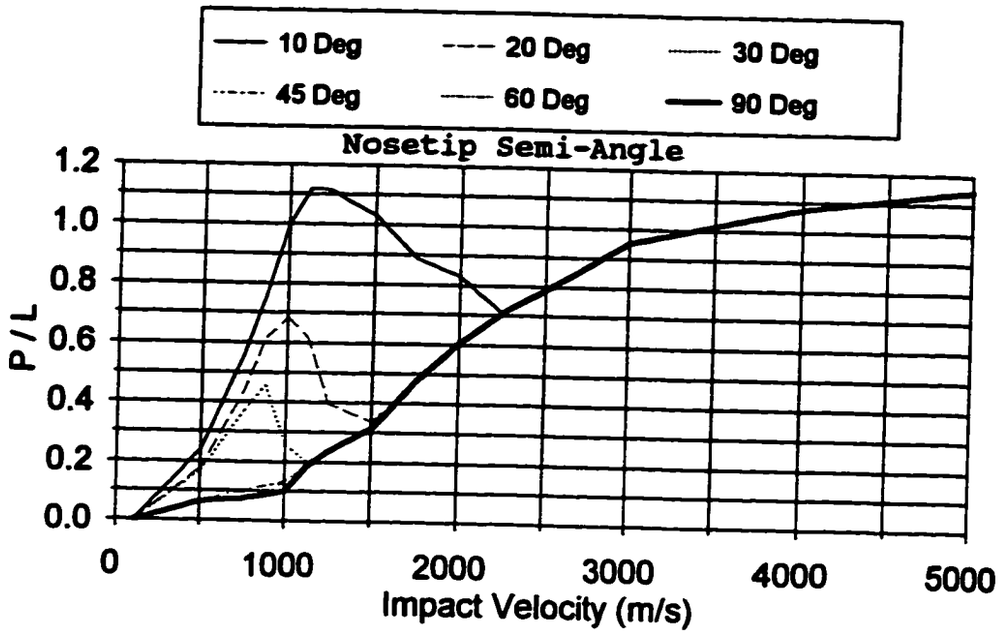

a. Penetration Depth vs. Impact Velocity

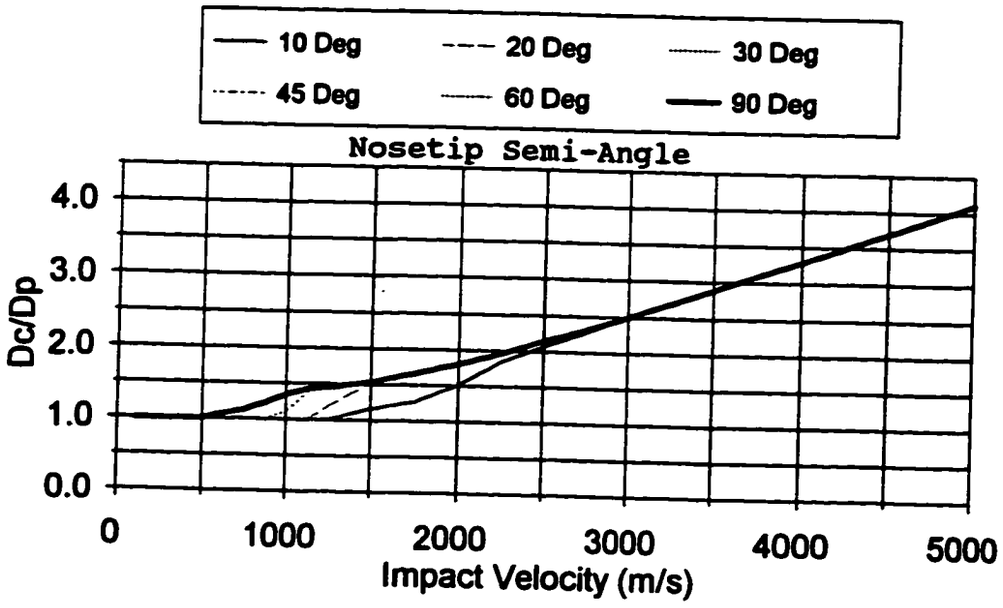

b. Crater Diameter vs. Impact Velocity

Fig. 37. Effect of Penetrator Nosetip Angle for the Baseline Case (1900 MPa, 7900 kg/m^3 Penetrator into a 800 MPa, 7900 kg/m^3 Target, L/D = 12)

and 90 degree penetration depths due to the target flowing the blunter nosetips at low-impact velocities. The crater diameters are equal to the penetrator diameter until the point where the whole nosetip flows.

Figs. 38a and 38b present the results for a low density target (1000 kg/m^3) with other properties held constant. The penetration depth for the 10 degree cone is over six times greater than for the baseline case at 2500 m/s. It is also noted that the maximum point in the penetration curve occurs at 2500 m/s instead of 1100 m/s due to a higher target flow initiation velocity compared with the baseline case. Only a small difference can be seen between the 45, 60 and 90 degree curves.

Figs. 39a and 39b present the results for a high density target (17000 kg/m^3). The crater depth is 20% less for the 10 degree nosetip than for the baseline case at 1000 m/s. The maximum points on all of the curves have shifted to lower impact velocities because of the increased target structural flow resistance and the resulting lower target flow initiation velocities. The 45, 60, and 90 degree nosetips collapse to the same curve because the target flows the nosetips at very low impact velocities.

Figs. 40a and 40b present the results for a low strength target (100 MPa). The maximum point on the curve is nine times the depth for the baseline case at the same

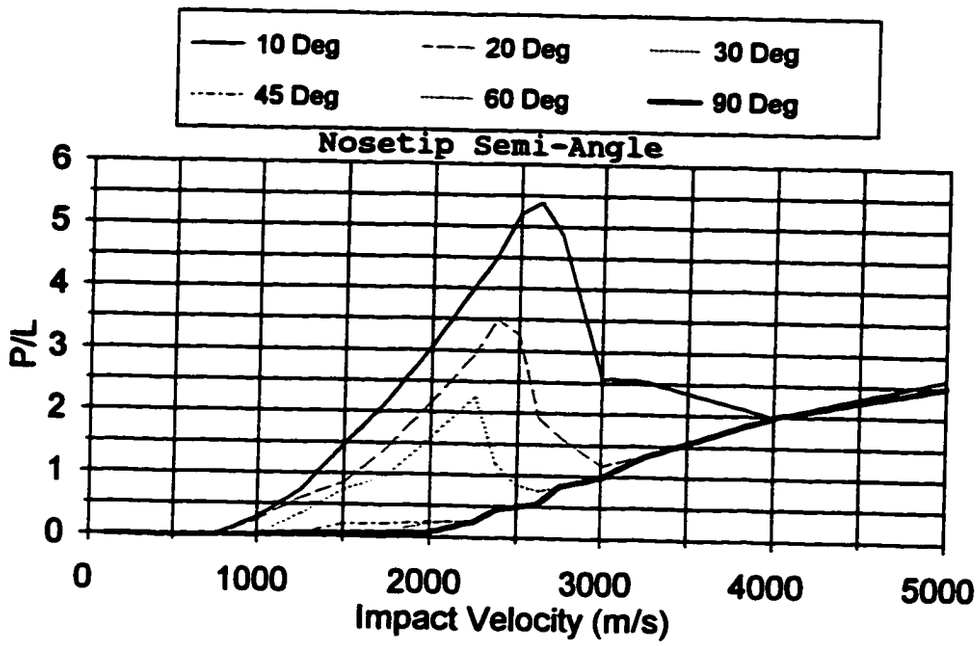

a. Penetration Depth vs Impact Velocity

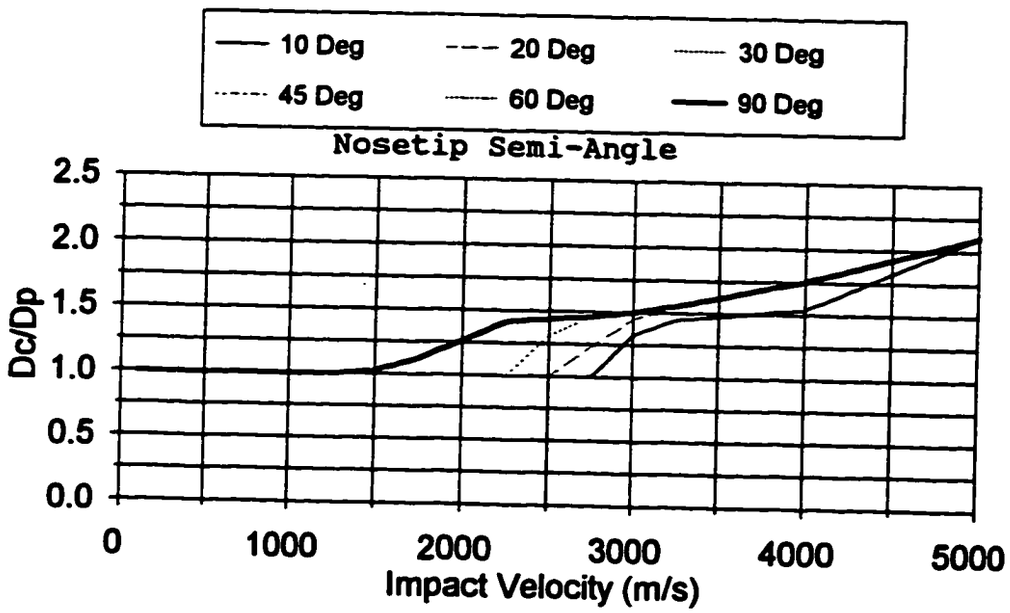

b. Crater Diameter vs Impact Velocity

Fig. 38. Effect of Penetrator Nosetip Angle for a Low Density Target (1900 MPa, 7900 kg/m^3 Penetrator into a 800 MPa, 1000 kg/m^3 Target, L/D = 12)

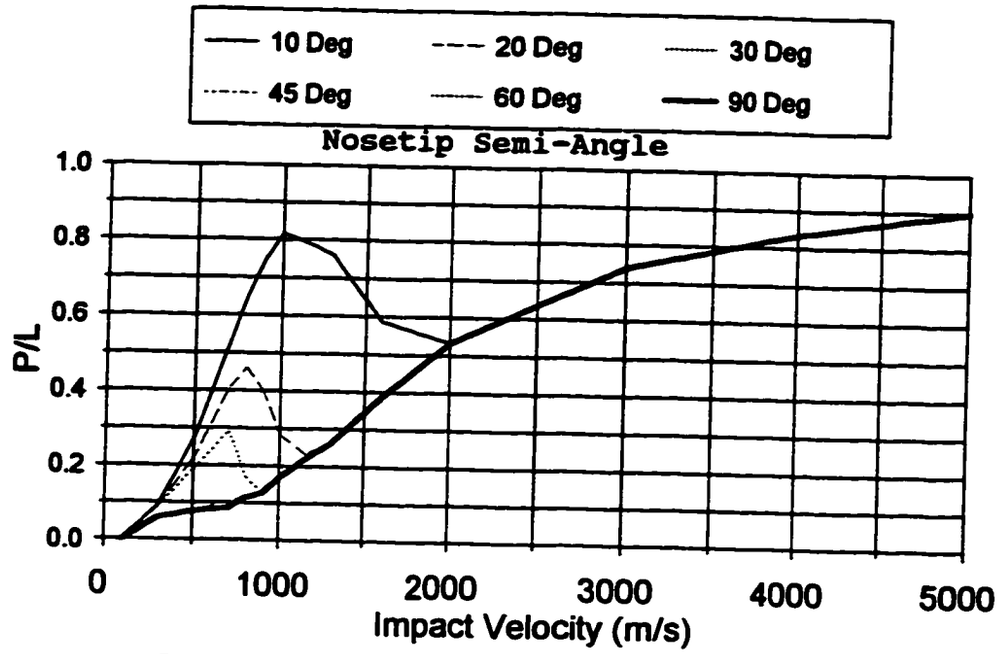

a. Penetration Depth vs. Impact Velocity

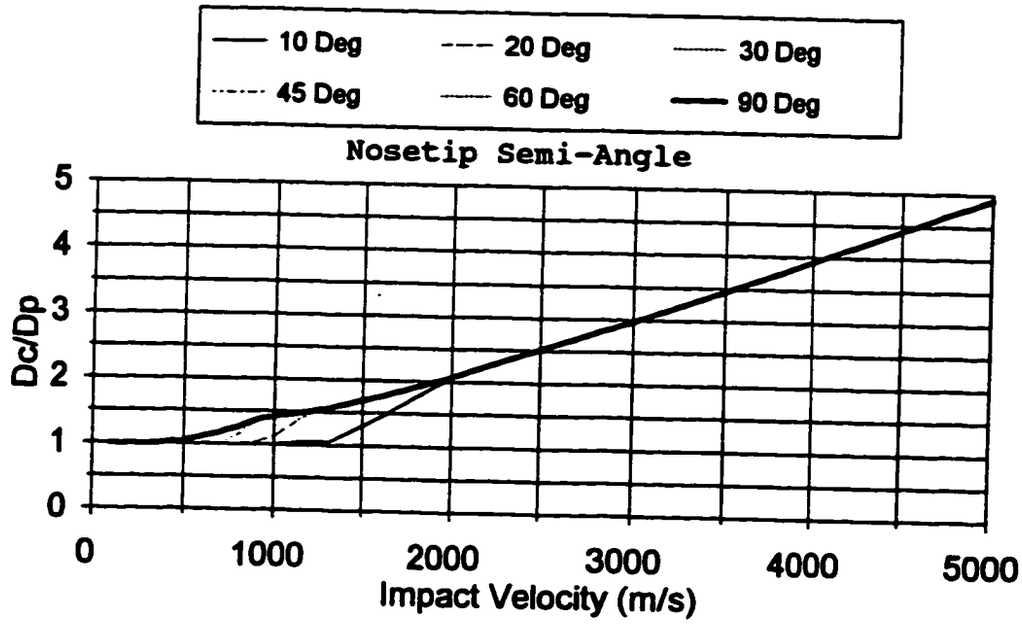

b. Penetration Depth vs. Impact Velocity

Fig. 39. Effect of Penetrator Nosetip Angle for a High Density Target (1900 MPa, 7900 kg/m^3 Penetrator into a 800 MPa, 17000 kg/m^3 Target, L/D = 12)

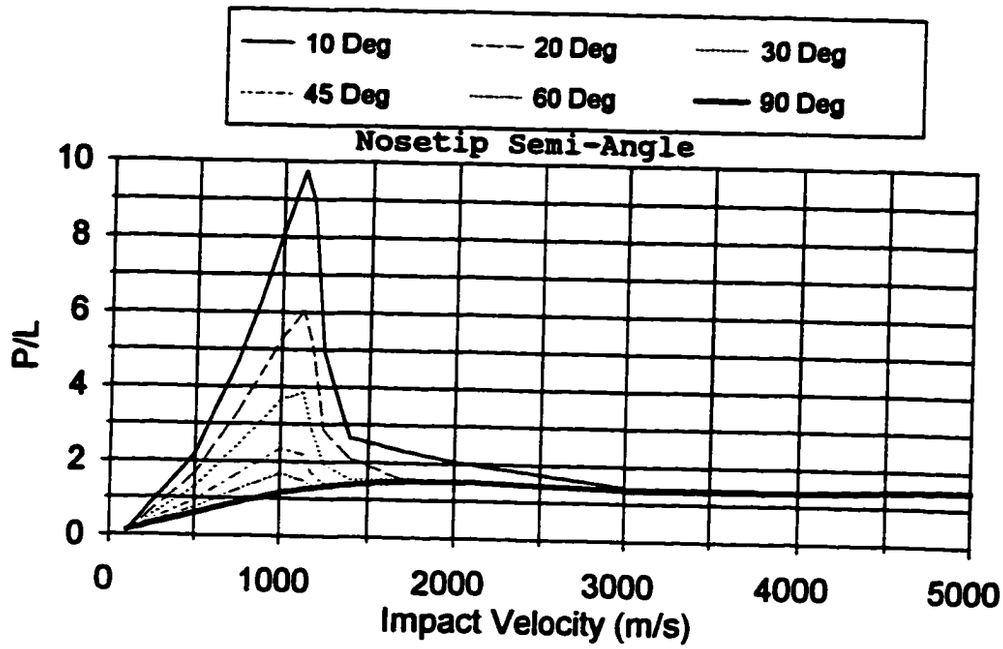

a. Penetration Depth vs. Impact Velocity

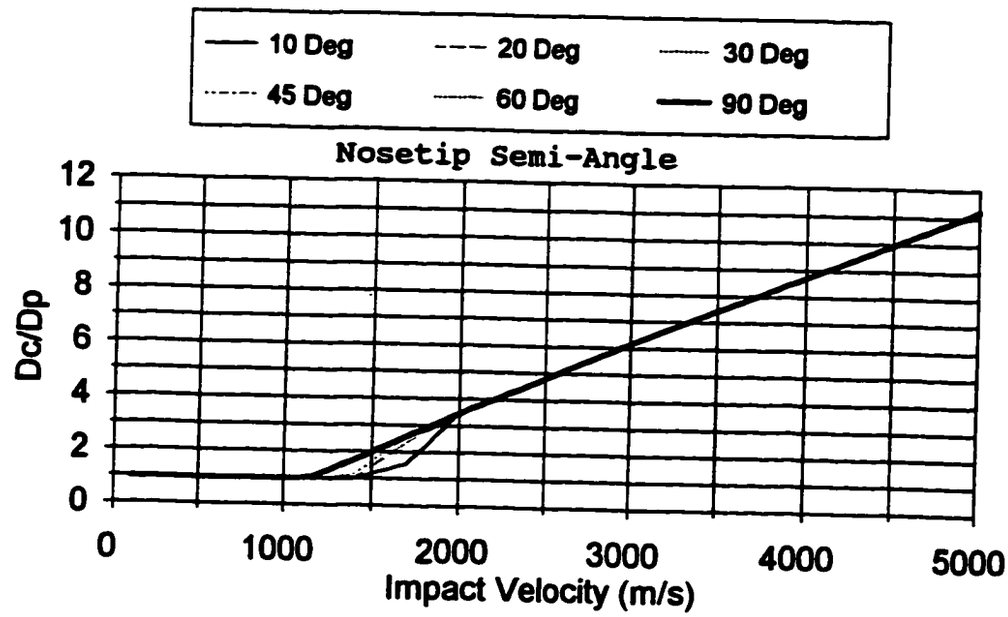

b. Crater Diameter vs. Impact Velocity

Fig. 40. Effect of Penetrator Nosetip Angle for a Low Strength Target (1900 MPa, 7900 kg/m^3 Penetrator into a 100 MPa, 7900 kg/m^3 Target, L/D = 12)

velocity. All the nosetips show much deeper penetration than for the baseline case and separate from the blunt case. The structural term in the target is small due to the low compressive strength so the resistance felt by the penetrator is mostly due to the flow resistance term.

Figs. 41a and 41b present the results for a high strength target (2000 MPa). The nosetip curves collapse to the nearly the same curve. A primary effect of the high-strength target is to flow the penetrator nosetips and quickly blunt them. This condition demonstrates a case where the penetrator nosetip has almost no effect on penetration depth. The slight increase in depth shown for the 10-degree nosetip may be solely due to the use of the average of the average nosetip angle for each wave cycle.

Figs. 42a and 42b present the results for a low density penetrator(1000 kg/m^3). The crater depths are lower than for the baseline case, but the maximum points of the curves occur at higher velocities. The increase in the penetrator flow initiation velocities is due to the increased maximum penetrator particle velocity that accompanies the low penetrator density, Eqn. (50).

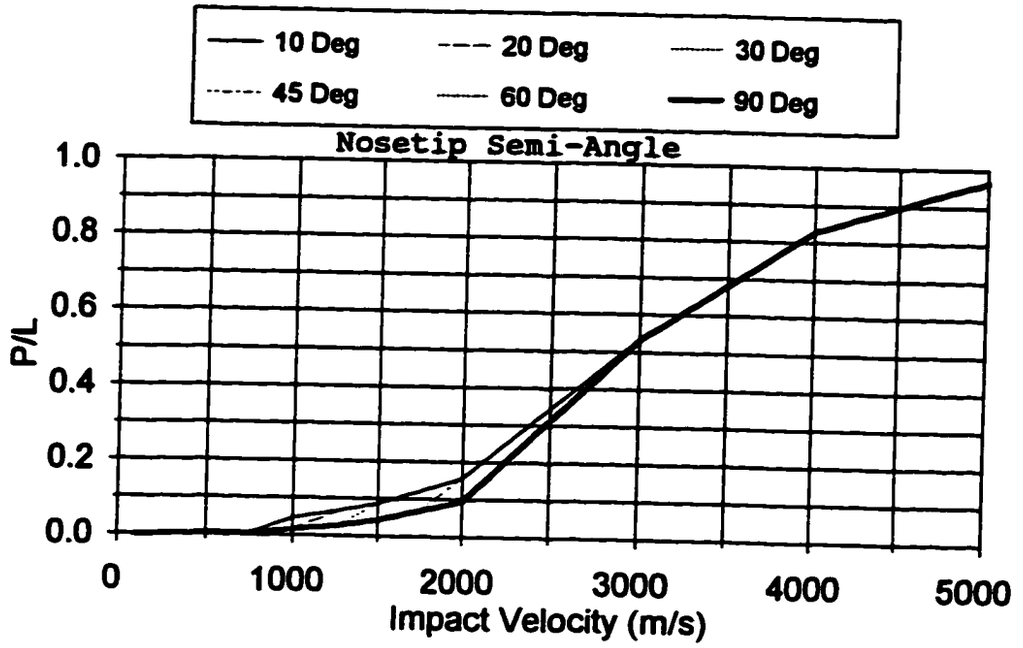

a. Penetration Depth vs. Impact Velocity

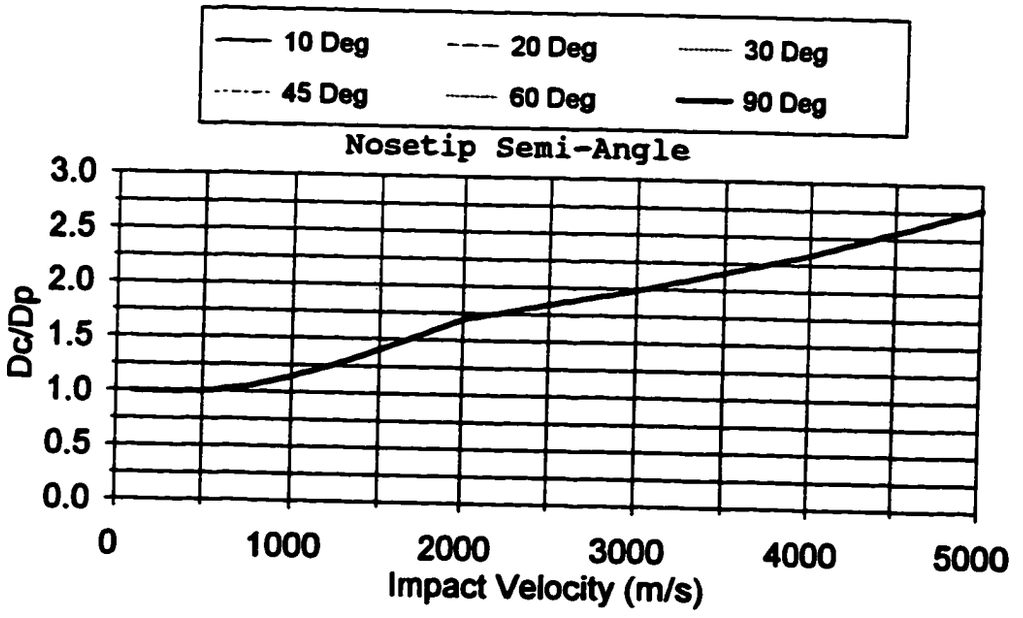

b. Crater Diameter vs. Impact Velocity

Fig. 41. Effect of Penetrator Nosetip Angle for a High Strength Target (1900 MPa, 7900 kg/m^3 Penetrator into a 2000 MPa, 7900 kg/m^3 Target, L/D = 12)

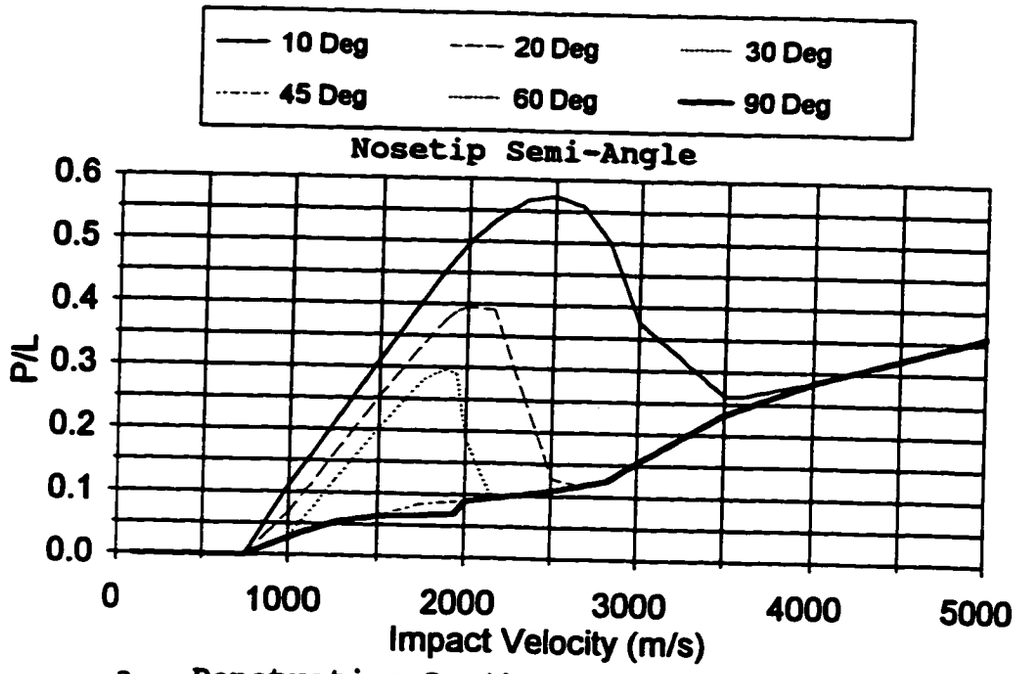

a. Penetration Depth vs. Impact Velocity

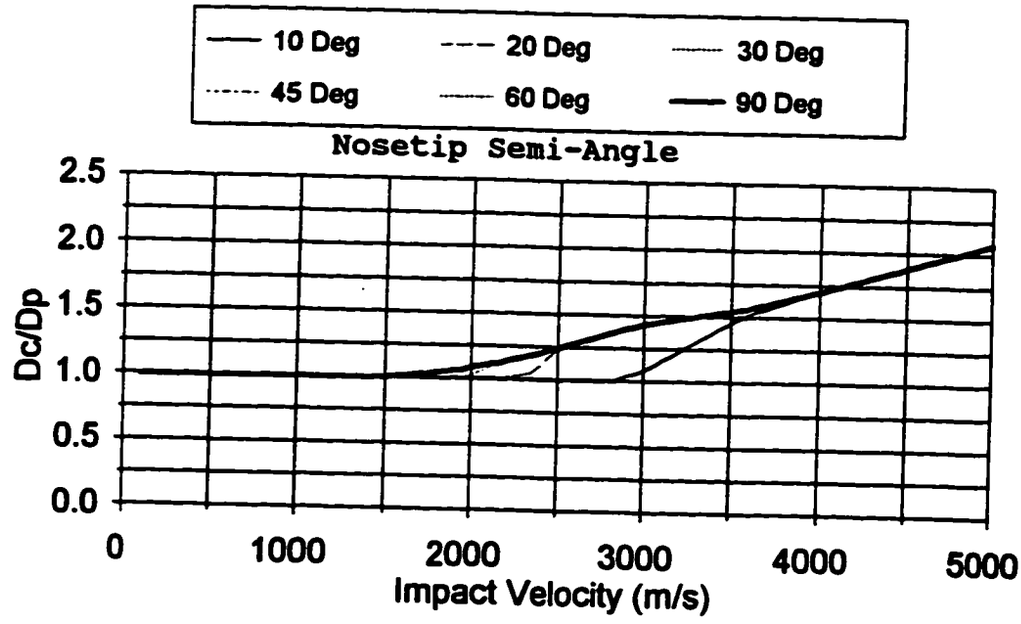

b. Crater Diameter vs. Impact Velocity

Fig. 42. Effect of Penetrator Nosetip Angle for a Low Density Penetrator (1900 MPa, 1000 kg/m^3 Penetrator into a 800 MPa, 7900 kg/m^3 Target, L/D = 12)

Figs. 43a and 43b present the results for a high density penetrator (17000 kg/m^3). The crater depth is four times the depth for the low-density penetrator for a 10-degree cone at 1500 m/s. The maximum points also occur at significantly lower velocities due to the lower maximum penetrator particle velocities.

Figs. 44a and 44b present the data for a low strength penetrator (100 MPa). The curves all collapse to a single curve as in Fig. 41a. All of the nosetips flow at low impact velocities because the target resistance exceeds the free surface structural strength of the relatively weak penetrators.

There is no graph for a high-strength penetrator. The baseline penetrator is already near the maximum for steel penetrator strength. Armor-piercing cores can have strengths up to 2000 MPa, but the penetrator is very brittle and can fracture upon impact.

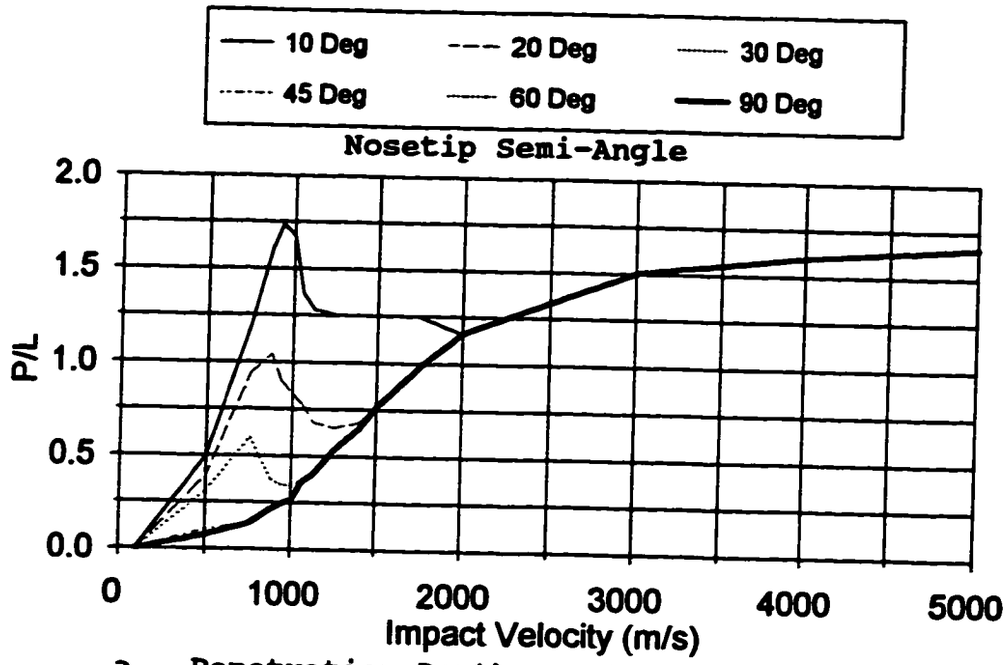

a. Penetration Depth vs. Impact Velocity

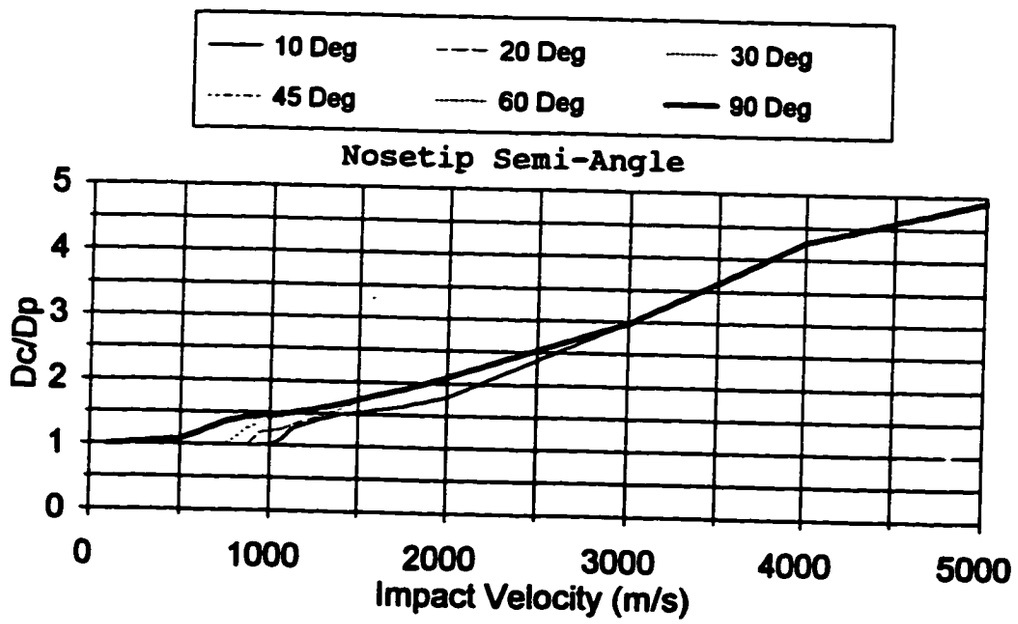

b. Crater Diameter vs. Impact Velocity

Fig. 43. Effect of Penetrator Nosetip Angle for a High Density Penetrator (1900 MPa, 17000 kg/m^3 Penetrator into a 800 MPa, 7900 kg/m^3 Target, L/D = 12)

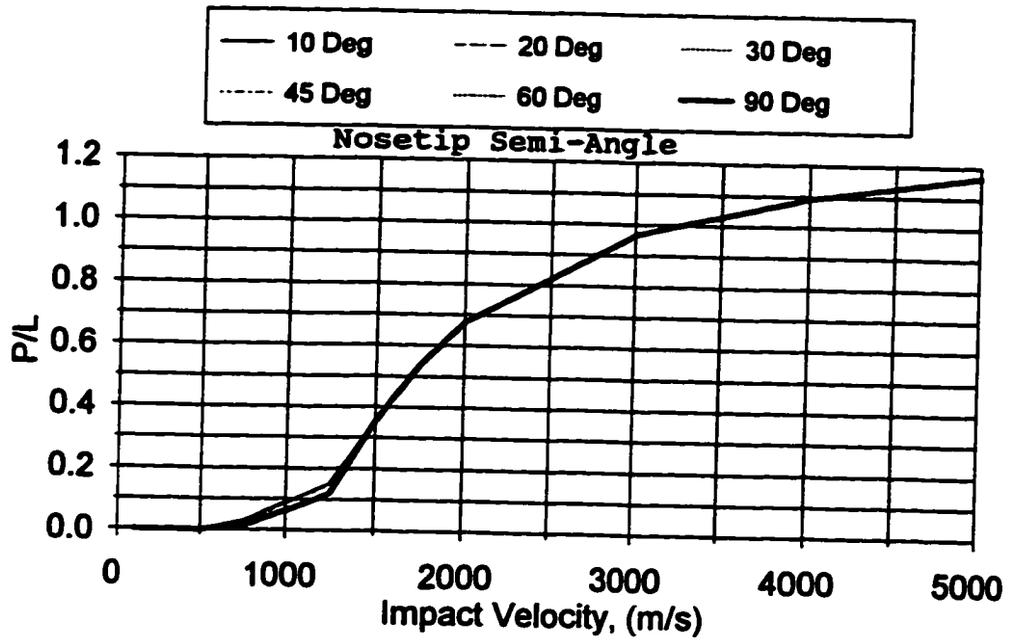

a. Penetration Depth vs. Impact Velocity

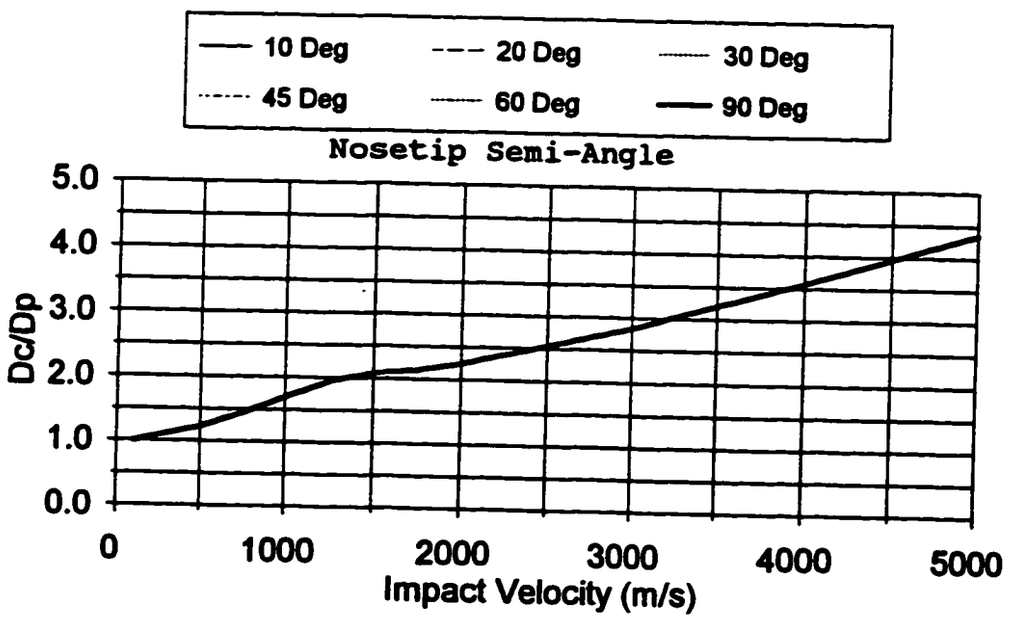

b. Penetration Depth vs. Impact Velocity

Fig. 44. Effect of Penetrator Nosetip Angle for a Low Strength Penetrator (100 MPa, 7900 kg/m^3 Penetrator into a 800 MPa, 7900 kg/m^3 Target, L/D = 12)

The parametric study results presented in Figs. 45-49 assumes a constant, 20-degree conical nosetip, and varies the penetrator and target strengths and densities. For the properties not being varied, the baseline properties are used.

Figs. 45a and 45b present the results obtained for different target densities from 1000 to 20000 kg/m^3. The maximum target particle velocity is inversely proportional to the target density, with other properties held constant. A higher maximum target particle velocity causes a higher target flow initiation velocity. This effect is seen by examining the low-density target penetration depth below 1000 m/s. The penetration depth is very low when the impact velocity is below the target flow initiation velocity. When the impact velocity is above the target flow initiation velocity, the low density in the flow stress term causes a lower stress on the penetrator. This effect delays penetrator flow initiation to a higher velocity for the lower density targets. The crater diameter is formed by the penetrator flow momentum, so the higher the flow stress term in the target, the higher the penetrator flow momentum and the larger the crater diameter.

Figs. 46a and 46b present the results obtained for different target strengths from 70 to 2000 MPa. The low

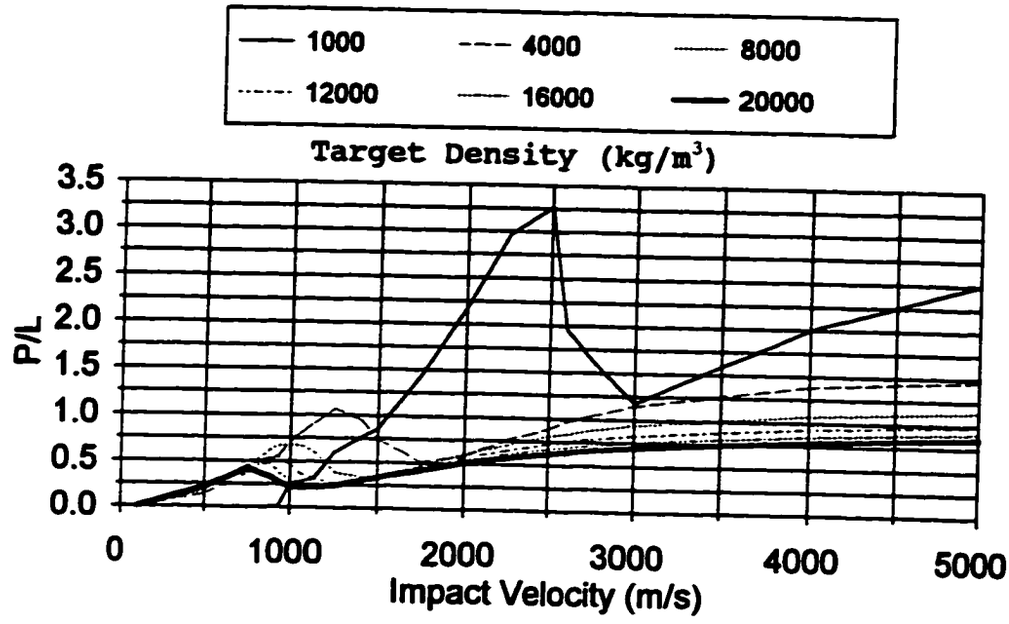

a. Penetration Depth vs. Impact Velocity

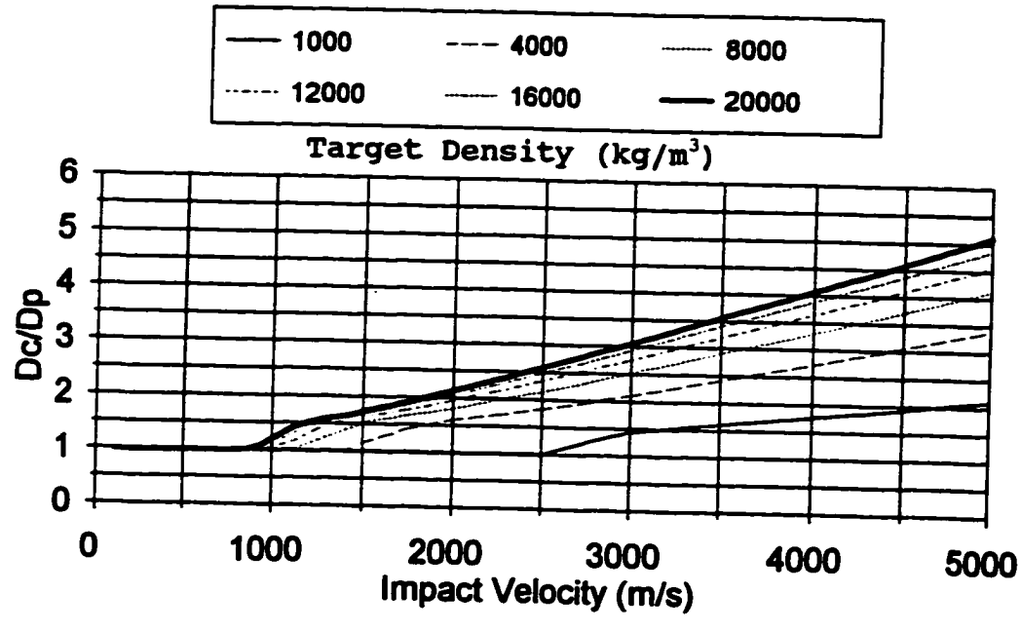

b. Crater Diameter vs. Impact Velocity

Fig. 45. Effect of Target Density (1900 MPa, 7900 kg/m³ Penetrator into a 800 MPa Target, L/D = 12, 20-Degree Conical Nosetip)

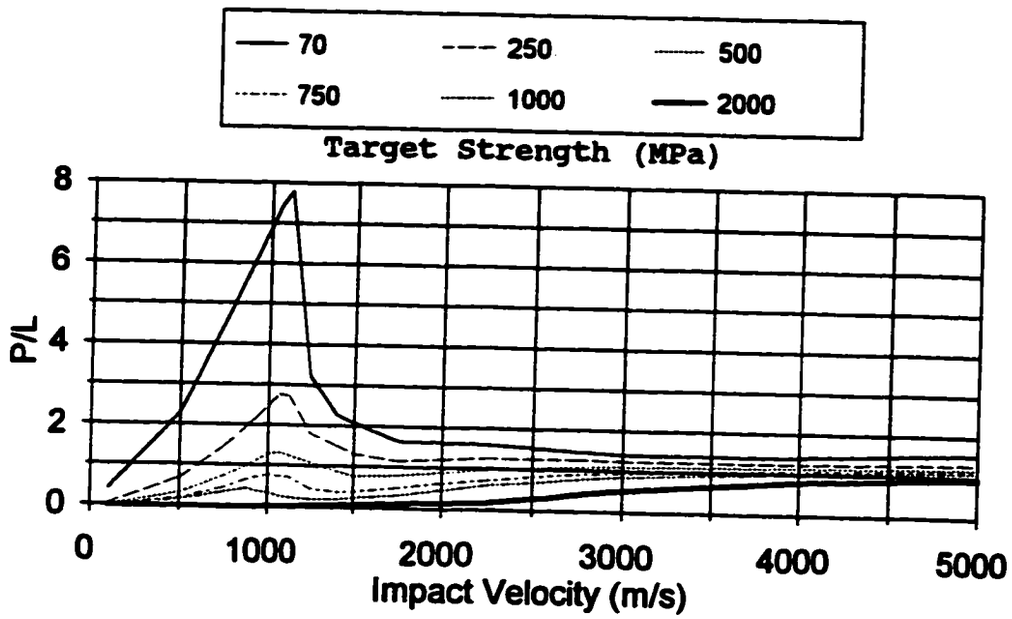

a. Penetration Depth vs. Impact Velocity

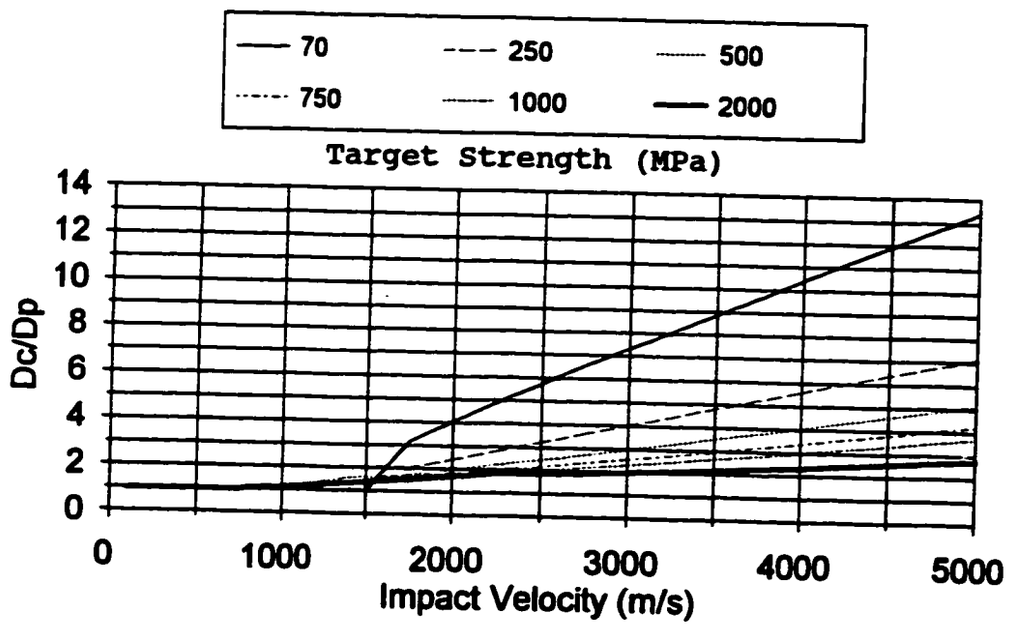

b. Crater Diameter vs. Impact Velocity

Fig. 46. Effect of Target Strength (1900 MPa, 7900 kg/m^3 Penetrator into a 7900 Kg/m^3 Target, L/D = 12, 20-Degree Conical Nosetip)

structural stress for the low target strengths causes the target to flow at very low velocities. The high structural stress at a higher target strength causes the penetrator to flow at a low impact velocity, blunts the nosetip, and reduces penetration into the target. The crater diameter is a function of the target strength so with a low target strength, the crater formed is very large compared with a high strength target.

Figs. 47a and 47b presents the results obtained for different penetrator densities from 1000 to 20000 kg/m^3. A low-density penetrator has a higher maximum particle velocity and therefore a higher target flow initiation velocity than a higher density penetrator. At the higher-impact velocities the penetration is slightly above the square root of the ratio of the penetrator density to the target density. This greater penetration depth is due principally to the terminal transient.

Figs. 48a and 48b present the results obtained for different penetrator strengths from 70 to 2000 MPa. All the penetrators, except the 2000 MPa case, begin to flow at low velocities because the confined target structural strength is greater than the penetrator free-surface structural

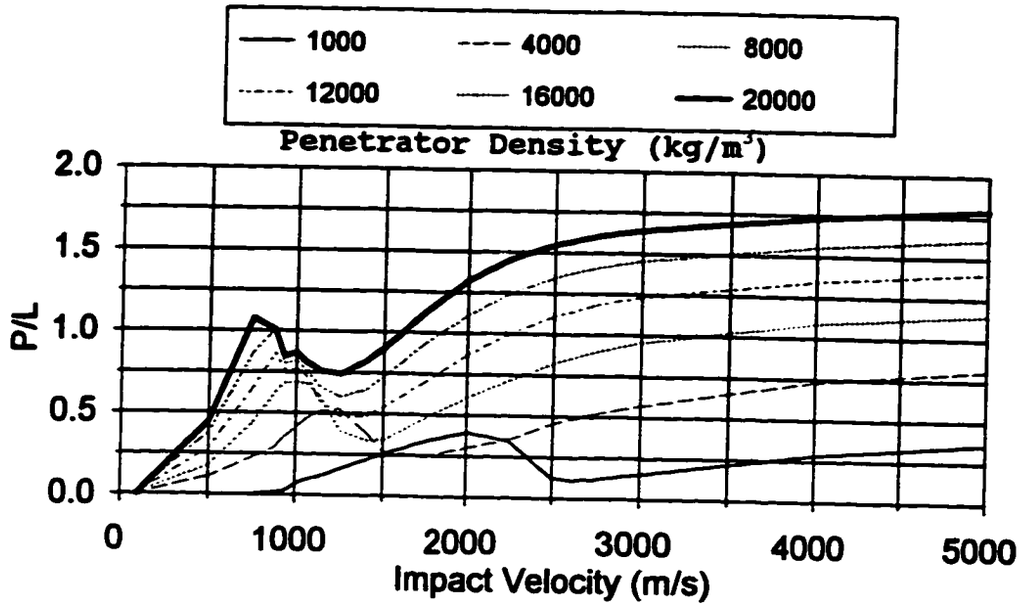

a. Penetration Depth vs. Impact Velocity

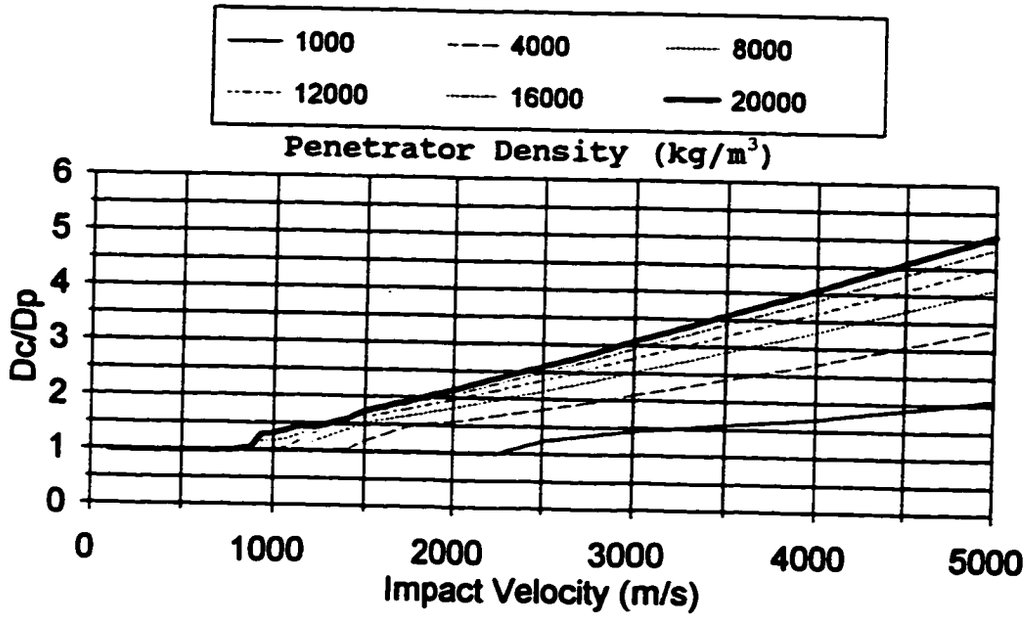

b. Crater Diameter vs. Impact Velocity

Fig. 47. Effect of Penetrator Density (1900 MPa, Penetrator into a 800 MPa, 7900 kg/m³ Target, L/D = 12, 20-Degree Conical Nosetip)

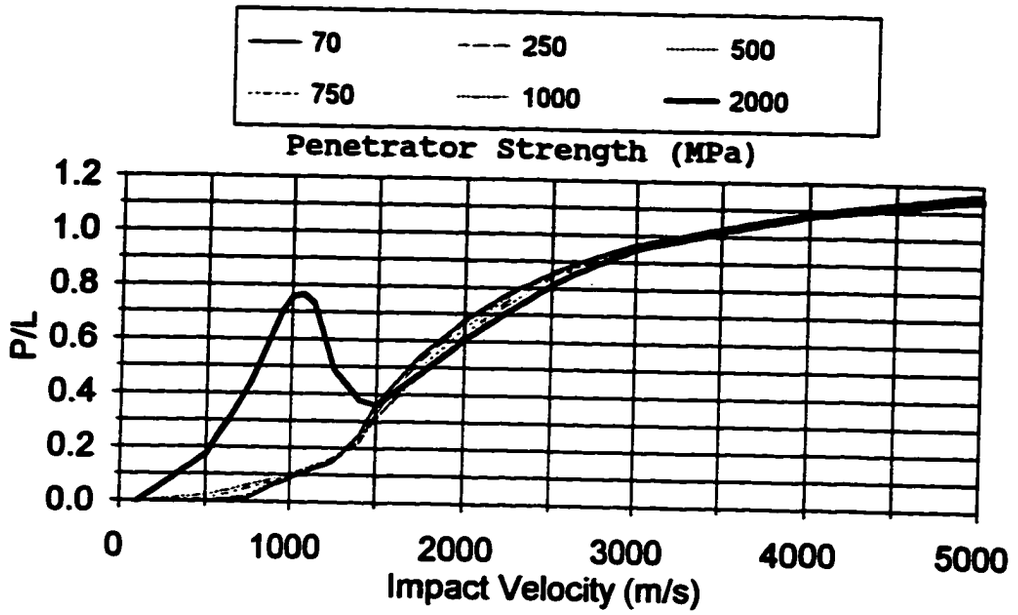

a. Penetration Depth vs. Impact Velocity

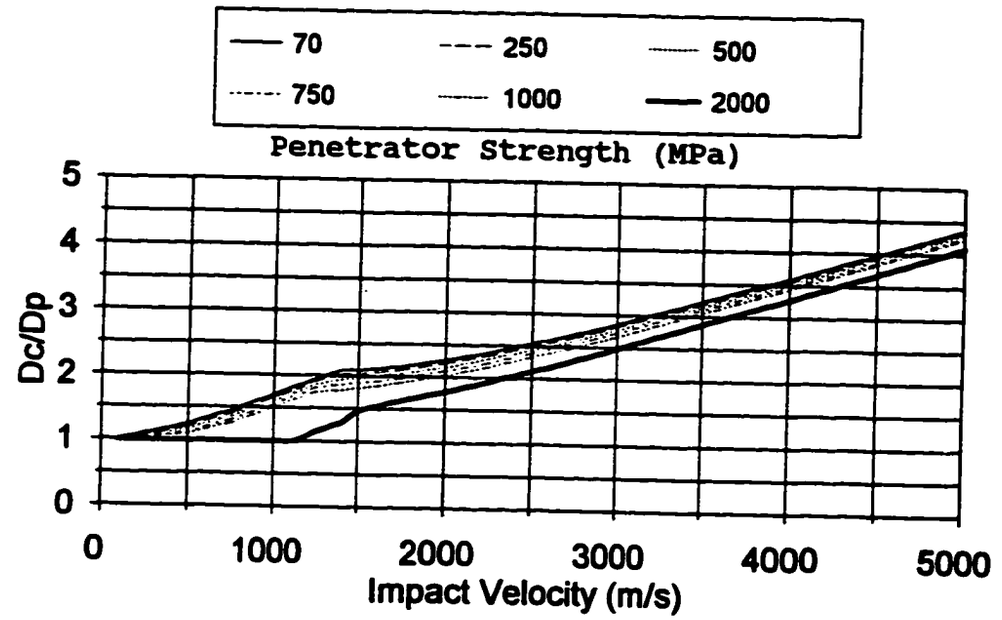

b. Crater Diameter vs. Impact Velocity

Fig. 48. Effect of Penetrator Strength (7900 Kg/m^3, Penetrator into a 800 MPa, 7900 kg/m^3 Target, L/D = 12, 20-Degree Conical Nosetip)

strength. At the highest penetrator strength, the penetrator free-surface structural strength is greater than the target confined surface structural strength and remains non-deformed until an impact velocity of 1100 m/s.

Figs. 49a and 49b present the results obtained for various length to diameter ratios for the baseline materials. The penetration depth is nearly the same until 900 m/s and only varies by the small initial transient. When the nosetip begins to flow at 900 m/s the length of the penetrator has a significant effect. The longer the penetrator, the longer the time for each wave cycle, and the lower the deceleration of the penetrator. This has the effect, for short penetrators, of reducing the velocity of the penetrator below the point at which the nosetip will flow much more quickly than for long penetrators. The longer penetrators tend to cause the entire nosetip to blunt during the first wave cycle.

Figs. 50a and 50b show the effects of nosetip angle on penetration depth for a baseline penetrator into a 70 MPa concrete target. The 10-degree nosetip penetrates over a factor of two over the 20-degree nosetip at 1600 m/s, the local maximum point. The calculation includes the nosetip erosion equation with a aggregate constant of five.

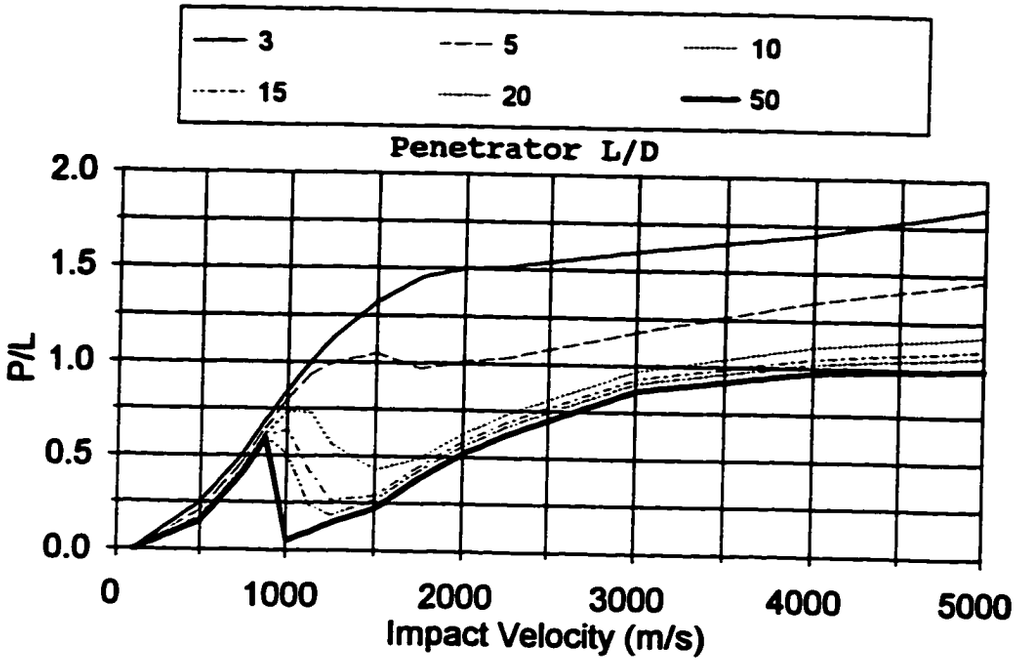

a. Penetration Depth vs. Impact Velocity

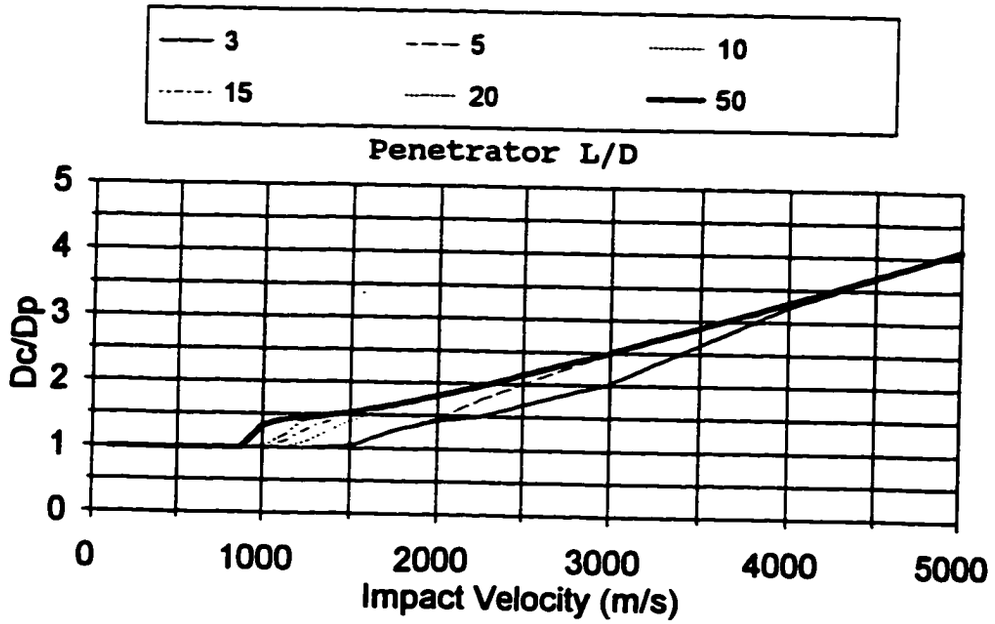

b. Crater Diameter vs. Impact Velocity

Fig. 49. Effect of Penetrator L/D (1900 MPa, 7900 Kg/m^3, Penetrator into a 800 MPa, 7900 kg/m^3 Target, 20-Degree Conical Nosetip)

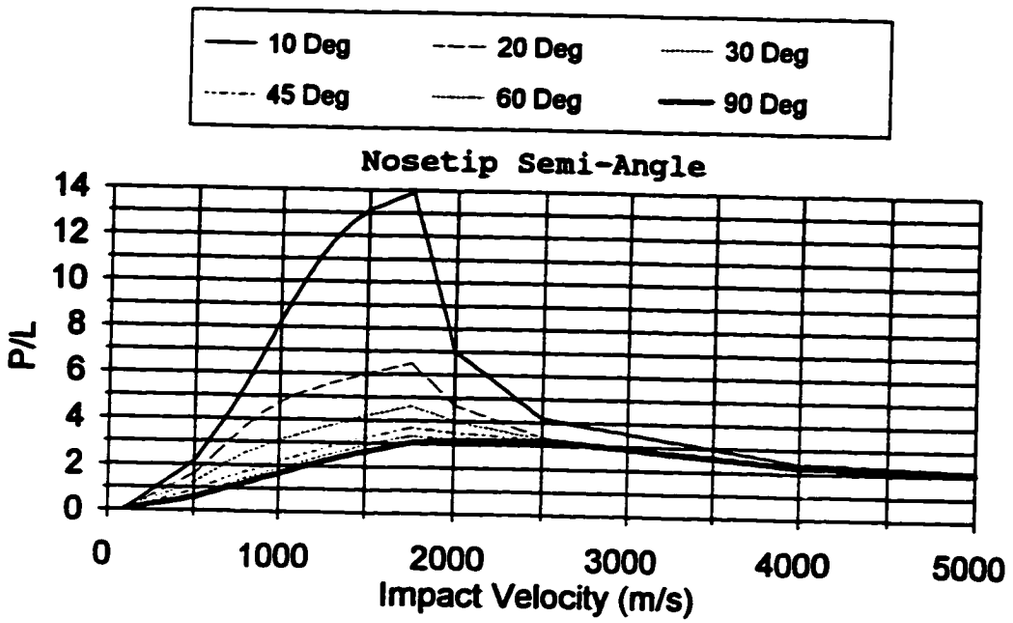

a. Penetration Depth vs. Impact Velocity

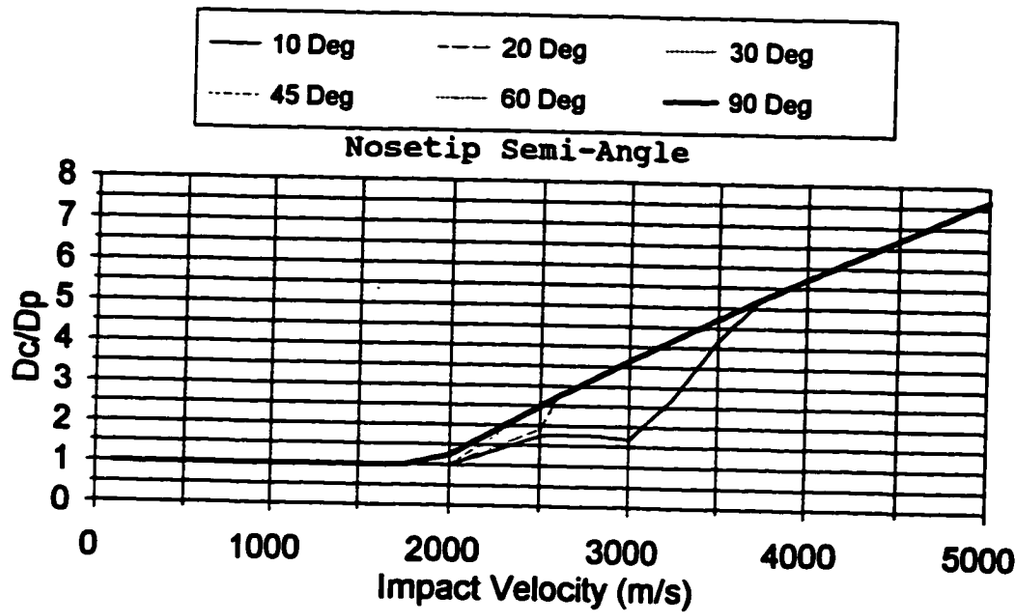

b. Crater Diameter vs. Impact Velocity

Fig. 50. Effect of Penetrator Nosetip Angle for Steel into 70 MPa Concrete (1900 MPa, 7900 kg/m^3 Penetrator into a 70 Mpa, 2300 kg/m^3 Target, L/D = 12)

CHAPTER 10

CONCLUSIONS AND RECOMMENDATIONS

The purpose of this investigation was to extend the previous work, (Ref. 1) to include angular nosetips. Terminal ballistics phenomena are categorized into three distinct regimes--the initial transient, the developed penetration process, and the terminal transient. It is postulated that the compression waves generated during the impact event control the penetrator deceleration as well as all other penetrator and target responses in all three regimes. The penetrator and target velocities are each divided into two components, the compression velocity or particle velocity, which is due to the change in velocity across the disturbance wave as it travels through the material, and the flow velocity, which is the velocity of the material as it relieves the pressure at the penetrator-target interface.

There is another flow velocity postulated to occur for angular nosetips. This velocity is the nosetip flow velocity which occurs at the penetrator centerline in response to the flow resistance of the target stream and the target structural resistance. The nosetip flows because, no

matter how sharp, it would always have a blunt surface at the centerline. This bluntness causes an increase in the pressure only at the centerline so that the centerline region will flow before the rest of the nosetip.

Conclusions

1. A one-dimensional model based on the penetrator-target interface integral momentum equation gives predictions of crater depth and diameter to within the experimental uncertainty of available data for a wide range of penetrator and target materials, impact velocities, and penetrator L/D ratios. This agreement is obtained by a completely physically-based model without resort to empiricisms.
2. The penetrator-target interface integral momentum equation gives the correct relationship between the penetrator and target structural resistance terms and the hydrodynamic flow terms. The Bernoulli equation upon which the Tate model is based does not model this relationship correctly.
3. The maximum penetrator structural resistance is directly proportional to the compressive strength and inversely proportional to Poisson's ratio because the stress due to the compression waves in the penetrator is relieved by flow normal to the direction of the

induced particle velocities at the penetrator-target interface.

4. The maximum target structural resistance for a blunt nosetip is directly proportional to the compressive strength and inversely proportional to Poisson's ratio squared because the stress due to the compression waves in the target is relieved by flow around the target which is 180 degrees from the direction of the induced particle velocities at the penetrator-target interface.
5. The influence of an angular nosetip is to reduce both the target hydrodynamic flow stress and maximum target structural stress. The hydrodynamic flow stress is reduced by the multiplying factor $(1 - \cos \theta)$, and the structural stress is reduced by utilizing $(1 + \sin \theta)$ for the Poisson's ratio exponent where θ is the frontal area averaged nosetip semi-angle.
6. The difference in normalized crater depths for different L/D blunt penetrators is due almost entirely to the terminal transient with a small influence of the initial transient. The normalized depths due to the developed erosion are identical.
7. The penetrator erosion observed in the penetration of concrete and geologic targets at impact velocities below the nosetip flow velocity are due to the high stresses associated with the Hugoniot compression waves

generated when the nosetip encounters the aggregate and/or grains in the material. An empirically correlated erosion term gives an accurate prediction of the recovered penetrator length and penetrator mass loss.

8. The penetration depth of a 10-degree semi-angle conical nosetip, high-strength penetrator can be up to 10 times greater than for a blunt penetrator at the same impact velocity.

9. For sufficiently high impact velocity, the angled nosetip will begin to flow, and the penetration depth will decrease for higher impact velocities. As impact velocity increases beyond this regime the penetration depths for angled nosetips approach the blunt penetrator values because the nosetips will blunt during penetration.

10. The superior performance of ceramics at low velocities is associated with the low material density coupled with high compressive strength. These factors result in a high target flow initiation velocity. At velocities significantly above the target flow initiation velocity, the low density of ceramic materials results in greater penetration depth than for a higher density material such as a steel of equal strength.

Recommendations

1. Further refinement of the erosion term for granular materials is needed with the goal of incorporating aggregate and/or grain properties into the model so that empirical correlations can be avoided.
2. The initial transient model needs to be revisited to more accurately assess the quantity of shocked material removed during the transient time.
3. The terminal transient needs additional study to better define the expansions due to the target and penetrator momentum.
4. Extension of the model to finite thickness targets where perforation is expected should be pursued by accounting for the bow compression region interactions with the rear surface.
5. The energy equation needs to be developed and linked to the conservation of momentum and mass equations to allow study of hypervelocity impacts where the penetrator and target are melted or vaporized. The temperatures of the penetrator and target materials could be predicted during and after crater formation. This would allow better prediction of that portion of the hypervelocity region where heat generation and heat transfer becomes important.

APPENDIX A

EQUATION CALCULATION ORDER

Equation Calculation Order

The following is the order in which the equations are solved to make impact calculations. They may be coded into a spreadsheet or into any computer language.

The average nosetip angle

$$\theta = \frac{1}{A_p}\int_0^{A_p} \theta_p \, dA \qquad (22)$$

The penetrator and target free surface and confined maximum stress constants

$$C_{sp} = \nu_p^{-1} \quad and \quad C_{st} = \nu_t^{-[1+\sin(\theta)]} \qquad (7)\&(32)$$

The maximum particle velocity in the penetrator and the target

$$Solve\ for\ U_{ppm} \rightarrow \rho_p U_{ppm} V_{sp} = C_{sp}\sigma_{sp} \quad with \quad V_{sp} = C_{op} + S_{ip} U_{ppm} \qquad (6)$$

$$Solve\ for\ U_{ptm} \rightarrow \rho_t U_{ptm} V_{st} = C_{st}\sigma_{st} \quad with \quad V_{st} = C_{ot} + S_{it} U_{ptm} \qquad (31)$$

Maximum allowable stress in the penetrator and the target

$$S_p' = \rho_p U_{ppm} V_{sp} \quad and \quad S_t' = \rho_t U_{ptm} V_{st} \qquad (5)\&(30)$$

The increased density across the penetrator and target compression wave

$$\rho_p' = \rho_p\left(\frac{V_{sp}}{V_{sp} - U_{pp}}\right) \quad and \quad \rho_t' = \rho_t\left(\frac{V_{st}}{V_{st} - U_{pt}}\right) \qquad (2)\&(27)$$

The following if-then block is used to calculate the target, penetrator, and centerline flow initiation velocity:

If $S_p' > S_t'$ then

$$V_{pfi} = U_{ptm} + U_{ppm} + \sqrt{\frac{S_p' - S_t'}{\rho_t'[1 - \cos\theta]}} \qquad (71)\&(72)$$

$$V_{pfni} = U_{ptm} + U_{ppm} + \sqrt{\frac{S_p' - S_t'}{\rho_t'}} \qquad (73)\&(74)$$

$$V_{tfi} = U_{ptm} + U_{pp} \quad Solve\ for\ U_{pp} \rightarrow \rho_p U_{pp} V_{sp} = S_t' \qquad (70)$$

else

$$V_{tfi} = U_{ptm} + U_{ppm} + \sqrt{\frac{S_t' - S_p'}{\rho_p'}} \qquad (77)$$

$$V_{pfi} = U_{ppm} + U_{pt} \quad Solve\ for\ U_{pt} \rightarrow \rho_t U_{pt} V_{st} = S_p' \qquad (75)$$

end if

This section solves for U_{pf}, U_{tf}, U_{pp}, U_{pt}

If $V_p < V_{pfi}$ and $V_p < V_{tfi}$ then solve simultaneously for U_{pp} and U_{pt}

$$\rho_p U_{pp} V_{sp} = \rho_t U_{pt} V_{st} \qquad (68)$$

$$V_{sp} = C_{op} + S_{ip} U_{pp} \quad and \quad V_{st} = C_{ot} + S_{it} U_{pt} \qquad (55)\&(57)$$

$$V_p = U_{pp} + U_{pt} \qquad (21)$$

$$U_{pf} = 0 \quad and \quad U_{tf} = 0$$

else if $V_p < V_{pfi}$ and $V_p > V_{tfi}$ then solve simultaneously for U_{pp} and U_{tf}

$$\rho_p U_{pp} V_{sp} = S_t' + \rho_t' U_{tf}^2 (1 - \cos\theta) \qquad (64)$$

$$V_{sp} = C_{op} + S_{ip} U_{pp} \qquad (55)$$

$$V_p = U_{pp} + U_{ptm} + U_{tf} \tag{21}$$

$$U_{pf} = 0 \quad and \quad U_{pt} = U_{ptm}$$

else if $V_p > V_{pfi}$ and $V_p < V_{tfi}$ then solve simultaneously for U_{pt} and U_{pf}

$$S_p' + \rho_p' U_{pf}^2 = \rho_t U_{pt} V_{st} \tag{66}$$

$$V_{st} = C_{ot} + S_{it} U_{pt} \tag{57}$$

$$V_p = U_{ppm} + U_{pt} + U_{pf} \tag{21}$$

$$U_{tf} = 0 \quad and \quad U_{pp} = U_{ppm}$$

else if $V_p > V_{pfi}$ and $V_p > V_{tfi}$ then solve simultaneously for U_{pf} and U_{tf}

$$S_p' + \rho_p' U_{pf}^2 = S_t' + \rho_t' U_{tf}^2 (1 - \cos\theta) \tag{59}$$

$$V_p = U_{ppm} + U_{ptm} + U_{pf} + U_{tf} \tag{21}$$

$$U_{pt} = U_{ptm} \quad and \quad U_{pp} = U_{ppm}$$

end if

Initial transient (execute 1 time at beginning)

$$\rho_p U_{pph} V_{sph} = \rho_t U_{pth} V_{sth} \tag{85}$$

$$V_p \sin\theta = U_{pph} + U_{pth} \tag{86}$$

$$V_{sph} = C_{op} + S_{ip} U_{pph} \quad and \quad V_{sth} = C_{ot} + S_{it} U_{tth}$$

Solve the above for U_{pph} and U_{pth}

$$\Delta t_{it} = \frac{r_{pr}}{V_{sph}} \tag{87}$$

$$Time = \Delta t_{it}$$

$$if\ U_{pth} < U_{ptm}\ then\ L_{cl} = 0\ else\ L_{cl} = (U_{pth} - U_{ptm})\,\Delta t_{it} \tag{88}$$

$$if\ U_{pph} < U_{ppm}\ then\ \Delta L_{pl} = 0\ else\ \Delta L_{pl} = -(U_{pph} - U_{ppm})\,\Delta t_{it} \tag{89}$$

End Initial Transient

If $V_p < V_{pfni}$ then

$$U_{pfn} = 0$$

else solve the following for U_{pfn}

$$S_p' + \rho_p' U_{pfn}^2 = S_t' + \rho_t' U_{tf}^2 \qquad (44)$$

End if

The time for a wave cycle is

$$\Delta t_1 = \frac{L_p^i}{V_{sp}} \quad and \quad \Delta t_2 = \frac{L_p^{i+1}}{V_{sp}} \qquad (11)\&(13)$$

The penetrator length and crater depth equations

$$L_p = L_p - (U_{pf} + U_{pp})\Delta t_1 - (U_{pf} - U_{pp})\Delta t_2 \qquad (46)$$

$$L_c = L_c + (U_{tf} + \frac{U_{pt}}{2})(\Delta t_1 + \Delta t_2) \qquad (43)$$

The crater diameter equation

$$\frac{D_c}{D_p} = \sqrt{1 + \frac{\rho_p' U_{pf}^2}{\frac{\sigma_{st}}{\nu_t}}} \qquad (82)$$

The final transient at the end of the wave cycle is

$$\frac{L_{ctpf}}{r_p} = \sqrt{\frac{\rho_p' U_{pf}^2}{\sigma_{st}/\nu_t}} - 1 \qquad (92)$$

$$L_{ctpm} = r_p \frac{V_{st}}{V_{stt}} \left(\frac{U_{pt}}{U_{ptfs}} \sqrt{\frac{\rho_t'}{\rho_{tfs}'}} - 1 \right) \qquad (95)$$

$$L_{cfinal} = L_{ctpf} + L_{ctpm} \qquad (96)$$

Checking to see if this expansion will give a greater crater depth than the maximum depth at each wave pass.

$$If\ L_c + L_{cfinal} > L_{cmax}\ then\ L_{cmax} = L_c + L_{cfinal} \quad (102)$$

$$Time = Time + \Delta Time_1 + \Delta Time_2 \quad (103)$$

$$V_p = V_p - 2\,U_{pp} \quad (104)$$

Repeat equations until V_p is below 1 m/s.

BIBLIOGRAPHY

1. McMurtry, J. Scott, "Physical Mechanisms in Terminal Ballistics," Master's Thesis, Louisiana Tech University, February 1991.

2. Tate, A., "Further Results in the Theory of Long Rod Penetration," Journal of Mechanics and Physical Solids, Vol. 17, pp. 141-150, 1969.

3. Tate, A., K. E. B. Green, P. G. Chamberlain, and R. G. Baker, "Model Scale Experiments on Long Rod Penetration," RARDE, Fort Halstead, Sevenoaks, Kent, England, Fourth International Symposium on Ballistics, 1978.

4. Christman, D. R., A. B. Wenzel, and J. W. Gehring, "Penetration Mechanics of High-Velocity Rods," Proceedings of the Seventh Hypervelocity Impact Symposium, Tampa, Florida, November 17-19, 1964.

5. Anderson, Charles E. Jr., and Sol R. Bodner,"Ballistic Impact: The Status of Analytical and Numerical Modeling," International Journal of Impact Engineering, Vol. 7, No. 1, pp. 9-35, 1988.

6. Anderson, Charles E., Jr., and James D. Walker, "An Examination of Long-Rod Penetration," International Journal of Impact Engineering, Vol. 11, No. 4, pp.481-501, 1991.

7. Forrestal, M. J., K. Okajima, V. K. Luk, "Penetration of 6061-T651 Aluminum Targets with Rigid Long Rods," Journal of Applied Mechanics, Vol. 55, December 1988.

8. Forrestal, M. J., N. S. Brar, V. K. Luk, "Penetration of Strain-Hardening Targets with Rigid Spherical-Nose Rods," Journal of Applied Mechanics, Vol. 58, March 1991.

9. Luk, V. K., "Dynamic Cylindrical Cavity Expansion of Compressible Strain-Hardening Materials," Transactions of the ASME, Vol. 58, June 1991.

10. Forrestal, M. J., V. K. Luk, "Penetration of 7075-T651 Aluminum Targets with Ogival-Nose Rods," International Journal of Solids Structures, Vol. 29, No. 14/15, 1992.

11. Lankford, James, Charles E. Anderson, Jr., Suzanne A. Royal and John P. Riegel, III, "Penetration Erosion Phenomenology," International Journal of Impact Engineering, Vol. 18, 1996.

12. Anderson, Charles E., James D. Walker, Stephan J. Bless, and Yehuda Partom, "On the L/D Effect for Long-Rod Penetrators," International Journal of Impact Engineering, Vol. 18, No. 3, 1996.

13. Forrestal, M. J., D. J. Frew, S. J. Hanchak, and N. S. Brar, "Penetration of Grout and Concrete Targets with Ogive-Nose Steel Projectiles,"International Journal of Impact Engineering, Vol. 18, No. 5, 1996.

14. Hanchak, S. J., M. J. Forrestal, E. R. Young, and J. Q. Ehrgott, "Perforation of Concrete Slabs with 48 MPa and 140 MPa Unconfined Compressive Strengths," International Journal of Impact Engineering, Vol. 12, No. 1, 1992.

15. Dancygier, A. N. and D. Z. Yankelevsky, "High Strength Concrete Response to Hard Projectile Impact, "International Journal of Impact Engineering, Vol. 18, No. 6, 1996.

16. Forrestal, M. J., B. S. Altman, J. D. Cargile, and S. J. Hanchak, "An Empirical Equation for Penetration Depth of Ogive Nose Projectiles into Concrete Targets, "International Journal of Impact Engineering, Vol. 15, No. 4, 1994.

17. Salik, Joshua, and Donald H. Buckley, "Effects of Erodant Particle Shape and Various Heat Treatments on Erosion Resistance of Plain Carbon Steel," NASA Technical Paper 1755, 1981.

18. Allen, William A., Earle B. Mayfield and Harvey L. Morrison, "Dynamics of a Projectile Penetrating Sand," Journal of Applied Physics, Vol. 28, No. 3, March 1957.

19. Miyoshi, Kazuhisa and Donald H. Buckley, "Friction and Metal Transfer for Single-Crystal Silicon Carbide in Contact with Various Metals in Vacuum," NASA Technical Paper 1191, 1978.

20. Miyoshi, Kazuhisa and Donald H. Buckley, "Friction and Wear of Metals with a Single-Crystal Abrasive Grit of Silicon Carbide-Effect of Shear Strength of Metal," NASA Technical Paper 1293, 1978.

21. Miyoshi, Kazuhisa and Donald H. Buckley, "Surface Chemistry and Wear Behavior of Single-Crystal Silicon Carbide Sliding Against Iron at Temperatures to 1500 C in Vacuum," NASA Technical Paper 1947, 1982.

22. Miyoshi, Kazuhisa and Donald H. Buckley, "Friction and Wear with a Single-Crystal Abrasive Grit of Silicon Carbide in Contact with Iron-Base Binary Alloys in Oil-Effects of Alloying Element and Its Content," NASA Technical Paper 1394, 1979.

23. Miyoshi, Kazuhisa and Donald H. Buckley, "Wear Mechanism Based on Adhesion," NASA Technical Paper 2037, 1982.

24. Miyoshi, Kazuhisa and Donald H. Buckley, "Friction and Wear of Iron-Based Binary Alloys in Sliding Contact with Silicon Carbide in Vacuum," NASA Technical Paper 1612, 1980.

25. Miyoshi, Kazuhisa and Donald H. Buckley, "Friction and Wear Characteristics of Iron-Chromium Alloys in Contact with Themselves and Silicon Carbide," NASA Technical Paper 1387, January 1979.

26. Loomis, William and William R. Jones, Jr., "Steady-State Wear and Friction in Boundary Lubrication Studies," NASA Technical Paper 1658, 1980.

27. Tylczak, J. H., "Correlating Abrasive Wear to Alloy Additions in Low-Alloy Steels." Personal Communication.

28. Longcope, Donald B., Jr., "Coupled Bending/Lateral Loading Modeling of Earth Penetrators," SAN90-0789, July 1990.

29. Lundgren, Ronald G., "High-Velocity Penetrators," SAN094-2724C, Sandia National Laboratories, Albuquerque, New Mexico, U. S. A.

30. Forrestal, M. J., L. M. Lee, B. D. Jenrette, and R. E. Setchell, "Gas-Gun Experiments Determine Forces on Penetrators into Geological Targets," Transactions of the ASME, Vol. 51, pp. 602-607, September 1984.

31. Forrestal, M. J., L. M. Lee, and B. D. Jenrette, "Laboratory-Scale Penetration Experiments into Geological Targets to Impact Velocities of 2.1 km/s," Journal of Applied Mechanics, Vol. 53, pp. 317-320, June 1986.

32. Brunette, Harold, and Werner Goldsmith, "Propellant-Driven Anchoring in Rock: Results from Initial Scaling Tests," International Journal of Impact Engineering, Vol. 9, No. 1, pp. 51-69, 1990.

33. Turgutlu, A., S. T. S. Al-Hassani, and M. Akyurt, "The Influence of Projectile Nose Shape on the Morphology of Interface in Impact Spot Welds," International Journal of Impact Engineering, Vol. 18, No. 6, pp. 657-669, 1996.

34. Chen, E. P., "Numerical Simulation of Dynamic Fracture and Failure in Solids," CONF-940771-1, Sandia National Laboratories, Albuquerque, New Mexico, 1994.

35. Silsby, G. F., "Penetration of Semi-Infinite Steel Targets by Tungsten Long Rods at 1.3 to 4.5 km/s," Proceedings of the 8th International Symposium on Ballistics, Orlando, Fl., 23-25 October 1984.

36. Magness, L. S. and T. G. Farrand, "Deformation Behavior and its Relationship to the Penetration Performance of High-Density KE Penetrator Materials," Army Science Conference, Durham, N.C., 1990.

37. Morris, B. L. and C. E. Anderson, Jr., "The Ballistic Performance of Confined Ceramic Tiles," Proceedings of the 1991 TACOM Combat Vehicle Survivability Symposium, pp. 235-244, 15-17 April 1991.

38. Keele, M., E. Rapacki, Jr., and W. Bruchey, Jr.,"High Velocity Ballistic Performance of a Uranium Alloy Long Rod Penetrator," Proceedings of the 12th International Symposium on Ballistics, San Antonio, TX, 30 Oct - 1 Nov 1990.

39. Hohler, V. and A. J. Stilip, "Penetration of Steel and High Density Rods in Semi-Infinite Steel Targets," Proceedings of the 3rd International Symposium on Ballistics, Karlsruhe, FRG, 23-25 March 1977.

40. Fugelso, E., "Further Experimental Studies on the Effect of Combined Obliquity and Yaw on the Perforation of Steel Plates by Long-Rod U-0.75 Wt% Ti Penetrators," Report No. LA-8357-MS, Los Alamos Scientific Laboratory, Los Alamos, NM, 1983.

VITA

J. Scott McMurtry was born in Springhill, Louisiana in 1965. In 1983, he was admitted to Louisiana Tech University to pursue the degree Bachelor of Science in Mechanical Engineering. He received the Bachelor's degree in 1987 and the Masters degree in 1991.